UNIVERSITY OF OSLO
Department of
Geosciences MetOs section

Identification of wildfire aerosols in LIDAR data and model calculations of the vertical propagation of absorbing aerosols

Master thesis in
Geosciences
Meteorology and
Oceanography

Tobias Wolf

July 19, 2012

Abstract

Wildfires are a source of major perturbations in the earth-atmosphere system. Between 1997 and 2008, an area of roughly $4 \cdot 10^6$ km^2 has been burned each year. Among other species, wildfire aerosols consist of black carbon that absorbs solar (short wave) radiation. This can lead to a warming of the surrounding air causing buoyancy and vertical transport, an effect known as radiatively induced self-lifting or short self-lifting.
To assess the influence of wildfire aerosols on the climate system, it is important to know their altitude distribution. If wildfire aerosols are e.g. lifted into a cloud, they can alter the cloud development through the indirect and the semi-direct aerosol effects. In addition, vertical transport can alter the residence time and transport distance of the absorbing aerosols. Therefore, this study aimed to analyse LIDAR data for wildfire aerosols and to study the effects of radiation absorption on the vertical propagation of the absorbing aerosols. For this, LIDAR data from the ALOMAR research station have been analysed for potential aerosol layers between April and September 2010 and 2011 together with auxiliary data, like SYNOP data and radiosonde measurements. The source regions of the aerosol layers above ALOMAR have been determined with the help of FLEXPART simulations and were compared to MODIS wildfire data.
Two events have been identified with clear wildfire aerosol transport towards ALOMAR. The event showing an aerosol layer from fires west of Lake Superior was chosen for simulations with WRF-Chem. An aerosol layer above ALOMAR was reproduced in the WRF-Chem simulations but uncertainties in emissions and transport caused the simulated aerosol concentrations above ALOMAR to be too low. Therefore, no self-lifting has been found for this plume. However, signs of self-lifting have been found in a plume that originated from stronger wildfires in Kansas during the same time, and in an analysis of domain averaged properties.
Two main effects of radiation absorption on the vertical propagation of the aerosols have been found: the additional radiation extinction through the absorption of short wave radiation led to a cooling of the ground at the emission sites, causing a trapping of the aerosols close to the ground above the fires. Later on, short wave heating caused a lifting of strong aerosol plumes.
Wet-scavenging was reduced through the absorption of short wave radiation. An analysis of the probability distribution function of the black carbon aerosol concentrations showed that the overall effect of the radiation absorption was to keep the plumes more intact. The effect without the trapping of the aerosols at the fires and the reduced wet-scavenging led to a dilution of the plume edges, indicating the development of a convectively mixed layer at the plume tops, whereas the plume centres were protected from dilution.
Overall, self-lifting was only found important for concentrated plumes.

Acknowledgements

First of all, I would like to thank my supervisors Jón Egill Kristjánsson and Andreas Stohl for their guidance and support during the last year and for their open doors.

I would also like to thank Michael Gausa from ALOMAR for many helpful discussions and comments in connection with the LIDAR data and the staff at ALOMAR for welcoming me so nicely during my visit.

The people at MEtOs and the Meteorological Institute were very helpful throughout the entire study, from listening to my problems to helping me with the WRF-Chem model, discussions about the various topics in this thesis and general help with computer problems. I would especially like to mention Øivind Hodnebrog, Melissa Anne Pfeffer, Gunnar Wollan, Frode Stordal and Kjell Andresen and my fellow students.

Finally, I would like to thank my family: my parents Brunhilde and Walter Wolf, who always were there for me and my girlfriend Susann Große, who supported me in so many ways.

Tobias Wolf

Oslo, July 19, 2012

Several datasets from various sources have been used in this thesis. The author acknowledges the contribution from those sources.

Abbreviations

AERONET	**AE**rosol **RO**botic **NET**work
ALOMAR	**A**rctic **L**idar **O**bservatory for **M**iddle **A**tmosphere **R**esearch
AMSL	**A**bove **M**ean **S**ea-**L**evel
AOD	**A**erosol **O**ptical **D**epth
APD	**A**valange **P**hoto **D**iode
ARL	**A**ir **R**esource **L**aboratory
ARR	**A**ndøya **R**ocket **R**ange
ARW	**A**dvanced **R**esearch **W**RF
BC	**B**lack **C**arbon
BHR	**B**ackground subtracted, **H**eight corrected and **R**ayleigh extinction
BW	**B**and **W**idth
CCN	**C**loud **C**ondensation **N**uclei
CMG	**C**limate **M**odeling **G**rid
CW	**C**enter **W**avelength
DBS	**D**icroic **B**eam **S**plitter
ECMWF	**E**uropean **C**entre for **M**edium-Range **W**eather **F**orecasts
EST	**E**astern **S**tandard **T**ime
FINN	**F**ire **IN**ventory from **N**CAR
GDAS	**G**lobal **D**ata **A**ssimilation **S**ystem
HYSPLIT	**HY**brid **S**ingle **P**article **L**agrangian **I**ntegrated **T**rajectory
IAP	Leibniz-**I**nstitut für **A**tmosphären**P**hysik
IPCC	**I**ntergovernmental **P**anel on **C**limate **C**hange
IR	**I**nfra **R**ed
IF	**I**nterference **F**ilters
LIDAR	**L**ight **D**etection **A**nd **R**anging
LST	**L**ocal **S**olar **T**ime
LTER	**L**ong-**T**erm **E**cological **R**esearch
LW	**L**ong **W**ave
MADE	**M**odal **A**erosol **D**ynamics Model for **E**urope
MODIS	**MOD**erate-Resolution **I**maging **S**pectroradiometer
MPF	**M**otorized **P**olarisation **F**ilter
MSIS-E-90	**M**ass-**S**pectrometer-**I**ncoherent-**S**catter **E**xtended 90
MWMA	**M**ass **W**eighted **M**ean **A**ltitude

NASA	**N**ational **A**eronautics and **S**pace **A**dministration
NCAR	**N**ational **C**enter for **A**tmospheric **R**esearch
NCEP	**N**ational **C**enters for **E**nvironmental **P**rediction
ND	**N**eutral **D**ensity filter
NILU	**N**orsk **I**nstitutt for **LU**ftfoskning
NMM	**N**on-hydrostatic **M**esoscale **M**odel
NOAA	**N**ational **O**ceanic and **A**tmospheric **A**dministration
OC	**O**rganic **C**arbon
PBL	**P**lanetary **B**oundary **L**ayer
PBS	**P**olarizing **B**eam **S**plitter cube
PDF	**P**robability **D**istribution **F**unction
PDR	**P**article **D**epolarization **R**atio
PES	**P**otential **E**mission **S**ensitivity
PM	**P**articulate **M**atter
PMT	**P**hoto **M**ultiplier **T**ube
PSC	**P**otential **S**ource **C**ontribution
RADM	**R**egional **A**cid **D**eposition **M**odel
RCS	**R**ange **C**orrected **S**ignal
READY	**R**eal-time **E**nvironmental **A**pplications and **D**isplay s**Y**stem
RIMA	**R**ed **I**bérica de **M**edida fotométrica de **A**erosoles
RMR	**R**ayleigh-**M**ie-**R**aman
RRI	**R**apide **R**esponse **I**magery
SORGAM	**S**econdary **ORG**anic **A**erosol **M**odel
SSA	**S**ingle **S**cattering **A**lbedo
SW	**S**hort **W**ave
SYNOP	Surface **SYNOP**tic
UiO	**U**niversitetet **i** **O**slo
UTC	**U**niversal **T**ime **C**oordinated
WMO	**W**orld **M**eteorological **O**rganization
WPS	**W**RF **P**reprocessing **S**ystem
WRF	**W**eather **R**esearch and **F**orecasting
VDR	**V**olume **D**epolarisation **R**atio

Contents

1 Introduction **1**
- 1.1 Literature review on self-lifting . . . 2
- 1.2 Aim of the study and outline . . . 4

2 Theoretical Background **5**
- 2.1 Wildfires . . . 5
- 2.2 Interactions between light and atmospheric matter . . . 7
  - 2.2.1 Inelastic scattering . . . 7
  - 2.2.2 Elastic scattering . . . 8
  - 2.2.3 Bulk optical properties . . . 9
- 2.3 Radiatively induced self-lifting . . . 10
  - 2.3.1 Theoretical self-lifting potential . . . 10
  - 2.3.2 Conceptual approach to self-lifting . . . 12
- 2.4 Aerosol effects on earth's radiation budget . . . 14
  - 2.4.1 Direct aerosol effect . . . 15
  - 2.4.2 Indirect aerosol effects . . . 15
  - 2.4.3 Semi-direct aerosol effect . . . 16
- 2.5 LIDAR instruments . . . 17
  - 2.5.1 LIDAR equation and depolarization ratio . . . 18
- 2.6 Atmospheric models . . . 19
  - 2.6.1 Eulerian models . . . 20
  - 2.6.2 Lagrangian models . . . 20

3 Materials and Methods **23**
- 3.1 ALOMAR troposphere LIDAR . . . 23
  - 3.1.1 ALOMAR . . . 23
  - 3.1.2 Alomar troposphere LIDAR . . . 24
  - 3.1.3 Raw data treatment . . . 24
  - 3.1.4 Identification of potential aerosol layers . . . 26
  - 3.1.5 PDR and VDR calculation . . . 27
  - 3.1.6 Glueing and noise problems . . . 29
- 3.2 SYNOP data . . . 29
- 3.3 Radio-soundings from Bodø airport . . . 30
- 3.4 MODIS . . . 31
  - 3.4.1 NASA's RRI . . . 31
  - 3.4.2 MODIS CMG data . . . 32

3.4.3 MODIS daily wildfire data . . . 32
3.4.4 MODIS AOD . . . 33
3.5 AERONET . . . 33
3.6 NCEP weather maps . . . 34
3.7 HYSPLIT . . . 34
3.8 MSIS-E-90 model . . . 35
3.9 FLEXPART . . . 36
3.9.1 The FLEXPART model . . . 36
3.9.2 Model version and setup . . . 36
3.9.3 Input data . . . 37
3.9.4 FLEXPART data evaluation . . . 37
3.10 WRF and WRF-Chem . . . 39
3.10.1 WRF . . . 39
3.10.2 WRF-Chem . . . 41
3.10.3 Input data sets . . . 43
3.10.4 Simulations . . . 44
3.10.5 Data evaluation . . . 45

4 Results and Discussion 47
4.1 Identification of wildfire aerosol layers . . . 47
4.2 In-depth analysis April 17, 2010 . . . 48
4.2.1 LIDAR results . . . 48
4.2.2 HYSPLIT results . . . 53
4.2.3 MODIS RRI quick plot . . . 54
4.2.4 Radio and SYNOP results . . . 55
4.2.5 FLEXPART source specification results . . . 56
4.3 Weather maps . . . 64
4.4 WRF-Chem transport analysis . . . 64
4.4.1 Comparison of the simulated AOD to measurements . . . 71
4.5 Influence of the Eyjafjallajökull eruption . . . 77
4.6 Analysis of radiatively induced self-lifting . . . 78
4.6.1 Single plumes . . . 78
4.6.2 Domain averaged effects . . . 87

5 Summary and Conclusions 97
5.1 Summary . . . 97
5.2 Final conclusions and future work . . . 100

References 103

A LIDAR 111
A.1 LIDAR schematic and specifications . . . 111
A.2 Description of the LIDAR components . . . 113
A.2.1 Transmission unit . . . 113
A.2.2 Reception unit . . . 113
A.2.3 Acquisition unit . . . 114
A.3 Filter design for LIDAR data evaluation . . . 115

A.4 LIDAR signal calibration . . . 115
A.4.1 Calibration on the basis of the Rayleigh signal . . . 115
A.5 Calibration routine based on the MPF . . . 116
A.6 Electronic noise . . . 117

B WRF-Chem **119**
B.1 Description of RADM2/MADE/SORGAM(aq) . . . 119
B.2 Model control . . . 119

C Bugs and added routines in WRF-Chem **121**
C.1 FINN . . . 121
C.2 Added routines to WRF-Chem . . . 122
C.3 Bug in the WPS routine . . . 124
C.4 Bug in the FINN tool . . . 126
C.5 SORGAM aerosols . . . 126

D Illustration of the use of PDFs **127**

Chapter 1

Introduction

Climate change is one of the most discussed topics worldwide. A Google search gave 817,000,000 hits for "climate change", 760,000,000 for "world peace" and 750,000,000 hits for "cancer research". In addition, climate change is also one of the most controversially discussed topics.

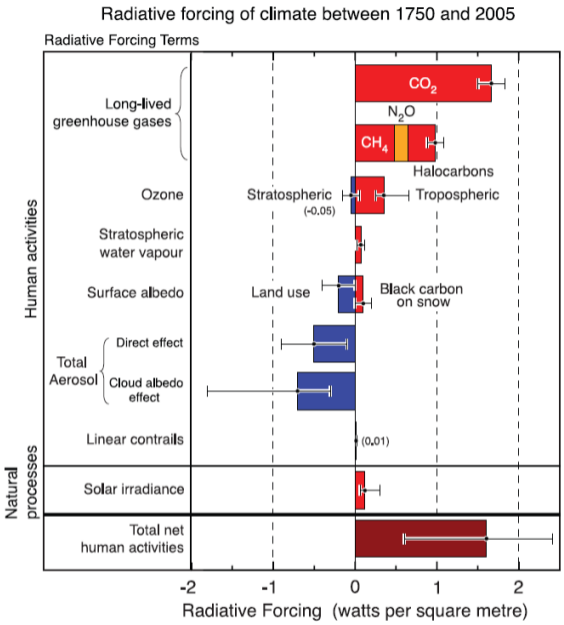

Figure 1.1: "Summary of the principal components of the radiative forcing of climate change." Figure from Forster et al. (2007)

Figure 1.1 from the last assessment report of the **I**ntergovernmental **P**anel on **C**limate **C**hange (IPCC) provides a best estimate of the differences in radiative forcing of different components of the earth-atmosphere system due to anthropogenic influences between 1750 and 2005. Black horizontal bars indicate the uncertainties connected to each component. The largest uncertainties were found in connection to aerosol effects.

Biomass burning is one of the main contributors to atmospheric aerosols. However, even the sign of the radiative forcing due to biomass burning aerosols was still under discussion in the IPCC report.
Indications have been found that wildfire occurrence and intensity has increased because of the ongoing climate change [Westerling et al. (2006), Gillett et al. (2004), Achard et al. (2008)], making a detailed understanding of the net effect of wildfire aerosol emissions even more important.
In contrast to other aerosol mixtures, like desert dust and volcanic ash, biomass burning aerosols do not only contain species that are light scattering. **B**lack **C**arbon (BC) absorbs **S**hort **W**ave (SW) radiation, resulting in a warming of the surrounding air. This can have a number of impacts on the earth-atmosphere system: Radiative forcing of different signs has been found dependent on the existence of underlying clouds [Keil and Haywood (2003)]. The warming of the air can lead to a suppression of clouds within or below the aerosol plume, called the semi-direct aerosol effect [Sakaeda et al. (2011)] causing a positive radiative forcing. In addition to effects in the atmosphere, BC aerosols can have an influence on the development of glaciers, especially under significant transport to high latitudes [Stohl et al. (2007)]. There, BC can decrease the snow albedo and cause a positive radiative forcing [Hadley and Kirchstetter (2011)].
Like other aerosols, biomass burning aerosols can have an influence on clouds through the indirect aerosol effects. Large aerosols have some influences in the **L**ong **W**ave (LW) spectral region as well. However, BC, in contrast to purely scattering aerosols, can even have an influence on its own vertical transport by creating additional buoyancy through SW heating. This again, will affect long-range transport and the effects that have been listed above. It is therefore important to deepen the understanding of long-range transport and vertical propagation of biomass burning aerosols.

1.1 Literature review on self-lifting

Concerns have been raised since the 1980's about the residence time of aerosol layers caused by a nuclear war. This led to the investigation of the "Nuclear Winter" scenario, where a large amount of smoke is inserted into the upper troposphere and stratosphere. Light absorbing aerosols might prolong their residence time through radiatively induced self-lifting (or short 'self-lifting'). Self-lifting is caused by a diabatic heating due to the absorption of SW (solar) radiation. Malone et al. (1986) examined the effects of a theoretical nuclear war and found extended residence times of aerosols in high altitudes due to the self-lifting effect. During ascent, a large amount of aerosols was removed by wet-scavenging and self-shielding (the lower part of a plume was not heated since the sunlight was blocked from the aerosols above). The wet-scavenging rates in an absorbing aerosol plume were reduced in comparison to the rates in a non-absorbing plume. However, this effect was mostly concluded to be connected to the appearance of a new, lower tropopause due to the strong heating, shielding the aerosols from the moist troposphere. The effect of the self-shielding

led to a separation of the upper plume part from the lower one.
Fortunately, the theoretical considerations of a nuclear war could never be investigated in reality. However, evidence of self-lifting was found from observational studies of oil fires. Radtke et al. (1990) conducted an experiment, in which a large amount of aviation fuel was burned in a pool during fair weather conditions. Rudich et al. (2003) re-analysed the Kuwait oil fires with focus on cloud effects. Both found evidence of self-lifting. Radtke et al. (1990) found additionally evidence of a splitting of the plume that was trapped in the PBL. A suppression of cloud formation was revealed within the highly absorbing plumes and an increase of cloudiness above the plume due to a cooling of the air above. It was assumed that self-lifting caused an ascending motion of the air above the plume, resulting in an adiabatic cooling. Herring and Hobbs (1994) conducted an observational study of the Kuwait oil fires, together with radiative transfer calculations. They also included an argumentation about the aerodynamic resistance of a large scale plume against uplifting and about dilution.
Boers et al. (2010) re-visited the theory of radiatively induced self-lifting in connection with wildfire aerosols. They conducted an idealised study of self-lifting of plumes with fixed thickness and optical depth on the basis of radiative transfer calculations. It was concluded that a wildfire aerosols plume could reach the tropopause within 3-4 days, only through radiatively induced self-lifting together with pole-ward transport and the corresponding altitude gain due to the rising isentropes.
deLaat et al. (2012) found evidence of aerosol transport into the stratosphere in connection with a strong burning event in Australia. They used observations from satellites and radio soundings together with trajectory calculations to prove that the stratosphere transport was not caused by pyro-convection [Fromm and Servranckx (2012)]. An analysis of the lifting potential with the same method as in Boers et al. (2010) suggested that aerosols could have been transported into those high altitudes by self-lifting. From the argumentation of Boers et al. (2010) and deLaat et al. (2012), it should in theory be possible for strong enough plumes to reach the tropopause within a few days.
However, cooling and cloud development above the plume, as found by Rudich et al. (2003), and aerodynamic resistance, as discussed by Herring and Hobbs (1994), were not included in their argumentation.
So far, studies that aimed to analyse wildfire aerosol plumes after long-range transport were mostly conducted with the help of offline transport models [Forster et al. (2001), Amiridis et al. (2009), Stohl et al. (2006)]. Radiatively induced self-lifting outside of the nuclear winter theory has only rarely been analysed. A study that was aimed to understand the effects caused by the SW-absorbing wildfire aerosols (not the feedback directly on them), found increased wet deposition in connection with self-lifting [Westphal and Toon (1991)]. Liu (2003) found a reduction of clouds in connection to a wildfire aerosol plume because of a cooling of the ground underneath the plume and a subsequent reduction in moisture transport out of the PBL to the cloud layers. The effect of the SW heating directly on the relative humidity in the layer was smaller. Trentmann et al. (2002) simulated the initial development of an aerosol plume and compared the results to observations. They found some altitude differences between simulations with and without interaction between radiation and

aerosols. However, their analysis extended only over a few hours after the emissions. To the knowledge of the author, no sensitivity study exists that analysed the effects of radiation absorption on the vertical propagation of wildfire aerosols in a fully coupled atmospheric chemistry transport model. Stenchikov et al. (2006) published an abstract for a new study on the self lifting of wildfire aerosol layers from the upper troposphere to the lower stratosphere by using a regional scale atmospheric model with radiatively interactive tracers. However, the corresponding article has not been published.

1.2 Aim of the study and outline

The aim of this study was to analyse the influence of radiation absorption on the vertical propagation of wildfire aerosols during transport towards the Arctic.
For this, data from the ALOMAR troposphere LIDAR were analysed for potential aerosol layers (together with other observational data to separate out clouds). HYSPLIT and FLEXPART simulations were used to find the source regions of the potential aerosol layers. The source regions were compared to satellite wildfire detections to identify potential aerosol layers above ALOMAR as wildfire aerosols.
Strong wildfire aerosol layers should then be chosen for analysis with WRF-Chem. It was aimed to analyse a number of cases to assess the importance of self-lifting for the long-range transport of wildfire aerosol layers. For this, it was planned to make simulations with and without radiation absorption by BC and to compare them. The LIDAR data should be used to validate the altitude of the layers.
Wildfire aerosol layers from burns in Russia were preferred because of the potentially shorter distance between the source region and the ALOMAR station in comparison to e.g. burns in North America. This would have the advantage, that uncertainties in transport might be smaller and that the plumes are not as strongly diluted as plumes from more distant sources. Since transport towards the Arctic was analysed, the search for wildfire sources was constrained to mid- to high latitudes.

Only two events were found to show aerosol layers that could be connected to wildfires. Both had their origin in North America. Due to a lack of time it was decided to analyse one case in detail with WRF-Chem as a sensitivity analysis, instead of doing only a basic analysis of both. The case that was chosen for simulations with WRF-Chem showed a good overlap between transport simulations and high fire activity and had the strongest LIDAR signal of all aerosol layers that were analysed. Uncertainties in the simulated transport were found as a problem. This caused the simulated aerosol concentrations over ALOMAR to be too low, making a validation of the analysis of self-lifting on the basis of the LIDAR data impossible. Instead, a case-study was made to analyse the importance of self-lifting in dependence of the emission strength, based on a strong plume from other fires in a region close-by during the same time. In addition, the domain-averaged self-lifting and its influences on the intactness of plumes were analysed for different emission scenarios.

Chapter 2

Theoretical Background

The theoretical background with its main concepts is presented in this chapter.

2.1 Wildfires

Wildfires are sources of major perturbations in the earth-atmosphere system. Between 1997 and 2008, the annually burned area was roughly between $3.30 \cdot 10^6$ km^2 and $4.31 \cdot 10^6$ km^2 [Giglio et al. (2010)]. This is more than 10 times the size of Norway. From Figure 2.1 it can be seen that most of the fires burned in Africa and Australia with a burned fraction of nearly 100% in central Africa. High fire activity was also found in North America and northern Eurasia.

Wildfires emit a wide variety of gaseous and aerosol species. For this work, the aerosol emissions were important. They are, in turn, also influenced by the gaseous species, e.g. through the production of secondary organic aerosols.

Particle sizes emitted from fires cover a very broad range in the initial phase after the emissions. Within the first few minutes, a nucleation mode exists that is more and more depleted into the accumulation mode due to coagulation. The accumulation mode (with count median diameter of 100-150 nm and mass median diameter

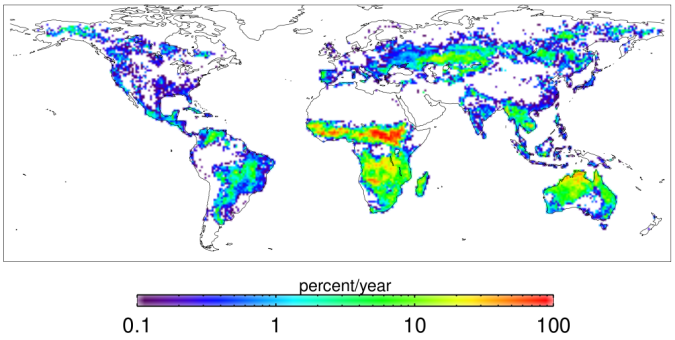

Figure 2.1: The global mean area fraction burned by open fires from 2001 - 2004. Figure from Giglio et al. (2006).

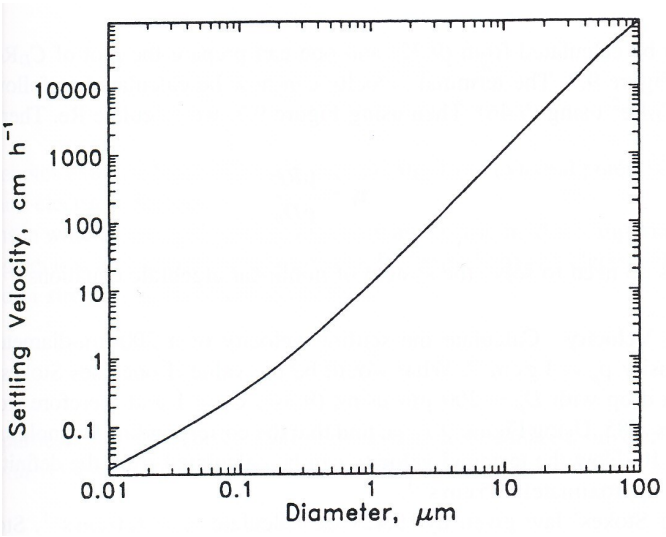

Figure 2.2: Settling velocity of particles with unit density in air at 298 K and ground pressure as a function of the particle diameter. Figure from Seinfeld and Pandis (2006).

around 240 nm) is the dominating size range of wildfire emissions. A coarse particle mode is often found near by wildfires with particle mass mean diameter of several μm and maximum diameter of up to several cm. That mode is depleted quickly due to gravitational settling.
The accumulation mode particles mostly consist of **O**rganic **C**arbon (OC). BC and inorganic species can each contribute up to 10%. The coarse mode particles mostly consist of dust, organic matter, ash and unperturbed fuel parts (e.g. small leaf fragments) [Janhäll et al. (2010)].
The gravitational settling speed of accumulation mode particles is low. Figure 2.2 illustrates the settling speed of particles with unit density at ground level pressure. For particles with sizes around 200 nm, the settling speed is roughly 1 $\frac{cm}{h}$, corresponding to 24 $\frac{cm}{day}$. The density of wildfire aerosols is smaller than 2 $\frac{g}{cm^3}$ [Reid et al. (2005)]. Since the settling speed is linear with the density of the particles, the settling rate of wildfire aerosols with a diameter of 200 nm would be 48 $\frac{cm}{day}$.

Wildfire aerosols can be transported over long-ranges, when they reach the free troposphere above the **P**lanetary **B**oundary **L**ayer (PBL). For this, they do not need to be released into this altitude directly during emissions. Different processes of lifting and mixing into the free troposphere can occur later (e.g. during transport in a warm conveyor belt or self-lifting).
During transport, aerosols can be removed by three different mechanisms:

- Wet-scavenging
- Dry-deposition after gravitational settling
- Dry-deposition during vertical mixing (mostly only important in the PBL)

Gravitational settling is small for accumulation mode particles and happens mostly in connection with coagulation of particles to larger sizes, having a higher settling speed (several μm).

During emissions, wildfire aerosols mostly consist of externally mixed particles (meaning that each single aerosol particle consists of only one species, but different particles can consist of different species). Later, this external mixture is transformed into an internal mixture [Reid et al. (2005)]. BC can e.g. become coated by sulphate that was emitted from the fires or from other emission sources. This coating increases the volume and therewith the settling speed of the particles and increases their light absorption cross section [Jacobson (2001)].

2.2 Interactions between light and atmospheric matter

There are two main ways of how radiation can interact with an atmospheric molecule or particle (aerosol): scattering and absorption.
The interaction is referred to as absorption, if the entire energy of a photon is absorbed. This can either lead to an ionisation of the molecule (e.g. UV absorption of ozone) or to a heating of the molecule or particle (e.g. BC). At least a part of the absorbed energy can be radiated away later, for example as **I**nfra **R**ed (IR) radiation from the surrounding air (thermal conduction). The absorptivity of a species is described by its imaginary refractive index.
The interaction between radiation and matter is referred to as scattering, if at least a part of the energy of the incoming photon is re-emitted right away (scattered) and only a part of the energy is absorbed. There are two main types of scattering: inelastic and elastic scattering.

2.2.1 Inelastic scattering

A scattering process is referred to as inelastic, if a part of the kinetic energy of the scatterers is transformed into some other form of energy.
An example for an inelastic scattering process from our daily life is a crash between two cars: A large amount of the kinetic energy of the two cars is transferred into the deformation of the crush zone. The original kinetic energy is transferred to a deformational energy and heat.
An important example of inelastic scattering in the atmosphere is Raman scattering. A degree of freedom of a bound electron is excited by the incoming radiation. The energy of the photon after the scattering process is reduced by the energy that was necessary for the excitation of the electron, leading to a frequency shift of the incoming radiation towards a longer wavelength. If light is scattered a second time by the same molecule, the energy from the excited state can be released again, leading to a frequency shift of the scattered radiation towards a shorter wavelength. The total scattering cross-section (corresponding to the scattering efficiency) for Raman scattering is small. Hence, Raman scattering can never be observed in daily life. For LIDAR remote sensing applications, however, Raman scattering is an important effect.

2.2.2 Elastic scattering

A scattering process is referred to as elastic, when no transfer of energy into some other form of energy occurs during the scattering process. The condition for fully elastic scattering is rarely reached for large scales. An example of an almost perfect elastic scattering process is the collision of two steel spheres. The original kinetic energy of the two spheres is almost entirely conserved.
There are three different mathematical solutions for the description of elastic light scattering on atmospheric particles and molecules: the Mie-solution, the Rayleigh solution and the classical solution. Which solution the most appropriate is, is determined by the size parameter [Liou (2002)]:

$$x = 2\pi \cdot \frac{a}{\lambda}, \tag{2.1}$$

where a is the particle radius and λ is the wavelength of the incoming radiation.

Mie solution

The Mie solution is the actual solution of Maxwell's equations for the scattering process of a light wave at a spherical particle. It is used, when the particle has about the same size as the wavelength ($x \approx 1$) or is somewhat larger ($x \geq 1$). Mie scattering has a complicated angular pattern of the scattering cross section with an increasing contribution of forward scattering with increasing particle size (Figure 2.3). In a wave-like approach, Mie scattering can be interpreted as the refraction of the incoming wave at the particle. The total Mie scattering cross-section shows a $\frac{1}{\lambda^2}$ dependence on the wavelength of the scattered light. Atmospheric aerosols fall into the range of the Mie solution for SW (solar) radiation.

Rayleigh solution

For small sizes of the scatterers such as molecules in the atmosphere ($x \ll 1$), the Mie solution can be approximated by the much simpler Rayleigh solution. The Rayleigh solution shows a symmetric scattering cross-section between forward and backward-scattering. Rayleigh scattering shows a strong wavelength dependence of the total scattering cross-section with $\frac{1}{\lambda^4}$ (in comparison to the $\frac{1}{\lambda^2}$ dependence of the Mie-solution). A well-known example of the wavelength dependence of Rayleigh scattering is the blue colour of the sky and the yellow colour of the sun: For the entire sky, except for the sun, the strong scattering of the blue part of the visible spectrum (short wavelengths) makes the air look blue. For the sun, Rayleigh scattering causes the blue part of the visible spectrum to be scattered into other directions. The direct sun-light has a reduced contribution from the blue light, the sun appears yellow. If the atmosphere was much thinner, the sun would appear much whiter and the sky black.

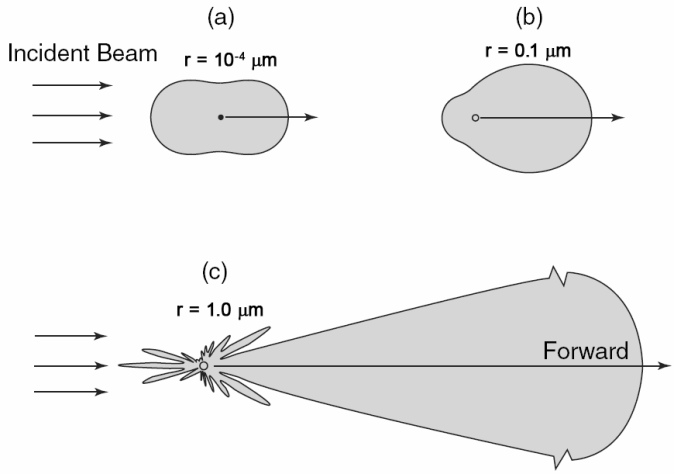

Figure 2.3: Angular dependence of the scattering cross-section from spherical aerosols for three different sizes. The size parameters are $1.26 \cdot 10^{-3}$ (a), 1.26 (b) and 12.6 (c). The increasingly complicated angular dependence of the scattering cross-section with increasing size parameter can easily be seen. Figure from Liou (2002).

Classical solution

For very large particles ($x \gg 1$), the Mie solution can be approximated by the classical description of light scattering at surfaces. An example of this effect are the multiple reflections within rain droplets leading to a rainbow or the reflection of light at horizontally aligned ice crystals.

2.2.3 Bulk optical properties

So far, only the optical properties of single particles and molecules have been discussed. However, it is impossible to describe a layer of air and aerosols by describing all single particles and molecules. Therefore, bulk properties are necessary.

Optical depth

The total optical depth of a layer with total thickness r is defined as

$$\tau_t = \int_0^r \beta_e(r')\, dr' \tag{2.2}$$

with β_e the extinction coefficient. It allows for a simple expression for the reduction of the light intensity after having passed the layer (multiple scattering is neglected):

$$\frac{I}{I_0} = exp(-\tau_t \cdot \frac{1}{\cos(\theta_0)}), \tag{2.3}$$

with I_0, the light intensity at the top of the layer, I the intensity underneath the layer and θ_0 the angle, under which the light passes the layer. An important quantity

for the analysis of atmospheric aerosols is the **A**erosol **O**ptical **D**epth (AOD)

$$\tau = \int_0^r \beta_{e,p}(r')\, dr'. \tag{2.4}$$

It is the fraction of the optical depth that is caused purely by aerosol extinction $\beta_{e,p}(r')$ (Mie solution)

Ångstrøm exponent

The Ångstrøm exponent is used to describe the relation of the AOD between two different wavelengths. It is defined as

$$\alpha = -\frac{\log \frac{\tau_{\lambda 1}}{\tau_{\lambda 2}}}{\log \frac{\lambda 1}{\lambda 2}} \tag{2.5}$$

The Ångstrøm exponent varies inversely with the size of the aerosols (the Ångstrøm exponent is small for large aerosols and vice versa). In the wavelength region, where the Ångstrøm exponent is valid, the AOD at every wavelength can easily be calculated by an inversion of Equation (2.5).

Single scattering albedo

The **S**ingle **S**cattering **A**lbedo (SSA) is the ratio of scattering and extinction by an atmospheric layer. It gives a quick overview, if an aerosol layer contains absorbing or only scattering particles. A SSA of 1 refers to a purely scattering layer and a SSA of 0 refers to a purely absorbing layer.

Other optical parameters, like the asymmetry factor, are included in radiative transfer routines but were not analysed separately and thus, are not explained here.

2.3 Radiatively induced self-lifting

2.3.1 Theoretical self-lifting potential

When solar radiation penetrates a layer of absorbing aerosols, energy is deposited in the layer. The amount of energy that is deposited in the entire layer is mostly dependent on the AOD and the SSA. An optically very thick layer with a low SSA absorbs a large amount of the radiative energy. This energy leads to a diabatic heating of the layer. When it is assumed that the only process influencing the layer is diabatic heating through SW radiation (under the assumption of a constant heating throughout the entire layer), then [Boers et al. (2010)]

$$\frac{d\Theta}{dt} = -\frac{1}{\rho c_p}\frac{dR}{dz} \tag{2.6}$$

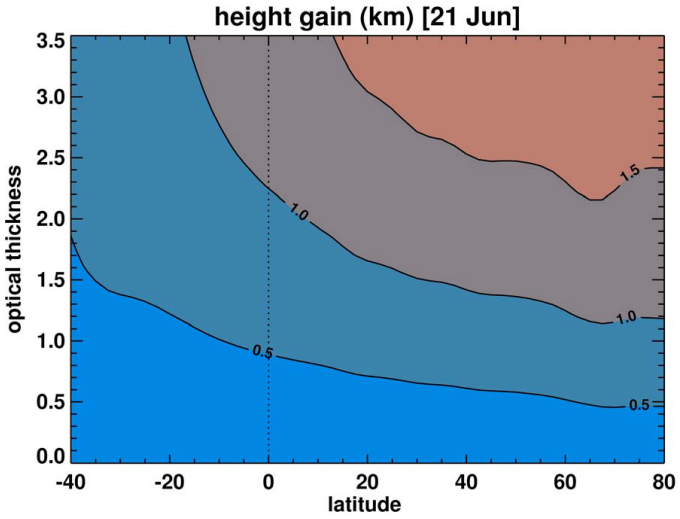

Figure 2.4: Altitude gain over 24 hours due to absorption of solar radiation for a layer with $SSA = 0.75$, $\alpha = 1.50$ and $\Gamma = 0.7$ during June 21 (longest day on the northern hemisphere), based on the assumptions of constant heating, no dilution and instantaneous lifting of the layer. The optical thickness refers to the AOD at 500 nm. Figure from Boers et al. (2010).

where $d\Theta$ is the change in the potential temperature of the layer, ρ is the density of dry air, R is the SW radiative flux and c_p is the heat capacity at constant pressure. The heat gain of the layer produces buoyancy, resulting in a lifting of the layer. The theoretical altitude gain is

$$z_1 - z_0 = \frac{\Theta_1 - \Theta_0}{\gamma}, \tag{2.7}$$

with γ the background atmospheric lapse rate, z_0 and z_1 the altitude before and after the lifting, Θ_0 the potential temperature of the surrounding air and Θ_1 the potential temperature of the heated plume. This process is called radiatively induced self-lifting or short self-lifting.
Figure 2.4 shows the theoretical altitude gain of a three km thick plume over a period of 24 hours due to radiation absorption, dependent on the optical thickness and latitude during June 21 (longest day on the northern hemisphere). Reflection of SW radiation from below was ignored.

The theoretical altitude gain due to radiation absorption is dependent on additional factors like the albedo of the underlying surface that reflects solar radiation back through the layer. An underlying surface with a higher albedo leads to a stronger heating of the layer. Solar irradiance is dependent on the wavelength and so is the scattering and absorption efficiency (through the size of the particles). A smaller Ångstrøm exponent, at constant SSA and optical depth (indicative of larger particles), leads to stronger absorption.

2.3.2 Conceptual approach to self-lifting

The above presented theory is based on strong simplifications. The aerosol-filled layer had a constant absorption and therewith warming rate. It remained intact and undiluted and lifting was instantaneous. Long wave cooling was neglected.
Taking the dynamics of a diluting plume into account leads to a number of different effects on the plume. Herring and Hobbs (1994) conducted an observational study of radiatively induced self-lifting of the Kuwait oil fires together with radiative transfer calculations. In addition, they introduced two concepts for the description of the main dynamic behaviour of a heated aerosol layer: entrainment/encroachment and lifting of the entire layer.

Entrainment/encroachment

They used an analogy to a study by Lilly (1988), who explored the dynamics of upper tropospheric cirrus outflow. The cirrus layer showed a strong IR heating that decreased rapidly with height. This strong vertical gradient of the heating rate in the cloud should generate a convectively mixed layer.
The temporal evolution of such a convectively mixed cloud layer is shown in Figure 2.5. For now, lifting of the entire layer is ignored. The background atmosphere is stably stratified. Through the vertical gradient of the heating rate, the stability in the cloud is decreased, generating a nearly neutrally stable, well mixed cloud layer and strong temperature inversions at the top and the bottom of the layer. Entrainment takes place at both boundaries, causing the layer to grow both at the bottom and the top boundaries. The layer stays thoroughly mixed.
Unless the entrainment at the bottom boundary is extremely strong, the temperature of the layer increases. The strength of the inversion increases at the bottom and decreases at the top. The growth rate at the top boundary is larger since the inversion is weaker. If the temperature of the layer has increased enough, the inversion at the top boundary is nearly removed, causing the cloud layer to grow rapidly in depth. Herring and Hobbs (1994) called this situation of a nearly removed upper temperature inversion the encroachment condition.
In contrast to cirrus clouds, wildfire aerosol layers are heated by SW radiation from above the layer. Thus, the heating rate of a mixed aerosol layer would increase with altitude. However, aerosol layers are never perfectly mixed and thus, the aerosol concentration at the top of the layer decreases with altitude, causing the heating rate to decrease as well. If a mixed aerosol layer would be assumed as initial condition, the encroachment condition would be reached right away and the strong inversion at the top would restore a layer with decreasing concentration with altitude, guaranteeing the applicability of Lilly's concept to SW absorbing aerosol layers.
The overall effect of the radiation absorption in this conceptual approach is a layer that is growing more rapidly at the top than at the bottom, causing the layers mean altitude to slowly increase over time and grow towards bigger heights. However, the growth of the layer is connected to a dilution of the layer so that the absorption of

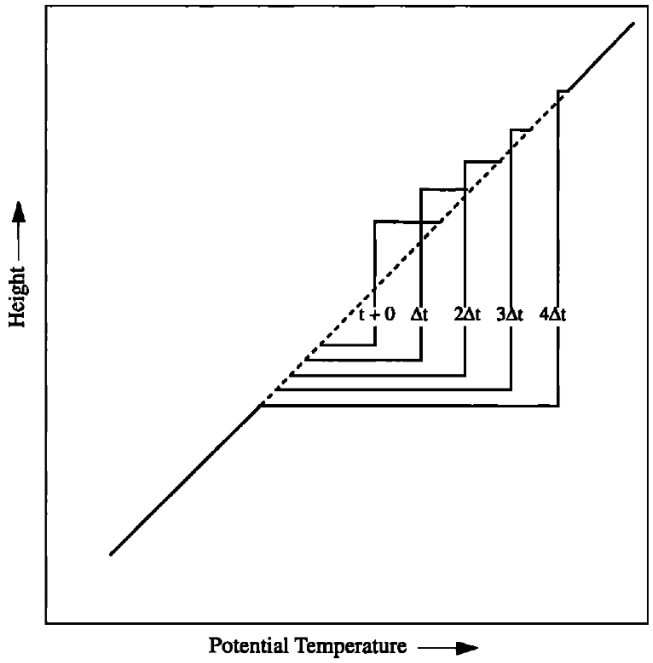

Figure 2.5: Temporal development of the potential temperature profile for a radiatively heated cirrus cloud layer with decreasing heating rate with altitude. The dashed line shows the unperturbed background profile, the solid lines show the profile for consecutive time-steps. The layer is assumed to be thoroughly mixed. Lifting of the entire layer is ignored. Figure from Herring and Hobbs (1994).

SW radiation per volume decreases rapidly and after a while, the entire mechanism is overcome.

Lifting of the entire layer

So far, lifting of the entire layer has been ignored. For this, Herring and Hobbs (1994) again used the analogy to the study by Lilly (1988). Lilly explored the possibility of large-scale lifting of the entire layer through an analogy to a large, flat buoyant plate, moving through a stably stratified fluid.
A balancing flow around the plate is necessary to compensate for the lifting. This is in analogy to moving a thin plate through a bucket of water. Thin jets form in front and behind the plate. If this would not be the case, a vacuum would be produced below the plate.
The aerodynamic resistance to such a compensating jet around a large buoyant layer slows down the lifting rate of the layer and is even larger in a stably stratified fluid, than it would be in a neutrally stratified fluid. An illustration of this concept is shown in Figure 2.6. Thin jets are visible at the top and the bottom of the layer. In addition, the temperature profile is perturbed. The layer drags along some air and causes an adiabatic cooling of the air above and below the layer. Herring and Hobbs (1994) argued that the rate for this type of lifting was proportional to the layers magnitude and inversely proportional to its horizontal width.

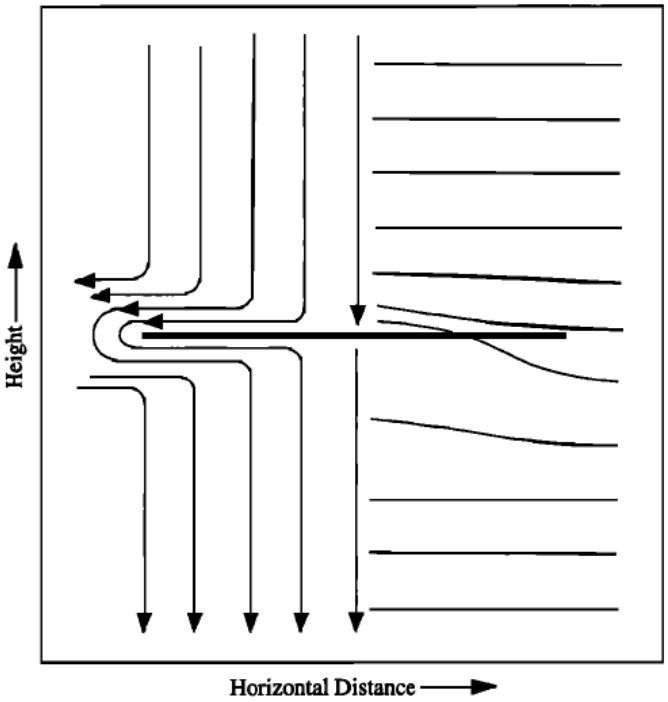

Figure 2.6: Flow pattern (left) and levels of constant potential temperature (right) for the lifting of a thin plate. The plate is assumed to be massive, corresponding to an undiluted aerosol layer. Figure from Herring and Hobbs (1994).

When both mechanisms are combined, the lifting of the entire plume would cause an adiabatic cooling of the layer that would keep it from reaching the encroachment condition. If the plume is, however, extended enough, the lifting would be too slow and entrainment would be the main mechanism for the layer top to gain altitude. Both cases would lead to an aerosol layer that lifts itself and gets diluted at the upper boundary. Fiebig et al. (2003) found evidence of such a profile in a wildfire aerosol layer during the LACE98 campaign. Boers et al. (2010) ignored the entrainment of air and the aerodynamic resistance of the layer in their theoretical study.
For extended plumes, Herring and Hobbs (1994) concluded that the layer would break into smaller (dry-convective) cells that can be lifted more efficiently, as studied by Ghan (1989a,b). In 2-D simulations, this created cells of sizes from 100 to 500 km in a plume, several thousand kilometres wide. For smaller plumes, no such cells were observed.

2.4 Aerosol effects on earth's radiation budget

It is common to distinguish between three types of aerosol effects on the earth's energy budget: the direct effect, the indirect effects and the semi-direct effect.

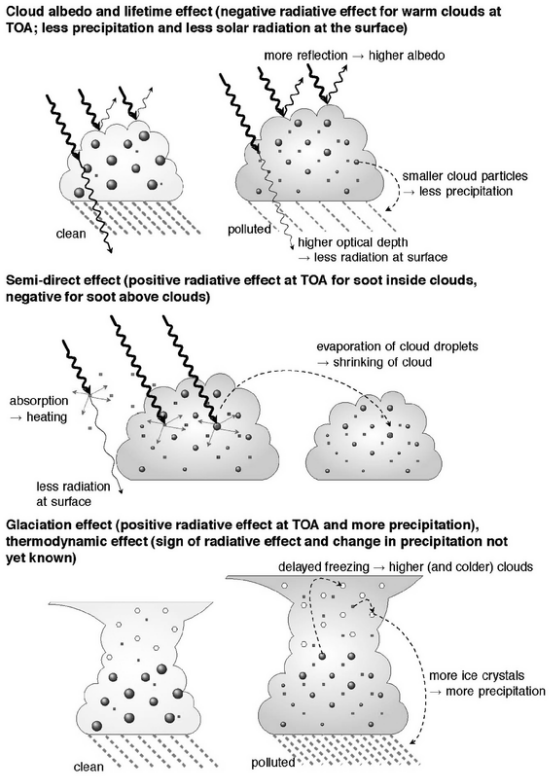

Figure 2.7: Top panel: cloud albedo and lifetime aerosol indirect effects. Centre panel: semi-direct aerosol effect. Bottom panel: glaciation and thermodynamic aerosol indirect effects. Figure from Forster et al. (2007).

2.4.1 Direct aerosol effect

Scattering aerosols above a darker surface lead to a negative radiative forcing, since they increase the SW albedo of the entire earth atmosphere system. Absorbing aerosols warm the surrounding air and cause a positive radiative forcing.

2.4.2 Indirect aerosol effects

Many aerosol types are effective cloud condensation nuclei. In clouds, an abundance of aerosols and therewith cloud condensation nuclei leads to an increased number of cloud droplets, reducing the mean effective radius of the droplets. The cloud optical depth is inversely related to the mean effective radius under the assumption of constant cloud water content. Thus, a higher cloud droplet number with the same cloud water content leads to an optically thicker cloud.
An optically thicker cloud has an increased albedo [Twomey (2007)]. Usually, the

underlying surface underneath a cloud has a lower albedo than clouds. An increased cloud albedo therefore leads to a negative SW radiative forcing. This effect is called the first indirect aerosol effect or Twomey effect.
The increased number of cloud droplets at constant cloud water content slows down the rate of collision and coalescence within the cloud (the onset of precipitation is directly dependent on the maximum droplet size within the cloud [Rogers and Yau (1988)]). Thus, a lower rate of collision and coalescence leads to smaller droplets. A cloud that contains more cloud condensation nuclei can contain a higher cloud water content without loosing water to rain. This increases the lifetime of the cloud, but also the maximum cloud water content that a cloud can reach. As for the first indirect effect, a cloud with an increased optical depth has an increased albedo and therewith an increased radiative forcing that is dependent on the underlying surface. This effect is called the second indirect aerosol effect.
Both indirect aerosol effects are dependent on the previous abundance of cloud condensation nuclei. They are more important for clean air than for polluted air. In addition, they are dependent on, if an aerosol plume can reach the cloud in the first place. An illustration of the indirect aerosol effects is given in Figure 2.7 (top panel).
So far, only increases in the number of cloud condensation nuclei have been discussed. Normally, aerosols from biomass burning are assumed to be poor ice nuclei. However, a recent study by Prenni et al. (2012) came to the conclusion that, even though the fraction of good ice nuclei is very low, at least during the burning phase of a wildfire, a large amount of ice nuclei can be produced. An increase in ice nuclei and thereby in the efficiency of cloud icing can turn a non-precipitating cloud into a precipitating cloud, leading to a positive radiative forcing [Forster et al. (2007)]. This effect is called the glaciation indirect effect. Even though ice nuclei are mostly scarce in the atmosphere, the effect is stronger for originally clean air than for polluted air, making aerosol transport an important issue.
In addition, a freezing of the surplus in cloud droplets caused by the second indirect aerosol effect can lead to a release of more latent heat and thus, a more vigorous convection. The indirect aerosol effects illustrate the importance of a good knowledge of the vertical propagation and lifetime of aerosols. An illustration of the glaciation and the thermodynamic effect is shown in Figure 2.7 (bottom panel).

2.4.3 Semi-direct aerosol effect

The effects on the earth radiation budget from the indirect effects are based solely on the interaction between the aerosols and the clouds, interaction of the aerosols with radiation is not taken into account. However, biomass burning aerosols are light absorbing in the SW range. Because of the multiple scattering within clouds [Liou (2002)], the optical path length is increased, enhancing light absorption.
Through the light absorption, an increase in temperature can happen not only in cloud free regions but also within a cloud. The relative humidity is inversely depen-

dent on the temperature through the saturation vapour pressure [Rogers and Yau (1988)]. Thus, a warming within a cloud reduces the relative humidity and thereby the cloud water content. This effect is called the semi-direct aerosol effect. It has a positive radiative forcing. An illustration of the semi direct aerosol effect is shown in Figure 2.7 (centre panel).
A reduction of the cloud water content also reduces the precipitation efficiency of the cloud. A reduction of the wet-scavenging efficiency is the result.
This effect is, however, only important, if the self-lifting is inefficient. If, however, the radiation absorption causes an efficient lifting, the air does not become warmer relative to the surrounding air. In this case, the self-lifting could cause an increase in the precipitation rate.
An aerosol layer above a cloud leads to a heating of the air and therewith to an increase in stability. The development of convective clouds can be influenced negatively and precipitation is reduced. This leads to a negative radiative forcing.

2.5 LIDAR instruments

(**L**ight **D**etection **A**nd **R**anging) (LIDAR) instuments (short LIDARs) are tools for active remote sensing [Liou (2002)]. They allow for ground based vertically resolved measurements, giving them a unique advantage in comparison to e.g. sun-photometers.
The principle behind each LIDAR is the emission of a pulsed laser beam. This laser beam is scattered back either by aerosols (Mie scattering) or by atmospheric gases (Rayleigh and Raman scattering). Only single scattering is assumed for the analysis of LIDAR data. The receiving telescope is most often placed coaxial with the emitted beam. From the telescope, the signal is sent through beam guiding mirrors and finally focussed on the detectors.
The altitude, from which the vertically resolved signal has been backscattered from, can be obtained from the temporal difference between pulse emission and signal detection. The minimum vertical resolution is hereby dependent on the pulse length. It is half the distance that a signal with the speed of light can travel within the pulse length. The pulse frequency should be chosen according to the maximum altitude, from which a signal is expected to be detected from. It needs to be made sure that no overlap exists between the signals from two successive pulses.
The intensity of the backscattered light at the receiving telescope is dependent on four factors:

1. The power of the emitted laser pulse (P_t): the backscattered signal is assumed linear with the pulse energy.

2. The volume backscattering coefficient ($\beta_\pi(r)$): the density of air and thus, the Rayleigh and Raman volume scattering coefficients are decreasing with altitude. The Mie scattering coefficient is dependent on the existence of aerosol layers.

3. The integrated volume extinction coefficient ($\beta_e(r)$): air molecules and aerosols cause extinction on the way through the atmosphere in upward and downward direction.

4. The distance (r) of the scattering volume from the receiving telescope: scattering is assumed isotropic for the small solid angle that is covered by the receiving telescope. Thus, the intensity at the receiving telescope decreases with the fraction of the sphere from the scatterer with distance r that is covered by the telescope, resulting in a decrease of the signal strength with r^2.

Full overlap is assumed between the detection unit's field of view and the laser beam. For use under daylight conditions, it is necessary to use narrow enough filters in front of the detectors to reduce background light pollution of the signal. Otherwise, the background light intensity would be higher than the actual signal.
As already mentioned in Section 2.2, the Rayleigh cross section for IR radiation is much smaller than for visible light. Thus, aerosol layers are better recognisable in the IR.

2.5.1 LIDAR equation and depolarization ratio

The LIDAR equation describes the relation between the emitted signal, the atmospheric composition and the detected signal. It is a non-linear differential equation. The full LIDAR equation under the assumption of pure single scattering describes the power at the detectors to be [Liou (2002)]

$$\bar{P}_r(r) = \frac{P_t C A_r \beta_\pi(r) \Delta h}{8\pi r^2} \cdot exp\{-2 \int_0^r \beta_e(r')\, dr'\} + B, \tag{2.8}$$

with

P_t	laser transmitted power $[W]$
C	an instrument factor
A_r	collecting aperture $[m^2]$
$\beta_\pi(r)$	height dependent volume backscattering coefficient $[\frac{1}{m}]$
Δh	layer thickness (height resolution) $[m]$
r	distance from the LIDAR (height) $[m]$
$\beta_e(r')$	height dependent volume extinction coefficient $[\frac{1}{m}]$
B	background signal from the detector's dark current and background light. $[W]$

The coefficients $\beta_\pi(r)$ and $\beta_e(r')$, describing the atmosphere's composition, consist of two terms: one for aerosols, denoted as $\beta_{\pi A}(r)$ and $\beta_{eA}(r')$ and one for air molecules, denoted as $\beta_{\pi R}(r)$ and $\beta_{eR}(r')$, respectively. The molecular backscattering and extinction for the LIDAR wavelengths is assumed to be pure Rayleigh single scattering. Replacing the initial coefficients with a combination of the new, separate

coefficients, the LIDAR equation becomes

$$\bar{P}_r(r) = \frac{P_t C A_r (\beta_{\pi A}(r) + \beta_{\pi R}(r)) \Delta h}{8\pi r^2} \cdot exp\{-2 \int_0^r (\beta_{eA}(r') + \beta_{eR}(r'))\, dr'\} + B. \quad (2.9)$$

A height resolved profile is reached through the emission of a pulsed signal. The height, the signal is coming from, can be retrieved from the speed of light and the time difference between the emission and the detection of the signal.
The 532 nm linear **P**article **D**epolarization **R**atio (PDR) [Freudenthaler et al. (2009)] is defined as

$$\delta_p = \frac{\beta_{\pi A,s}(r)}{\beta_{\pi A,p}(r)}, \quad (2.10)$$

with $\beta_{\pi A,s}(r)$ and $\beta_{\pi A,p}(r)$ the height dependent aerosol backscattering coefficient for s- and p-polarised light. The PDR states, how much of the light that is backscattered at a particle, changes linear polarisation direction from parallel to perpendicular. It contains information on the shape of the particles. For perfectly spherical particles, the PDR would be close to 0, for highly non-spherical particles, such as volcanic ash and most cloud types, it is high (> 0.15). Murayama et al. (2004) reported maximum PDR values for aged biomass burning plumes of 0.06 - 0.08.
The linear **V**olume **D**epolarisation **R**atio (VDR) is a mixed term containing the PDR and the Rayleigh depolarisation ratio [Bates (1984)]. The VDR states, how much of the light that is backscattered in a volume, containing particles and gases, changes linear polarisation direction from parallel to perpendicular. It is defined as

$$\delta_v = \frac{P_s(r)}{P_p(r)} = \frac{\beta_{\pi A,s}(r) + \beta_{\pi R,s}(r)}{\beta_{\pi A,p}(r) + \beta_{\pi R,p}(r)}. \quad (2.11)$$

Rayleigh depolarisation is weaker than particle depolarisation, resulting in a smaller VDR than PDR. For high particle backscattering coefficients, the Rayleigh backscattering coefficient is comparatively small and the differences between PDR and VDR become small. It is easier to calculate the VDR than the PDR. Since the VDR is smaller than the PDR, layers with a high VDR can be separated out as non-biomass burning layers.
The basic principle of LIDARs is linearity. The LIDAR equation is linear in P_t. A dead-time correction is necessary for the photon counting channels to assure linearity (Appendix A.2). Otherwise, signal detection is assumed to be linear with intensity within the detector ranges.

2.6 Atmospheric models

One basis of the description of atmospheric processes is the continuity equation

$$\frac{\partial \mu}{\partial t} + \vec{v} \cdot \vec{\nabla} \mu = S, \quad (2.12)$$

for different kinds of tracers, such as momentum, mass, moisture, and chemical tracers, with μ the tracer, S sources and sinks, $\vec{v}$ the three dimensional wind velocities

and ∇ the differential operator. The continuity equation is non-linear and can therefore not be solved analytically for most applications. Instead, numerical models are necessary.
Normally, one distinguishes between two main kinds of processes in the simulation of atmospheric processes: chemical processes and meteorological processes. Meteorological processes are described by the continuity equations for meteorological tracers, such as momentum, mass, energy, moisture and temperature. Chemical processes are described by the continuity equation for chemical tracers. In this work, the focus lies on the chemical tracer transport and is therefore described in somewhat more detail. There are two main types of models for the simulation of transport of chemical tracers: Eulerian and Lagrangian models.

2.6.1 Eulerian models

Eulerian models are based on observers that are fixed at discrete points in space. For this, the simulation domain is divided into a regular grid in the three spatial directions. Eulerian chemistry transport models can be run in two modes: offline and online. Offline means that the chemical species do not have any influence on the meteorological conditions, such as wind and moisture. In offline simulations, the meteorological conditions can be given a priori. In online simulations, full interaction is simulated between the chemical species and the meteorological conditions. Hence, meteorological conditions can vary during interaction with the chemical species (such as the vertical wind through absorption of SW radiation by aerosols) and therefore, are always calculated during the simulation. However, because of the chaotic nature of the atmosphere, it can be necessary to force the meteorological conditions towards observations by using nudging.
Since the domain is divided into a discrete grid, the resolution of an Eulerian model is always finite. This can have disadvantages, when e.g. assuming a point source in a large grid-box. The point source instantaneously becomes a volume source. In addition, Eulerian models can show numerical diffusion. Stability criteria dictate the time-step and with that, the computational efficiency.

2.6.2 Lagrangian models

Lagrangian models are based on observers that are fixed on air parcels. They do not have a gridded computational domain.
Lagrangian transport models are run offline. The meteorological conditions such as winds, temperature and moisture are given as gridded input data. Therefore, Lagrangian models cannot simulate an influence of chemical species on the meteorological conditions.
Since those models use a priori meteorological conditions as input, they can be referred to as linear. The position of each air parcel in the next time-step is predetermined by the current position. Therefore, it is possible to run Lagrangian models in both backward- and forward-mode, meaning that the simulation can start at the

release location and run forward in time or at a receptor location and run backwards in time. Only linear chemical processes are simulated in Lagrangian models.
In theory, Lagrangian models have an infinitesimally fine resolution. They do not show any numerical diffusion and are always stable.
There are two main types of Lagrangian models that are currently used in atmospheric sciences: Trajectory models and particle dispersion models.
Trajectory models calculate the trajectories of single particles. They follow a fully deterministic approach. That means, given the time-varying wind-field, the end point of the trajectory is entirely dependent on the exact starting location. This can lead to large errors in the transport directions. A method to avoid this, is to start a large number of trajectories. This, however, lessens the advantage of the high computational efficiency of the trajectory models.
Particle dispersion models calculate the trajectories of a large number of particles superimposed with stochastic random motions representing turbulent dispersion. Thus, even if started at one point, the particles automatically end up at different positions. This has the advantage that actual plumes can be simulated.

Chapter 3

Materials and Methods

The main methods and datasets that were used during this work are described and discussed here, some additional information is given in the Appendix. The data evaluation was done using Matlab, except for a few online tools. For the larger datasets, the data evaluation was split into single subroutines to make the code more manageable and easier to read.

3.1 ALOMAR troposphere LIDAR

The ALOMAR troposphere LIDAR was used to identify aerosol layers in the air above the ALOMAR research facility.

3.1.1 ALOMAR

The **A**rctic **L**idar **O**bservatory for **M**iddle **A**tmosphere **R**esearch (ALOMAR) is a research facility for remote sensing of the atmosphere at high latitudes. It is part of **A**ndøya **R**ocket **R**ange (ARR), which provides launch facilities for rocket and balloon missions. The ALOMAR observatory was built in 1994 as a cooperation of international institutes. It is located at 69°16'42"N and 16°00'31"E at an elevation of 380 m, on top of Raman mountain [ALOMAR (2012)].
With its location at high latitudes, about 70 km off the coast of Norway and 380 meters above sea level, it can be used as a complementing station to Arctic stations like Ny Ålesund, Alert or Barrow for transport from and to the Arctic.
The observatory is well suited for optical investigations of phenomena in the Arctic atmosphere, such as noctilucent clouds in the mesosphere [Fiedler et al. (2003)], the depletion of ozone in the Arctic stratosphere [Manney et al. (2011)] and tropospheric events, such as Arctic haze or direct long-range transport of pollutants.
At the moment, ALOMAR hosts four LIDAR systems: the **R**ayleigh-**M**ie-**R**aman (RMR) LIDAR (owned by Leibniz-**I**nstitut für **A**tmosphären**P**hysik (IAP)), the Sodium LIDAR (owned by Gats in Boulder, Colorado), the Ozone LIDAR (owned

by ALOMAR) and the Troposphere LIDAR. Additionally, there are other instruments on site (e.g. a sun-photometer and several radar instruments).
Several parts of the LIDAR instruments are highly sensitive to external influences. The main mirrors of the receiving telescopes could e.g. be influenced or even degraded by sea-salt. The LIDARs are placed in a telescope hall with a hatch that is only opened during suitable conditions.

3.1.2 Alomar troposphere LIDAR

The ALOMAR troposphere LIDAR was installed in 2005. It is operated by ALOMAR and **U**niversitetet **i** **O**slo (UiO).
The LIDAR consists of three main parts: the transmission, the reception and the acquisition unit [Frioud et al. (2006), Koelbl (2010)]. A schematic and a specification data sheet are given in Appendix A.1. A detailed description of the LIDAR components is given in Appendix A.2.
As mentioned in the last subsection, the measurement hours of all ALOMAR LIDARs are restricted to favourable conditions in terms of wind and moisture. The troposphere LIDAR's measurement time is further restricted by low clouds. The ALOMAR troposphere LIDAR is designed for maximum sensitivity so that measurements can be made up to altitudes of 20 km. Nonlinearities in the signal or even a degradation of the detectors could be the result of strong backscattering signal from low clouds. To avoid negative influences on the detectors, a grey filter could be used, if measurements should be taken underneath low clouds.
The LIDAR equation was introduced in Section 2.5.1. It is a non-linear differential equation in height. It is not possible to calculate the desired variables by solving the equation analytically. Instead, an inversion method needs to be used that makes assumptions on the relationship between the height dependent variables. Several different inversion algorithms have been developed over the years [Fernald (1984) and Ansmann et al. (1992)]. An algorithm for the ALOMAR troposphere LIDAR is under development but was not available at the time of this work. It was not crucial to perform a full inversion to retrieve the plumes' temporal and spatial extents and VDR. An approximation of the PDR was calculated for the case study. A partial inversion was developed for this purpose.

3.1.3 Raw data treatment

Beginning with the full LIDAR equation (eq. 2.9), the first step was the dead time correction of the raw signals in the photon counting channels (Subsection A.2.3). The detector's dead time was $\tau_d = 3.7\ ns$. The observed count rate (N) differed from the true count rate (S) by [Licel (2011)]

$$N = \frac{S}{1 + S \cdot \tau_d}. \tag{3.1}$$

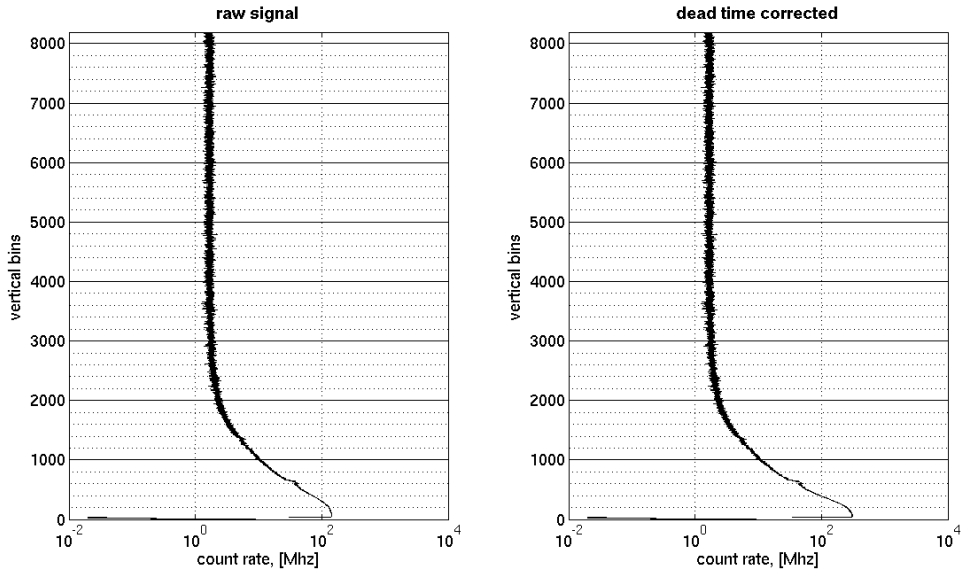

Figure 3.1: Left panel: raw-data example of the 532 nm p-polarised LIDAR signal from June 24, 2010. Right panel: dead time corrected raw signal. Differences are only visible in the signal strength in the lowermost 1000 bins. The differences at greater altitudes increase strongly after the dead-time correction.

An inversion of equation (3.1) resulted in the true count rate

$$S = \frac{N}{1 - N \cdot \tau_d}. \tag{3.2}$$

A raw-data signal from June 24, 2010 is shown in Figure 3.1, left panel. The dead time corrected signal is shown in the same figure (Figure 3.1, right panel).

The next step was the subtraction of the background signal. Background mostly consists of the detector's dark current and the background light in the atmosphere. On short time scales (a few laser shots), the background signal was assumed constant in time and thus, constant in altitude. The highest bin corresponded to an altitude of around 61500 m above ground. There are LIDAR systems at ALOMAR that can detect signals this high. However, no signal was assumed to be detected with the troposphere LIDAR from altitudes above 40 km [Gausa (2011)]. The last $\frac{1}{5}$ of the bins was assumed to be pure background. The signal from that range was averaged and subtracted from each channel in every time-step. The resulting signal is shown in Figure 3.2 (left panel).

An averaging filter was used to achieve a better signal to noise ratio. The filter was a 1-2-1 filter type that was extended to a 1-1-4-8-4-1-1 filter with a variable number of iterations. A discussion of the filter design and function is given in Appendix A.3. The next step was the calculation of the **R**ange **C**orrected **S**ignal (RCS). For this, the LIDAR equation was multiplied with r^2. The remaining constant factors were combined to one instrument factor K, resulting in a new version of the LIDAR equation

$$\bar{P}_r(r) = K \cdot (\beta_{\pi A}(r) + \beta_{\pi R}(r)) \cdot exp\{-2 \int_0^r (\beta_{eA}(r') + \beta_{eR}(r'))\, dr'\}. \tag{3.3}$$

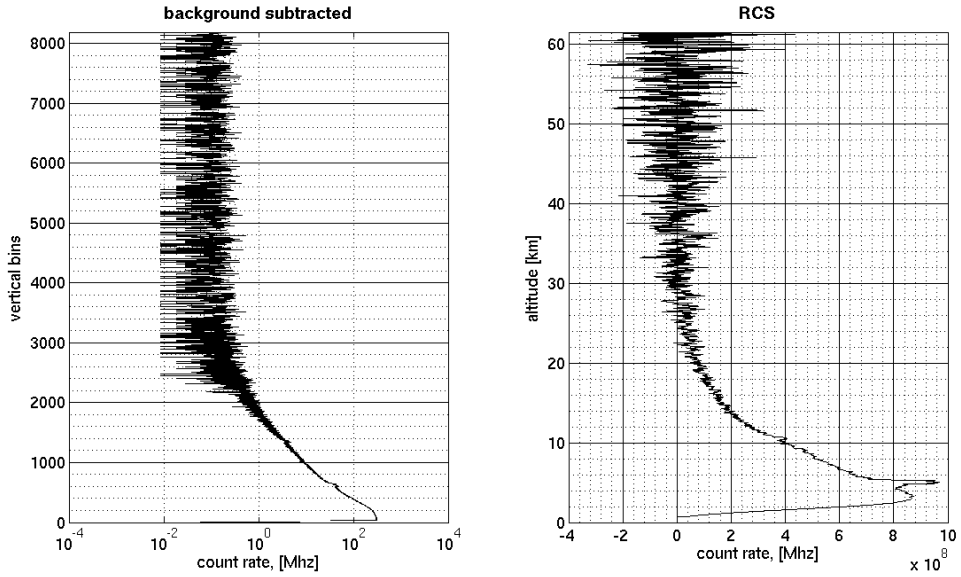

Figure 3.2: Left panel: absolute value of the dead time corrected and background subtracted raw signal for the same data set as shown in Figure 3.1. The signal above 6500 bins is zero in average. Negative values are not shown because of the logarithmic scale. Right panel: dead-time corrected, background subtracted and filtered range corrected signal. Because of the r^2 multiplication during the range correction, the signal to noise ratio falls quickly with height.

For technical reasons, the acquisition of the analogue channels occured with a temporal delay relative to the photon counting channels [Guan (2011)], causing the first bin of the analogue channels to be detected temporally coinciding with the fourth bin of the photon counting channels. To correct for this, the first three bins were removed from the analogue channels. The total offset for all LIDAR channels was 34 m above ground. The vertical resolution was 7.5 m and the surface elevation at ALOMAR was 380 m above sea level. Thus, the vertical axis extended from 414 m to around 61800 m. The RCS for the example is shown in Figure 3.2 (right panel).

3.1.4 Identification of potential aerosol layers

Potential aerosol layers were identified at this point. For that, time-resolved and time-averaged plots of the first 2000 bins were produced for the elastic 532 nm and 1064 nm channels. Datasets from each day could consist of several subsets with varying lengths and breaks. The breaks between the subsets were either caused by weather (clouds or wind) or by maintenance work on the LIDAR system. An example of a potential aerosol layer is given in Figure 3.3. Four data sets were collected through the day. A potential aerosol layer was found in the fourth data set. The layer can clearly be recognised at an altitude of about 5 km. The same layer was observed in the raw-data around 600 bins from the ground as a very weak

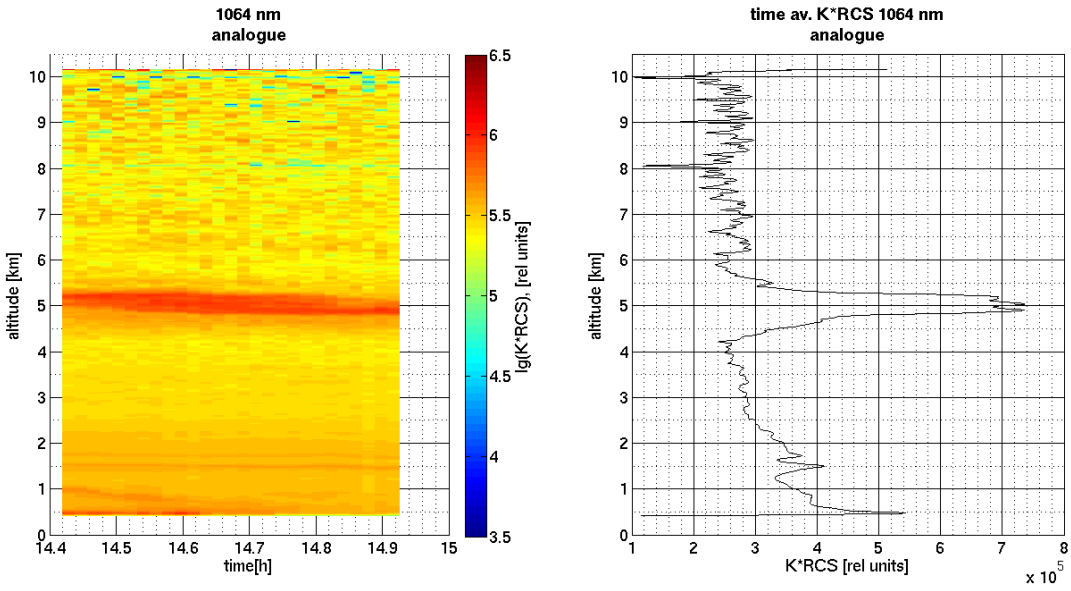

Figure 3.3: Left panel: logarithmic time-resolved profile of the 1064 nm *RCS* [relative units], x-axis: hour of the day, y-axis: altitude above sea level. Right panel: time-averaged profile of the 1064 nm *RCS* [relative units], x-axis: signal strength, y-axis: altitude above sea level. The signal is cut off above 10 km.
A potential aerosol layer is clearly visible around 5 km. The same layer was already visible in Figure 3.2. However, the layer was much less prominent because of the non-linearity of the photon counting detection mode for strong signals and a stronger contribution to the total signal from Rayleigh scattering.

peak. The layer became more visible in the RCS.

3.1.5 PDR and VDR calculation

Signal calibration

The instrument factor K in Equation (3.3) was unknown. However, it was not necessary to determine K for the identification of potential aerosol layers and the calculation of the VDR and the PDR, it was sufficient to estimate the ratio of K between the s- and p-polarized channels in Equation (3.3).
K was different for the s- and p-polarized channels because of different extinction in the optics after the two channels have been split in the PBS (Appendix A.2) and different detector gain. A minor difference could also have been caused by non-parallelism between the laser linear polarisation and the PBS and possibly a changing angle of the laser polarisation during the first hour of measurements. A calibration of the two channels relative to each other was necessary.
For 2011, a separate depolarisation calibration procedure based on the MPF (Appendix A.2) was available. For 2010, the calibration procedure has not yet been installed. Instead, a calibration was used that was based on the assumption of pure Rayleigh signal (no aerosols) within the stratosphere. Both methods are described

and discussed in Appendix A.4.
After the calibration procedure, the factor K was neglected for the p- and s-polarized channels, leading to a new set of equations

$$\bar{P'}_s(r) = (\beta_{\pi A,s}(r) + \beta_{\pi R,s}(r)) \cdot exp\{-2 \int_0^r (\beta_{eA,s}(r') + \beta_{eR,s}(r'))\, dr'\} \tag{3.4}$$

$$\bar{P'}_p(r) = (\beta_{\pi A,p}(r) + \beta_{\pi R,p}(r)) \cdot exp\{-2 \int_0^r (\beta_{eA,p}(r') + \beta_{eR,p}(r'))\, dr'\}. \tag{3.5}$$

It has to be emphasized that these equations are only valid for the retrieval of relative values between $\bar{P'}_s(r)$ and $\bar{P'}_p(r)$.

VDR calculation

The VDR was calculated by a simple division $\frac{\bar{P'}_s(r)}{\bar{P'}_p(r)}$, under the assumption of equal extinction coefficients for the p- and s- polarized light. This assumption can be violated for stably aligned ice particles. However, the scope of this thesis was not the characterisation of ice clouds, justifying the above assumption.

PDR calculation

To calculate the PDR, the influences of Rayleigh single scattering and Rayleigh extinction needed to be removed from the RCS of the 532 nm channels. The altitude dependent Rayleigh extinction correction factor

$$\beta_{eR}(r) = exp\{-2 \int_0^r (\beta_{em} \cdot N(r'))\, dr'\}, \tag{3.6}$$

(with N the number of air molecules) was calculated, using an atmospheric density profile and the molecular extinction cross section of air $\beta_{em} = 5.1517 \cdot 10^{-27}\, cm^2$ [Bates (1984)]. The Rayleigh extinction was removed from the p- and s-polarised channels separately by multiplication of Equation (3.6) with Equation (3.5). To remove the contribution from Rayleigh single scattering, the atmospheric density profile was fitted to the **B**ackground subtracted, **H**eight corrected and **R**ayleigh extinction (BHR) corrected LIDAR equations

$$\bar{P'}_s(r) = (\beta_{\pi A,s}(r) + \beta_{\pi R,s}(r)) \cdot exp\{-2 \int_0^r (\beta_{eA,s}(r'))\, dr'\}. \tag{3.7}$$

and

$$\bar{P'}_p(r) = (\beta_{\pi A,p}(r) + \beta_{\pi R,p}(r)) \cdot exp\{-2 \int_0^r (\beta_{eA,p}(r'))\, dr'\}. \tag{3.8}$$

A subtraction of the Rayleigh fit from the BHR corrected signal yielded an approximation to equations that were only dependent on aerosol single scattering and extinction

$$\bar{P}_{r,p}(r) = \beta_{\pi A,p}(r) \cdot exp\{-2 \int_0^r (\beta_{eA,p}(r')\, dr'\} \tag{3.9}$$

and

$$\bar{P}_{r,s}(r) = \beta_{\pi A,s}(r) \cdot exp\{-2 \int_0^r (\beta_{eA,s}(r')\, dr'\}. \tag{3.10}$$

The Rayleigh single scattering signal was still attenuated by aerosol extinction. However, the error from neglecting the aerosol extinction was small, since only plumes with low extinction cross sections were analysed (strong clouds for example showed a step in the backgound profile at the cloud layer indicating strong extinction). A division $\frac{\bar{P}_{r\ 532\ s}(r)}{\bar{P}_{r\ 532\ p}(r)}$ yielded Equation 2.10 for the PDR.

3.1.6 Glueing and noise problems

In Section 2.5.1, it was explained that signal detection is assumed linear in the detectors range. The LIDAR equation has an r^2 dependence, leading to a range of several orders in signal strength from the troposphere and the stratosphere. Neither the analogue nor the photon counting detection mode cover such a wide range on their own. For the signal calibration on the basis of the Rayleigh signal and for the calculation of the PDR, it was necessary to have a signal valid in the troposphere and the stratosphere. Thus, the signals of both detection modes were combined, extending the dynamic range of the LIDAR through the troposphere and most parts of the stratosphere.
For this, the analogue signal was fitted on the range corrected photon counting signal in a range, where both were valid. This method is called glueing, since the signal from the shorter-range analogue signal is glued together with the longer-range photon counting signal.
Glueing had to be done with a special software by ALOMAR staff and was therefore only done for the case-study. The glued data were already averaged over time, the remaining raw-data treatment was the same as described above.
Some of the datasets showed electronic noise. Examples for the different kinds are given in Appendix A.6. Measurements with strong electronic noise were sorted out manually.

3.2 SYNOP data

Surface **SYNOP**tic (SYNOP) observations were used as an additional tool to distinguish between aerosol layers and clouds, when detected with the ALOMAR troposphere LIDAR. SYNOP data are written in a code which makes them internationally understandable and short (information on how to read SYNOP code can be found in various sources [Weather (2012)]). They contain detailed information on e.g. wind velocity, precipitation and clouds. For this work, the information on cloud coverage was used to determine, wether a layer was a cloud or an aerosol layer.
Aerosol layers, in contrast to most types of clouds, can often not be seen by the naked eye, especially after long-range transport. The limitation of SYNOP data is reached for optically very thin clouds and for very thick aerosol layers [Forster et al.

(2001)]. Cloud coverage is given in oktas ($\frac{1}{8}$ of the sky). Only cloud coverage of 8 oktas, corresponding to full coverage, can guarantee that a cloud will be seen by the LIDAR. Thus, SYNOP data could only be used for the elimination of clouds.
The cloud observations for this work were manual observations. Data sets, including a translation, can be found under Mundomanz (2012). 1-hourly datasets without translation can be found under Valor (2012). The code for Andøya **W**orld **M**eteorological **O**rganization (WMO) station is *01010*.

SI 24/06/2010 15:00->
AAXX 24151 01010 41589 **1**0204 10089 20045 30165 40181 58006 70221 **81831**=

is an example of SYNOP code from the measurement time of the above example. The conditions were relatively clear sky with total cloud coverage of one okta. Cumulus humilis clouds covered one okta of the lower troposphere (with cloud base below 2000 m). Altocumulus translucidus clouds (mostly transparent) covered a maximum of 1 okta of the middle troposphere (with cloud base between 2000 m and 3000 m). Cirrus fibratus clouds covered a maximum of 1 okta of the upper troposphere (with cloud base above 3000 m). When this information was compared to the examples in Section 3.1.4, it was concluded that the measured layer was not a cloud signal, since a fine substructure of the clouds would have been visible. The observed layer was even, indicating an extended aerosol layer.

3.3 Radio-soundings from Bodø airport

Radio-soundings from Bodø airport radio-sonde station were used to distinguish between aerosol layers and thin cirrus clouds when detected with the ALOMAR troposphere LIDAR. Balloon soundings are released from Bodø airport radio-sonde station every 12h. During flight time, radio-sondes measure the temperature, relative humidity and pressure. Together with the GPS data, the wind speed and direction, the dew point temperature and the water mass mixing ratio on the flight track are calculated and stored in an archive.
The radio-sonde data for this work were downloaded from the University of Wyoming web page [University of Wyoming (2012)]. The web page provides radio-sonde data already plotted on a Tephigram together with the dew point temperature.
There are some disadvantages, regarding the use of radio-soundings. A low number of water molecules and low temperatures limit the accuracy of relative humidity retrievals at high altitudes. Therefore, saturation could be reached, even if the dew point and the temperature curve did not intersect but are only close. The Bodø radio-sonde station was relatively far away from Andøya (ca. 250 km). Hence, it could happen that there were clouds in Bodø but no clouds above ALOMAR or vice versa. The last restriction was the low temporal resolution of the radio-sonde data of 12h and the fact that on rare occasions, no sounding data were available at all.

3.4 MODIS

MODIS is an instrument that is flown on both the Terra and Aqua satellites, as part of NASA's Earth Observing System. The **MOD**erate-Resolution **I**maging **S**pectroradiometer (MODIS) detects radiation that is either emitted or backscattered from the ground, the ocean or the atmosphere. It detects 36 wavelength bands in a range from 620 nm to 14385 nm. Most of the bands have a horizontal resolution at ground of 1000 m [NASA (2012c)]. MODIS data are used for a wide variety of applications. In this work, three types of MODIS data were included in the identification of wildfire plumes, one formed the basis for the speciation of biomass burning emissions in WRF-Chem (Section 3.10) and one contained information on the column integrated AOD.
The speciation of emissions in WRF-Chem is described in Section 3.10.3, the remaining 4 datasets are described in the following sections. A description of the basic fire detection algorithm underlying all MODIS wildfire data can be found in Giglio et al. (2003). A description of the MODIS AOD retrievals can be found in Remer et al. (2005).
By having the same instrument flown on two satellites, MODIS scans the entire earth's surface every 1 to 2 days. Thereby, it is likely that the same fires are counted more than once during a day. This could lead to an overestimation of fire sizes or emissions. If data sets from both satellites are used, a correction needs to be included for that effect.
It is beneficial having two satellites, because MODIS cannot detect fires when thick clouds are covering the fire. Then, the long wave radiation is blocked and cannot reach the satellite. With two successive overflights, the likelihood of a fire detection during cloud free conditions is higher. This is directly used as part of the cloud correction algorithm. In addition, short lived fires are less likely to be missed when the surface is scanned twice a day.
The advantage in the combination of both satellites is that the likelihood for fire detection is higher, because spots will be scanned at two different times. Both satellites are in sun-synchronous near-polar orbit, with Terra passing the equator on descending node (from North to South) at 10:30 a.m. and Aqua passing the equator on ascending node (from South to North) at 1:30 p.m. The orbital period of both satellites is around 98 minutes.

3.4.1 NASA's RRI

NASA's **R**apide **R**esponse **I**magery (RRI) is an online accessible tool [NASA (2012e)]. It was used in addition to a first source determination of plumes with the HYSPLIT model (Section 3.7). MODIS fire counts can be plotted on a fire map with 3 different resolutions. The fire detections of MODIS Terra and MODIS Aqua were combined and corrected as mentioned above. The detection algorithm is similar to the one for the data from the University of Maryland [Giglio et al. (2003)]. Colour markers indicate a detection of at least one fire during the detection period. The colour scale

Layer Name	Data Type	Units	Description
CorrFirePix	int32	-	Corrected number of fire pixels.
CloudCorrFirePix	int32	-	Corrected number of fire pixels, with an additional correction for cloud cover.
MeanCloudFraction	int32	-	Mean Cloud fraction.
RawFirePix	int32	-	Uncorrected count of fire pixels.
CloudPix	int32	-	Number of cloud pixels.
TotalPix	int32	-	Total number of pixels.
MeanPower	float32	-	Mean fire radiative power.

Table 3.1: Summary of data layers in the CMG fire products [Giglio (2010)]

reaches from red markers for a few fire detections to yellow markers for many fire detections. Additional information, like fire size, cannot be accessed with this tool.

3.4.2 MODIS CMG data

MODIS CMG data have been used in the analysis of FLEXPART simulations (Section 3.9). The MODIS **C**limate **M**odeling **G**rid (CMG) data with the highest available resolution (i.e. 8 days and 0.5 degree) were downloaded from the University of Maryland ftp-server [University of Maryland (2012)]. The MODIS data are separated into different collections. The newest collection is version 5. Each 8-day data set consists of an array of size 720x360, containing the gridded variables that are listed under 3.1. There is one dataset available for each satellite.

For the analysis of FLEXPART simulations, the CloudCorrFirePix and the MeanPower of both satellites were used for a visible check if the highest potential emission sensitivity (PES) coincided with fires and to calculate a PSC for the fire pixels and the radiative power (for an explanation of the potential emission sensitivity (PES) and the potential source contribution (PSC), see Section 3.9.2 and 3.9.4). A detailed description of that method is given in Section 3.9.

3.4.3 MODIS daily wildfire data

MODIS daily wildfire data were used for the identification of single fires in combination with FLEXPART simulations and CMG data. Daily fire data provided additional information to an evaluation based solely on 8-day resolution CMG data, since many fires burn less than 8 days. When the FLEXPART source region did not temporally coincide with an actively burning fire and the respective CMG grid point was still marked as a fire, a false positive fire plume identification could have occurred.

The data sets are continuously downloaded by the **N**osk **I**nstitutt for **LU**ftfoskning (NILU) and were provided to the author by Dr. Andreas Stohl.

3.4.4 MODIS AOD

MODIS AOD data at 550 nm were used to validate the simulated AOD from WRF-Chem. Data were downloaded from NASA (2012b). The plots contain MODIS level 3 (quality controlled) data. AOD values were available for the wavelength of 550 nm. A description of the algorithm is given in Remer et al. (2005). The data have a spatial resolution of $1 \times 1^{\circ}$ and a temporal resolution of 1 day for each satellite.
Data were not available for every day and grid-box. Clouds led to missing entries, since they significantly increased the optical depth of a layer and thereby masked all information on aerosols. However, for severe smoke cases it could happen that smoke pixels were misidentified as cloud pixels and therefore data were missing. On the other hand, cases have been found, where clouds were misidentified as high AOD values. MODIS AOD data show some uncertainty since they are based on a complicated set of information on the current atmospheric state and the land use. Some land use types were not suitable for an AOD retrieval, leading to missing values.

3.5 AERONET

There is a sun-photometer on site at ALOMAR. The instrument is part of NASA's **AE**rosol **RO**botic **NET**work (AERONET) and the Spanish **R**ed **I**bérica de **M**edida fotométrica de **A**erosoles (RIMA) network and is maintained by a cooperation between the Universidad de Valladolid, Spain and ALOMAR. The data were retrieved from the AERONET webpage [NASA (2012a)]. AERONET is a global network of CIMEL Electronique 318A spectral radiometers (sun-photometers). Sun-photometers measure the incoming intensity of solar radiation at different wavelengths. For this purpose, they are automatically adjusted towards the sun every 15 minutes.
From the well known earth-sun distance, thickness and gaseous composition of the atmosphere and the solar angle, it can be calculated, how much solar radiation should have reached the ground in clean air conditions. The column integrated AOD can be calculated from the known theoretical and measured solar intensities for the different wavelengths. The Ångstrøm exponent between the wavelengths of 440 and 870 nm was used as a measure of the size of the particles.
Sun-photometer AOD retrievals are more exact than the ones from MODIS. In fact, AERONET is used for calibration of the MODIS algorithms. However, there are also disadvantages connected to sun-photometers: They always have to be pointed towards the sun. That makes a comparison to LIDAR data difficult (the LIDAR is aimed in near-zenith direction). Sun-photometers are static instruments, giving only point measurements. Sun-photometers can only be used during daylight conditions with sufficiently high solar angles.
Plots of AERONET data were at first provided and commented by Dr. Carlos Toledano at the Universidad de Valladolid [Toledano (2012)], Spain and later directly downloaded from the AEORNET web page.

3.6 NCEP weather maps

Surface weather maps and precipitation charts for the U.S. were downloaded from NCEP (2012). They are released by the U.S. **N**ational **C**enters for **E**nvironmental **P**rediction (NCEP).
The weathermaps show operational analysis maps of the sea-level pressure, frontal systems, a freezing line and areas of precipitation. Analysis times for the NCEP weather maps are 07:00 **E**astern **S**tandard **T**ime (EST), corresponding to 02:00 **C**oordinated **U**niversal **T**ime (UTC).
The precipitation charts show the 24-hourly total precipitation in inch, ending at the analysis time for the weather maps.

3.7 HYSPLIT

HYSPLIT was used to get a first impression about the origin of layers that have been detected with the ALOMAR troposphere LIDAR. The **HY**brid **S**ingle **P**article **L**agrangian **I**ntegrated **T**rajectory (HYSPLIT) model is developed and operated by the **A**ir **R**esource **L**aboratory (ARL) [NOAA (2012a)], under the **N**ational **O**ceanic and **A**tmospheric **A**dministration (NOAA) of the US government.
For this work, the web-based version of HYSPLIT: the **R**eal-time **E**nvironmental **A**pplications and **D**isplay s**Y**stem (READY) [NOAA (2012b)] was used. The model itself runs on the ARL system.
HYSPLIT was used for single particle calculations backwards in time from the measurement point (within a layer in the air above ALOMAR at 69.28° N, 16.01° E). Two calculations, each with the maximum number (i.e. three) of backward-trajectories, were done for each layer: one calculation with backward-trajectories starting at different altitudes within the layer and one calculation with backward-trajectories starting underneath, in and above the layer. This was done to achieve a good representation of the main transport directions within and around the potential aerosol layers. Maximum runtime was chosen (315h) with markers every 24h along the backward-trajectories.
Its very short runtime (around 2 minutes) qualified HYSPLIT as a first analysis tool. However, its fully deterministic approach showed disadvantages in comparison to Lagrangian particle dispersion models (Section 2.6).
The **G**lobal **D**ata **A**ssimilation **S**ystem (GDAS) dataset [NOAA (2012c)] was used as meteorological input. It was the only data set with global coverage in 2010 and 2011. The dataset has a temporal resolution of 6 hours and a horizontal resolution of 1°. The HYSPLIT result for the simulation that started within the layer of the example in Section 3.1 is shown in Figure 3.4.

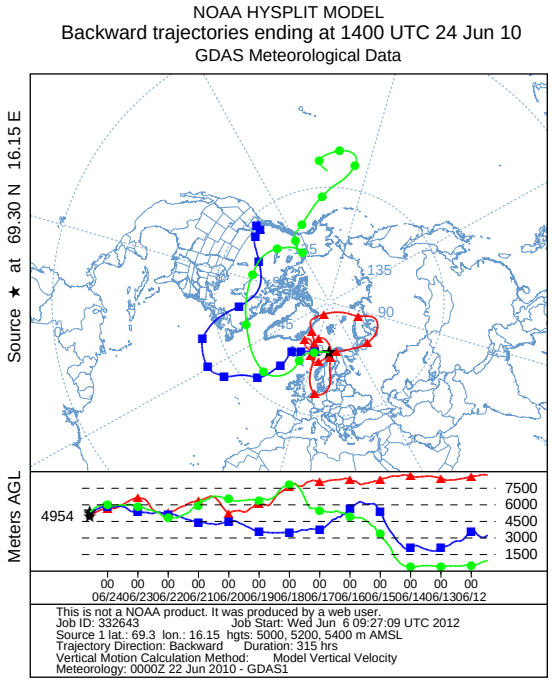

Figure 3.4: HYSPLIT backward-trajectory for June 24, 2010. Backward-trajectories were initialized in altitudes of 5000, 5200 and 5400 m within the layer of increased LIDAR signal that was seen in Figure 3.3 at 14:00 UTC. Tick marks were added with a 24 hour interval.

3.8 MSIS-E-90 model

To do a Rayleigh correction of the LIDAR case study, the air density was retrieved from the MSIS-E-90 model. The **M**ass-**S**pectrometer-**I**ncoherent-**S**catter **E**xtended (MSIS-E)-90 model calculates the horizontally and vertically resolved neutral temperature and density through the thermosphere, mesosphere, stratosphere and troposphere from a multiyear average [Hedin (1987), Hedin (1991)].
Like the HYSPLIT trajectory model, the MSIS-E-90 model can be run online from a webpage [NASA (2012d)].
Present weather conditions might differ from the multiyear average. Therefore, both the MSIS-E-90 data and the radio-sonde data could differ from the actual weather situation above ALOMAR. Hence, a comparison was done between the MSIS-E-90 data and radio-sonde data (Figure 3.5). There were nearly no differences in air density between the curves from the radio-sounding with and without moisture. Both lines were on top of each other and not even distinguishable. The difference between the air density calculated from the soundings and from the MSIS-E-90 model was small, with a maximum difference of 3.47×10^{-5} $\frac{g}{cm^3}$ or 7.2 % at an altitude of 9 km.

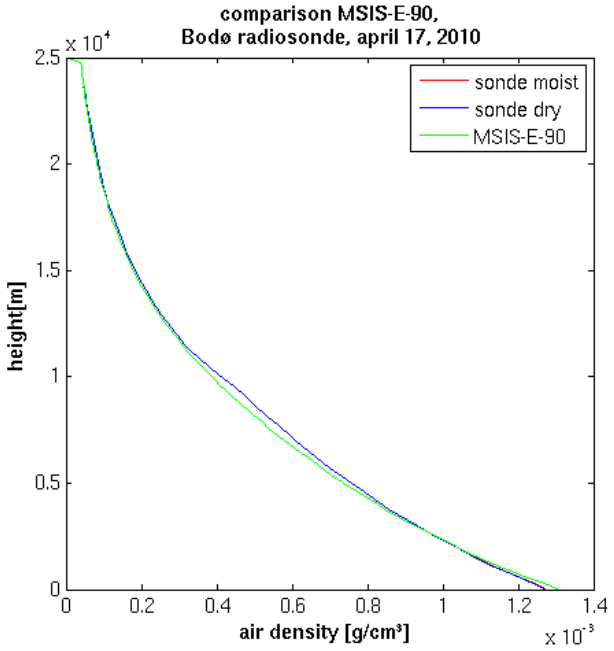

Figure 3.5: Comparison between the air density from the MSIS-E-90 model (green line), the dry air density from the Bodø radio-sounding (blue line) and the moist air density from the Bodø radio-sounding (red line), April 17, 2010. The red and the blue lines are coinciding (the moisture does have nearly no influence on the air density), making the red line impossible to spot.

3.9 FLEXPART

The FLEXPART model was used to identify the sources of potential aerosol layers in the ALOMAR LIDAR data. Together with the LIDAR data, FLEXPART provided the most important step in the identification of wildfire aerosol layers.

3.9.1 The FLEXPART model

FLEXPART is a Lagrangian type particle dispersion model. Its first version was developed by Andreas Stohl in 1998 and originally designed for the simulation of long-range and mesoscale dispersion of air pollutants from a point source (e.g. accidents in nuclear power plants) [Stohl et al. (2005)]. Today, the model is used for a variety of purposes by a number of research groups.

3.9.2 Model version and setup

For this work, the most recent available version of FLEXPART (version 8.23) was used [Stohl et al. (2011)]. After a manual identification of the vertical and temporal extent of potential aerosol layers in the LIDAR data, backward-simulations were started, releasing a total of 20000 particles. If several layers were found during the

same measurement day, simulations were done for each layer seperately and for all layers together. When the source region coincided with MODIS fire counts, another set of simulations was started in the vicinity around those layers:

- From the top of the layer to 1000 m above.
- From the bottom of the layer to 1000 m below.
- From 1000 m above the top of the layer to 2000 m above.
- From 1000 m below the bottom of the layer to 2000 m below.

The ambience simulations were done to get a good overview of the origin of the air that was surrounding the layer. The tracer particles were emitted into the backward-simulation as vertical line emissions at 69.27833° N 16.00861° E.
Gravitational settling speed was set to zero in accordance with earlier FLEXPART applications for the source specification of wildfire aerosols [Stohl et al. (2006)] and because of the low graviational settling speed of accumulation mode particles as discussed in Section 2.1. All simulations extended backwards in time for 20 days. Output was produced averaged over 43200 s (12 h). The output grid had a resolution of 0.5 degrees with upper boundaries of the vertical layers at 300, 600, 1000, 2000, 3000, 4000, 5000, 6000, 7000, 8000, 9000, 10000, 11000, 12000 and 13000 m. Since fires in middle to high latitudes were to be studied, the output grid was confined to the northern hemisphere from 34° N. The output variable was the **P**otential **E**mission **S**ensitivity (PES) [Stohl et al. (2003)]. The PES is proportional to the accumulated time spent by the passive tracer particles in a grid-box, when removal processes were ignored. An elevated PES indicates that an airmass was coined by the atmospheric conditions of the respective region (e.g. by aerosols from wildfires).

3.9.3 Input data

European **C**entre for **M**edium-Range **W**eather **F**orecasts (ECMWF) operational data with information on wind velocities in x, y and z direction and humidity were used as input. The data had a global cover and a resolution of 1°. To reach a better representation of the transport and wind shear during the first few hours after release, nested input data with a resolution of 0.25° were used in a domain 5° around ALOMAR (64° N 11° E to 74° N 21° E). The vertical resolution was 91 layers. The global data were provided by Andreas Stohl (NILU). The nested data were retrieved directly from ECMWF by Bjørg Rognerud (UiO).

3.9.4 FLEXPART data evaluation

The FLEXPART data were analysed together with MODIS fire counts. A Matlab routine for opening FLEXPART output was provided by Sabine Eckhardt (NILU), the M_Map package was used for plots.

Basic analysis for each potential aerosol layer

For every simulation, the PES was averaged over time and integrated in height as a measure of the sensitivity of the receptor (in this case the air above ALOMAR) to unit emissions in each vertical grid column. The result was divided by its total maximum, resulting in a new, dimensionless variable: the relative PES, which is similar to the PES defined by Seibert and Frank (2004).
Another variable, the relative footprint PES, was calculated by only integrating in height over the lowest levels. Since fires release a large part of their emissions into the lower troposphere, an elevated relative footprint PES above a wildfire indicated a strong connection between an aerosol layer above ALOMAR and the fires. Mostly, the lowest 3 to 5 levels were used, corresponding to altitudes between 1000 and 3000 m in accordance with Stohl et al. (2006).
The results were plotted on polar stereographic maps, covering the northern hemisphere from 35° N.
Simultaneously, MODIS CMG fire pixel counts from Terra and Aqua were averaged over 24 days (three data sets) with the last 8 days including the LIDAR measurement. The averaged fire pixel counts were then divided by the total number of MODIS pixels in each grid cell to get the relative fire cover for each cell. The relative PES and the relative footprint PES were plotted together with the relative fire cover to estimate the overlap between fires and high emission sensitivity. It was possible to repeat the above analysis only for one Terra and Aqua dataset, reducing the averaging time to only 8 days.
Large fires in the vicinity of high relative footprint PES could have contributed significantly to a plume. Therefore, a relative **P**otential **S**ource **C**ontribution (PSC) similar to the definition in Stohl et al. (2007) was calculated. The PSC is a folding (multiplication) of emission inventories (in this case the relative fire cover or the fire radiative power) with the relative PES. Very high fire emissions in connection with only a slightly elevated relative PES can be indicative of a stronger contribution to an aerosol layer than a high relative PES in connection with only weak fires. The relative PSC would in this case be higher for the stronger fires. From now on, the word relative is omitted, PES and PSC always refer to relative PES and PSC.

Further analysis of fire cases

So far, the comparison of high PES and fire activity was done only for time-averaged fire data over 24 or 8 days. This could have led to a false positive identification of forest fire aerosols. Thus, if a correlation between fire activity and high PES had been established, the PES was compared to MODIS single fire counts. For this, the footprint residence time was integrated only over 12 or 24 hours and plotted together with the corresponding MODIS daily single fire counts. If high PES coincided with fires, both spatially and temporally, the original aerosol layer above ALOMAR was finally identified as forest fire aerosols. The same was repeated for the PSC between the time-resolved PES and the time-averaged relative fire cover or fire radiative power. However, the MODIS daily single fire counts were only used as a control,

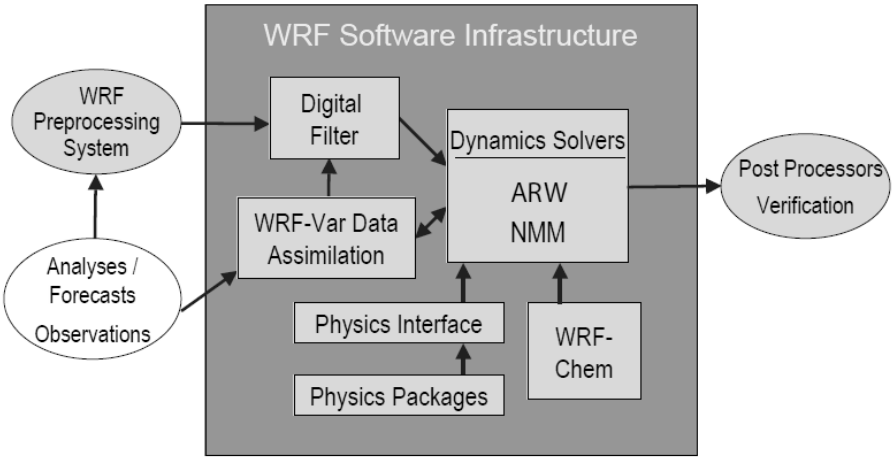

Figure 3.6: Schematic of the WRF components, including WRF-Chem. For this work, the ARW WRF-core has been used. Figure from Skamarock et al. (2008).

wether fire detections coincided spatially and temporally with the build-up of high PES. They were not used for the calculation of a PSC.

3.10 WRF and WRF-Chem

WRF-Chem was used for the analysis of long-range transport and the self-lifting effect. It consists of an Eulerian model (WRF) with a fully coupled online chemistry extension, WRF-Chem (the name is used for both, the extension and the full model). The full coupling between chemistry and transport allowed for the simulation of self-lifting.

3.10.1 WRF

The **W**eather **R**esearch and **F**orecasting (WRF) model and the chemistry extension WRF-Chem are developed and maintained separately as a combined effort between a number of institutions. Both models were designed as a community model for a wide range of applications from teaching and research to operational use. Together, WRF and WRF-Chem result in a fully coupled, fully compressible, Euler non-hydrostatic model with mass and scalar conservation [Grell et al. (2005)]. Figure 3.6 shows the WRF system components, including WRF-Chem.
The input data were pre-processed within the **W**RF **P**reprocessing **S**ystem (WPS). A bug has been found in the routine for reading the input datasets. A description of the bug and a bug-fix manual is given in Appendix C.3.

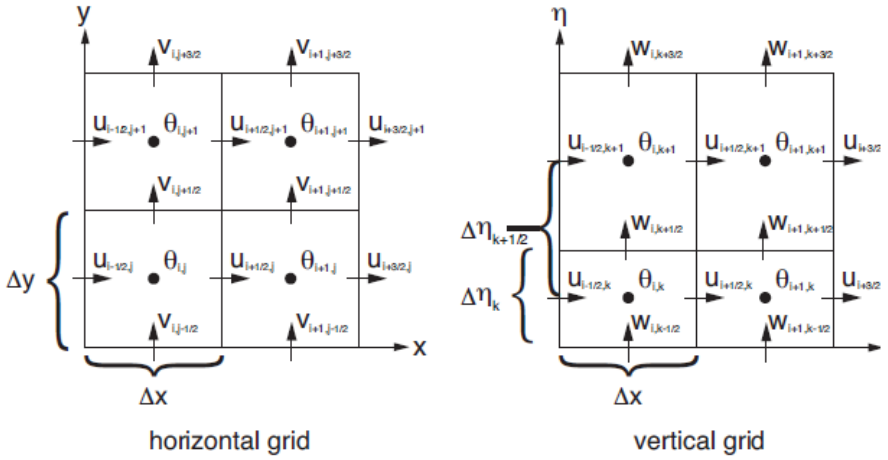

Figure 3.7: Illustration of the staggering in the Arakawa C-Grid. Points at the edges of the squares are referred to as staggered grid-points (full-levels in the vertical direction). Points in the centres of the squares are referred to as non-staggered grid-points (half-levels in the vertical direction). Chemical variables are given at non-staggered grid-points. Figure from Skamarock et al. (2008).

ARW Dynamic Solver

There are two dynamic solvers available in WRF: the non-hydrostatic **A**dvanced **R**esearch **W**RF (ARW) solver, which has been used for this work and the **N**on-hydrostatic **M**esoscale **M**odel (NMM) solver.
The ARW solver uses a time-split integration with a 2nd or 3rd order Runge-Kutta scheme, allowing for a shorter time-step for acoustic and gravity wave modes and a longer time-step for the meteorological modes. This allows for a relatively long time-step with high computational efficiency, while conserving the numerical stability. The minimum prognostic variables are the u, v and w velocity components, the perturbation potential temperature, the perturbation geopotential height and the perturbation surface pressure of dry air.
The grid is a Cartesian Arakawa C-Grid. The earth's spherical shape is taken into account by defining a map scale factor as a measure of the grid distortion

$$(m_x,\ m_y) = \frac{(\Delta x, \Delta y)}{\text{distance on earth}}. \tag{3.11}$$

Figure 3.7 illustrates the staggering of the different variables in the Arakawa C-Grid.
The vertical coordinate is a terrain-following, dry hydrostatic-pressure coordinate

$$\eta = \frac{p_h - p_{ht}}{\mu(x,y)}, \tag{3.12}$$

with

$$\mu(x,y) = p_{hs} - p_{ht}, \tag{3.13}$$

where p_h, p_{hs} and p_{ht} denote the hydrostatic component of the pressure at the layer, the surface and the top, respectively. The variable $\mu(x,y)$ denotes the mass per unit area of the dry air column at the horizontal point (x,y). A schematic of the η coordinate over topography is shown in Figure 3.8.

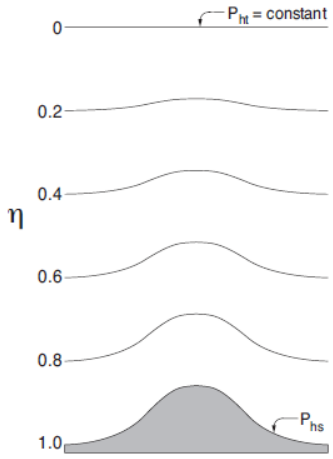

Figure 2.1: ARW η coordinate.

Figure 3.8: Schematic of the ARW η coordinate over topography. Level-spacing is smaller over topography. The uppermost level is flat in comparison to the mean sea-level. Figure from Skamarock et al. (2008).

3.10.2 WRF-Chem

WRF-Chem is the chemistry extension to the WRF model. The chemistry is calculated online, i.e. fully coupled with the transport scheme, with feedback in both directions. WRF-Chem is fully consistent with WRF, as it shares the same mass and scalar preserving transport scheme, the same physics schemes for subgrid-scale transport and the same time-step. The mass and scalar conservation are described in conservation equations of the form [Grell et al. (2005)]

$$\mu_t + \nabla \cdot (\vec{V}\mu) = 0 \tag{3.14}$$

$$(\mu\phi)_t + \nabla \cdot (\vec{V}\mu\phi) = 0, \tag{3.15}$$

with ϕ, a scalar mass mixing ratio, $\vec{V}$ the wind velocity vector and μ as defined above. There are a number of different choices that can be made for the chemistry scheme, of which RADM2/MADE/SORGAM(aq) was chosen for this work. A description of the scheme is given in Appendix B. RADM2/MADE/SORGAM was chosen since it provided a good balance between computational efficiency and accuracy and because some experience existed in this department with simulations of wildfire releases in this scheme. The extended RADM2/MADE/SORGAM(aq) was chosen, because it simulated the indirect aerosol effect that might have had some influence on the scavenging efficiency and thus, on the transport efficiency.

Plume rise

Wildfire emissions were released into the simulation domain with the help of the routines in module_plumerise1.F. The vertical emission profiles are calculated in a seperate 1-D routine [Freitas et al. (2007)] and released pre-defined into the atmospheric columns. The fires themselves and their heat release are not simulated

or even considered in WRF-Chem [Grell (2012)]. Thus, the emissions are not released at the ground with subsequent simulation of the rising plumes but instead, the emission altitudes are calculated a priori and the aerosols simply appear in those altitudes. In nature, the heat release from the fires would influence the meteorology of the region. This is not simulated. Since the heat release from the fires is not simulated in WRF-Chem, the extinction of solar radiation at the emission site leads to a cooling of the ground at the fires and a stabilisation of the atmosphere directly above them. In nature, this would at least partially be counteracted by the heat release from the fires.

Dry- and wet-deposition rates for BC aerosols

The dry- and wet-deposition rates for chemical species were not explicitly reported in WRF-Chem output. New routines were added to calculate the domain integrated BC dry-deposition and grid-resolved and subgrid wet-scavenging rates. An excerpt of the file chem_driver.F is given in Appendix C.2.
For some of the simulations, wet-scavenging was suppressed by setting the namelist variable wetscav_onoff to 0. This, however, only suppressed grid-resolved wet-scavenging. Subgrid-scale wet-scavenging could not be suppressed in this version of WRF-Chem.

Aerosol optical properties

The calculation of aerosol optical properties was done in two steps: First, the refractive indices were averaged. Afterwards, the aerosol optical thickness, extinction coefficient, backscatter coefficient, asymmetry parameter and single-scattering albedo were calculated, using Mie theory for the wavelengths (300, 400, 600 and 1000 nm). The routines are independent of the choices made on the chemistry scheme.
There are three different routines available for the optical averaging of the refractive indices in WRF-Chem. For all three routines, the size distribution is first spread into eight equally sized bins. All three routines assume solely internal mixing. Figure 3.9 shows an illustration of the differences in the optical averaging. Only the first routine is finished and fully tested and therefore recommended for use. For each bin, the refractive indices of all aerosol species are averaged by volume, neglecting any particular substructure.

BC absorption

To extract the effect of BC radiation absorption, it was necessary to do simulations with and without BC radiation absorption. It was not possible to disable BC radiation absortion in the input namelist. Thus, the imaginary part of the refractive index of BC was changed in the source code from the original WRF-Chem value

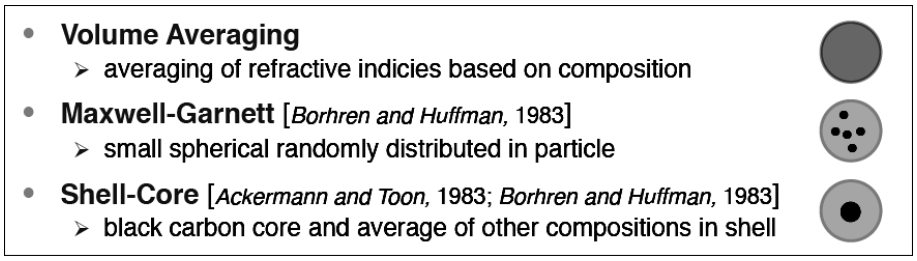

Figure 3.9: Illustration of the three different optical averaging routines in WRF-Chem. Only the first routine is fully tested. The other two routines, though possibly more exact, are computationally more expensive and not yet recommended for use. Figure from Fast et al. (2010).

0.71 to 0 for the non-absorptive cases. All other parameters were left unchanged to extract only differences that were caused by absorption of radiation from BC.

3.10.3 Input data sets

Meteorological input data

ECMWF operational data with a horizontal resolution of 0.5° were retrieved for the domain 29° N < latitude < 89° N, 156° W < longitude < 34° E from March 28, 2010 until April 18, 2010 by Bjørg Rognerud (UiO). The data had a vertical resolution of 26 atmosphere levels from 1 to 1000 hPa and 4 soil levels.

FINN tool

The **F**ire **IN**ventory from **N**CAR (FINN) (**N**ational **C**enter for **A**tmospheric **R**esearch) tool [Wiedinmyer et al. (2010)] was used for producing the wildfire releases. It provides daily wildfire emissions with a horizontal resolution of 1 km. The fire emissions are based on fire detections as described in Section 3.4. Double fire counting is prevented in a circumference of 1 km around a detected fire. No more fire can be detected in this area during the same day. Fire emissions are estimated using

$$E_i = A(x,t) \cdot B(x) \cdot FB \cdot ef_i, \tag{3.16}$$

with i the emitted species, E_i the mass emitted of i, A the area burning during time t and at location x, $B(x)$ the biomass loading at x, FB the fraction of biomass that is burned in the fire, and ef_i the emission factor for species i.
The part of the FINN tool mapping the fire raw-data to the WRF-Chem domain was modified so that fire emissions could be constrained in time and space. The changes are described in Appendix C.1. A mapping list was necessary from the fire raw-data to the correct species of the chemistry scheme in WRF-Chem. A mapping list from NCAR was used, in which a bug was found during the work. A description of the problem and a bug-fix are given in Appendix C.4. Another bug was found in

Physics Option	Scheme
Micro Particle	Lin et al.
SW Radiation	Goddard SW
LW radiation	RRTM
Planetary Boundary Layer	YSU
Cumulus Parameterisation	Grell-Devenyi

Table 3.2: WRF-Chem physics parameterisations. Micro particle and SW radiation parameterisations were prescribed by the chemistry scheme. The remaining parameterisations were chosen according to Sessions et al. (2010).

the WRF-Chem module_aerosols_sorgam.F for processing the fire emission input data sets. A description of the problem and a bug-fix are given in Appendix C.5. FINN emissions are based on twice daily wildfire detections that are combined together to one daily fire detection with highest possible cover. To account for the temporal variation of wildfire releases, a diurnal cycle is assumed, with maximum releases during the day and nearly no releases during the night. That assumption was found to be more correct for fires in low latitude regions because of the strong influence of solar heating of the ground [Eva and Lambin (1998)]. In high latitudes, the effects of increasing or decreasing winds might be dominating, causing a possible source of uncertainties in transport through inexact emission times.

3.10.4 Simulations

A number of WRF-Chem simulations was done to analyse the transport and the self-lifting of wildfire aerosols. Only the basic setup is given here, details are given in the Sections 4.4 and 4.6. A short description of the model control is given in Appendix B.2.

Model setup

The domain was a Lambert-conformal projection with a horizontal resolution of 30 km $\times$ 30 km at the true point and a size of 260 $\times$ 193 horizontal grid points. The map scale factor was between 1 and 1.23; relevant aerosol transport did not include regions with a map scale factor over 1.1. The vertical resolution in the atmosphere was 35 layers between ground pressure and 0.5 hPa. The model timestep was 180 s. The runtime was from April 04, 2010 until April 18, 2010. Table 3.2 gives an overview over the relevant physics parameterisations. Nudging (Newtonian relaxation) of the horizontal wind velocities and the water vapour mixing ratio were used in order to force the simulations towards observations. This was necessary, because initial simulations without nudging showed entirely different conditions after a few simulation days, when only the domain size was changed by a few degrees, illustrating the instability of the simulations for only minor changes. The nudging coefficients for the horizontal velocities and the water vapour mixing ratio were set

to $3.2 \cdot 10^{-4}\ \frac{1}{s}$, according to a recommendation from Øivind Hodnebrog (Cicero). The nudging coefficient of the temperature was set to $1 \cdot 10^{-6}$. This was done, because it was aimed to simulate temperature changes. A strong nudging of the temperature would have suppressed those changes.

3.10.5 Data evaluation

The Arakawa C-Grid is a staggered grid. The geopotential height is only given at downward staggered positions (full levels), the chemical variables are given at non-staggered positions (half levels). That made it necessary to calculate the half-level geopotential height. A linear interpolation of the geopotential height was done using the pressure at the full-

$$p_{h,s} = \eta_s \cdot \mu + p_{ht} \tag{3.17}$$

and half-levels

$$p_{h,u} = \eta_u \cdot \mu + p_{ht} \tag{3.18}$$

that were calculated from Equation (3.10.1) according to a recommendation from Bjørn-Egil Nygaard (Norwegian Meteorological Insitute).
BC was used as a plume tracer, since it is the most relevant species for self-lifting. A comparison to other wildfire related aerosol species showed overlapping positions. Aerosol concentrations were given in units of $\frac{\mu g}{kg(\text{dry air})}$. For the data evaluation, the concentrations were recalculated to have the unit $\frac{\mu g}{m^3}$. The grid-box size was varying horizontally (map scale factor) and vertically (η-levels). Thus, an array was calculated with the volume of each grid-box.
To make the data comparable to sun-photometer and MODIS measurements, the column-integrated Ångstrøm exponent between 400 and 600 nm was calculated. From that, the column integrated AOD at 500 nm (sun-photometer) and 550 nm (MODIS) could be calculated.
For assessing the overall effect of radiatively induced self-lifting, the **M**ass **W**eighted **M**ean **A**ltitude (MWMA) of BC was calculated. This was done by a multiplication of the total BC concentration in a grid-box with its volume. The resulting grid-box BC mass was then multiplied with its altitude. The result was summed over the entire domain and finally divided by the domain integrated BC mass. Variable lower AOD thresholds at 600 nm was introduced, under which the column integrated BC concentrations were set to zero and therewith excluded from the MWMA calculations. That made it possible to analyse the self-lifting dependent on the plumes' AOD and therewith dependent on the plume strength.
Including the total atmospheric column in the calculation of the MWMA introduced an underestimation from the non-lifted background. This underestimation was however small and decreased with the AOD threshold.
Probability **D**istribution **F**unctions (PDFs) for the BC aerosol concentrations were calculated with the Matlab ksdensity function, calculating a kernel smoothed PDF. The BC concentrations spanned a wide range from $10^{-16}\ \frac{\mu g}{m^3}$ to $10^{4}\ \frac{\mu g}{m^3}$. Thus, the logarithm of the concentrations was used as a basis for the PDFs.

Chapter 4

Results and Discussion

The results from the identification of wildfire aerosol layers are presented and discussed in the first section of this chapter. In the second section, the long-range transport is analysed for the most suitable case. For the same case, radiatively induced self-lifting is studied in the last section. Altitudes are given in **A**bove **M**ean **S**ea-**L**evel (AMSL).

4.1 Identification of wildfire aerosol layers

For the present study, LIDAR data from the ALOMAR troposphere LIDAR from 2010 and 2011 were used. Measurements were taken during a total of 120 days, of which 65 fell into 2010 and 57 into 2011. Little biomass burning and no self-lifting was expected during the period from October to March. Thus, only data from April to September were used. A total of 33 cases in 2010 and 39 in 2011 were analysed. In 2010, nine datasets were dismissed because of obvious electrical noise in the raw-data, none in 2011. From the remaining cases, two were dismissed in 2011 and one in 2010, since the measurements lasted only a few minutes and could therefore not be used for analysis. Another case in 2010 was dismissed, since the signal strength was strongly increasing with height.
The remaining datasets were separated into days only showing clouds, clean air days and days showing potential aerosol layers. As already explained in Section 3.1.5, the analysis of the cases in 2010 was somewhat different from the cases in 2011.
In 2011, layers were sorted out using the low PDR of aged wildfire aerosols that are usually spherical in shape. A PDR larger than 15 % was not expected for wildfire aerosols. However, as explained in Section 3.1.6, it would have been necessary to get pre-processed data for every data set in order to calculate the PDR. Therefore, the VDR was used with the same threshold of 15%. Replacing the PDR by the VDR could only be used to sort out strong signals, since the VDR for weak signals was too strongly influenced by the very low depolarisation of the Rayleigh signal (Section 2.5.1). The results were double-checked with SYNOP reports and radio-sonde measurements.

In 2010, no separate calibration procedure was available. A calibration based on the Rayleigh signal was not possible on a regular basis, since that would have made it necessary to get pre-processed data for every data set. Therefore, the cloud identification was done based on the signal strength, SYNOP reports and radio-soundings. Very strong signals were not expected to be caused by wildfire aerosol layers, since ALOMAR was only affected by long-range transport of plumes that were likely to be diluted. If SYNOP reports additionally showed cloud contamination, the layer was sorted out. Attention was thereby also given to the substructure of the LIDAR signal. For example cirrus fibratus clouds should show a LIDAR signal with a fibre like or at least fractured substructure. Radio-soundings from Bodø airport station mostly confirmed the conclusions by the existence of high relative humidity. Also with this method, it was not possible to sort out weak signals, since layers causing weak signals were not expected to be reported in the SYNOP reports.
The remaining nine cases in 2010 and 20 cases in 2011 were analysed with FLEXPART simulations. Of those, the PES (Section 3.9.2) from six layers in 2010 and five in 2011 coincided with the MODIS CMG fire pixel counts. The footprint PES from six layers in 2010 and four in 2011 coincided well with the fire pixel counts. Of the ones showing a good agreement between FLEXPART source specifications and fire activity, six cases had their origin in North America, three in Russia and one in Georgia.
The LIDAR signal was very weak for most of the cases showing an overlap between MODIS CMG fire pixel counts and FLEXPART simulations. Only two cases were found to show a clear LIDAR signal in all analysed channels and a good overlap between the simulated source region and MODIS detected wildfires. The source regions of both cases were located in North America. One case was detected on April 17, 2010 and the other one on June 24, 2010 (the layer that was used as an example throughout Chapter 3). The case from April 17, 2010 showed an aerosol layer with a stronger LIDAR signal and the transport simulations showed an overlap with higher fire activity than for the layer from April 24, 2010. The LIDAR signal was the strongest of all aerosol layers in 2010 and 2011. Therefore, the layer from April 17, 2010 was chosen for an in-depth analysis, including the calculation of the PDR, extended analysis of the FLEXPART results and WRF-Chem simulations.

4.2 In-depth analysis April 17, 2010

4.2.1 LIDAR results

Figure 4.1 shows the time-resolved and the time-averaged 1064 nm profiles from April 17, 2010. The data set was recorded over a time span from 15:42 - 16:50 UTC. The time-resolved plot shows an enhanced signal at an altitude around 6300 m throughout the entire measurement period, increasing in strength over the first few minutes and then staying nearly constant after that. Strong backscatter signals were found during short periods at altitudes around 1000 and 4000 m. Those were concluded to be clouds. A decrease in the background signal was observed at an

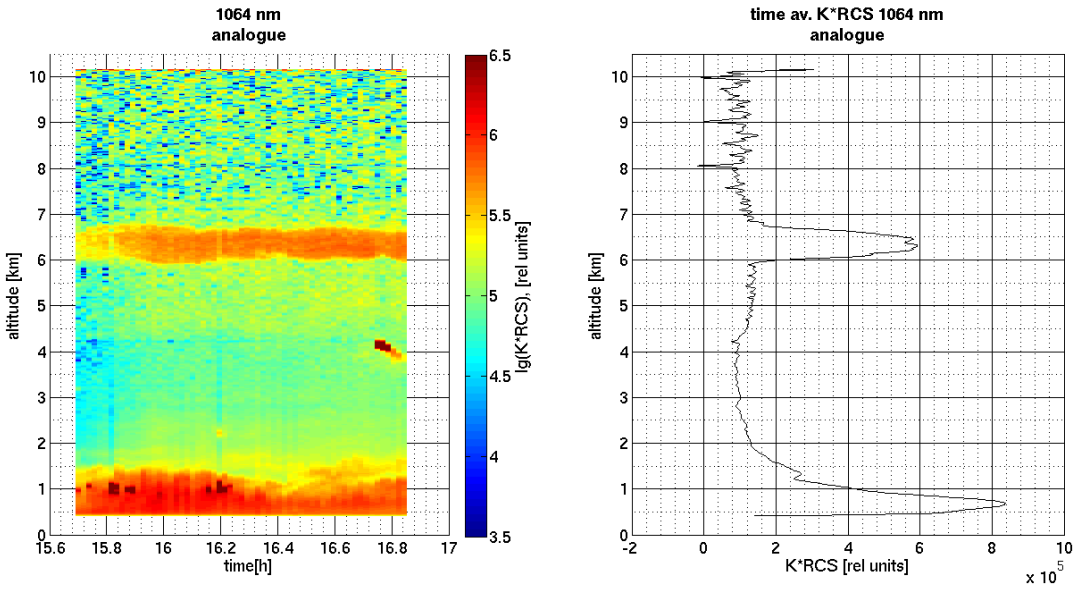

Figure 4.1: Left panel: time-resolved profile of the logarithmic RCS from April 17, 2010. The signal was cut off from altitudes above 10 km. Right panel: time-averaged 1064 nm RCS signal profile. Averaging was done from 16:18 - 16:42 UTC. A potential aerosol layer is visible between 6000 and 6700 m. The top of the PBL is visible around 1500 m. The signal in the PBL is higher than what would be expected for a clean air day.

altitude around 1000 m, indicating the top of the PBL.
Averaging was done over the data from 16:18 - 16:42 UTC in order to avoid confusion from the strong signals around 1000 and 4000 m. In addition to the main signal at an altitude around 6300 m, a slightly increased signal was seen directly below that in the time-resolved profiles and in the time-averaged 1064 nm profile, extending down to an altitude around 4300 m. Figures 4.2 and 4.3 show the 532 nm p- and s-polarized time-resolved profiles for the analogue and photon counting detection mode (for an explanation of the two detection modes, see Appendix A.2). The strong signal around 6300 m and the strong signals at lower altitudes were also detected in both 532 nm channels. The decrease in signal strength at the top of the PBL was less prominent because of the dominant Rayleigh profile (Rayleigh scattering is more dominant for smaller wavelengths because of the $\frac{1}{\lambda^4}$ dependency, in comparison to the $\frac{1}{\lambda^2}$ dependency for Mie scattering).

Figure 4.4 shows the glued and time-averaged data, including the Rayleigh extinction correction and the Rayleigh fit. The averaging time was from 15:42 - 16:00 UTC and from 16:00 - 16:50 UTC. Both datasets were combined so that an average over the full temporal extent of the measurement was reached. The Rayleigh fit was done at an altitude between 10 and 12 km, well within the stratosphere. The calibration factor was 0.2125.

Figure 4.5 shows the VDR and the PDR. The layer with increased signal strength was depolarizing, with a maximum PDR around 2.1%. The VDR was lower because of the influence of the Rayleigh signal. In addition, the uncalibrated VDR and PDR profiles are given in Figure 4.6. The maximum PDR was 10%.

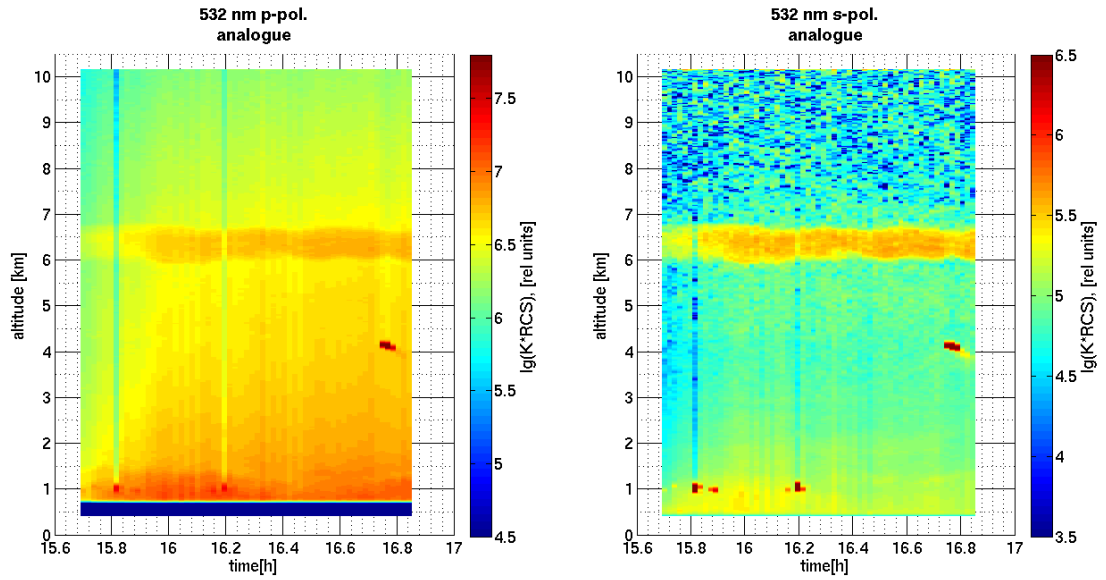

Figure 4.2: Left panel: time-resolved 532 nm analogue p- polarized RCS profile from April 17, 2010. Right panel: analogue s-polarised profile, x-axis: hour of the day, y-axis: altitude above sea-level. The same layer as in Figure 4.1 is visible. The bright vertical lines around 15.8 and 16.2 on the x-axis are caused by the very high extinction of the low level clouds around 1 km altitude.

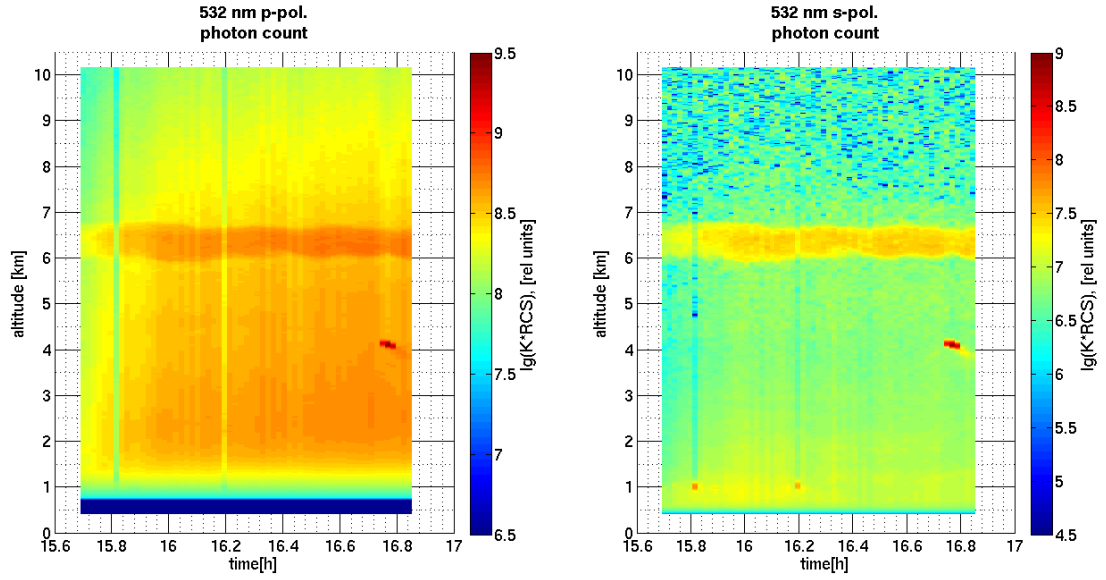

Figure 4.3: Same as Figure 4.2 for the photon counting channels (for an explanation of the differences between analogue and photo-counting, see Appendix A.2).

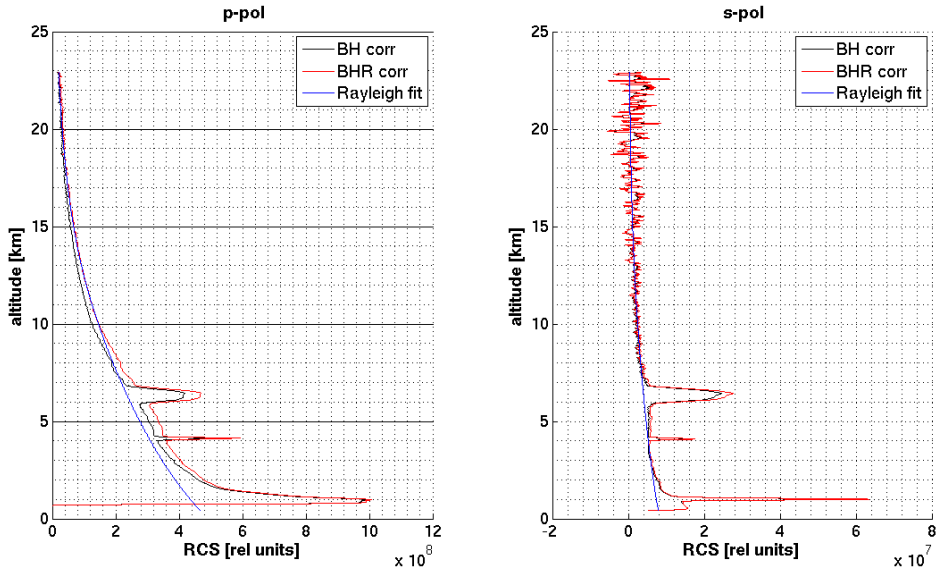

Figure 4.4: Left panel: time-averaged, glued (analogue and photon-counting) 532 nm p-polarised profile from April 17, 2010. Right panel: s-polarised profile. Averaging was done over the full temporal extend of the measurement. The black line indicates the RCS, the red line is the Rayleigh corrected RCS and the blue line shows the Rayleigh fit.

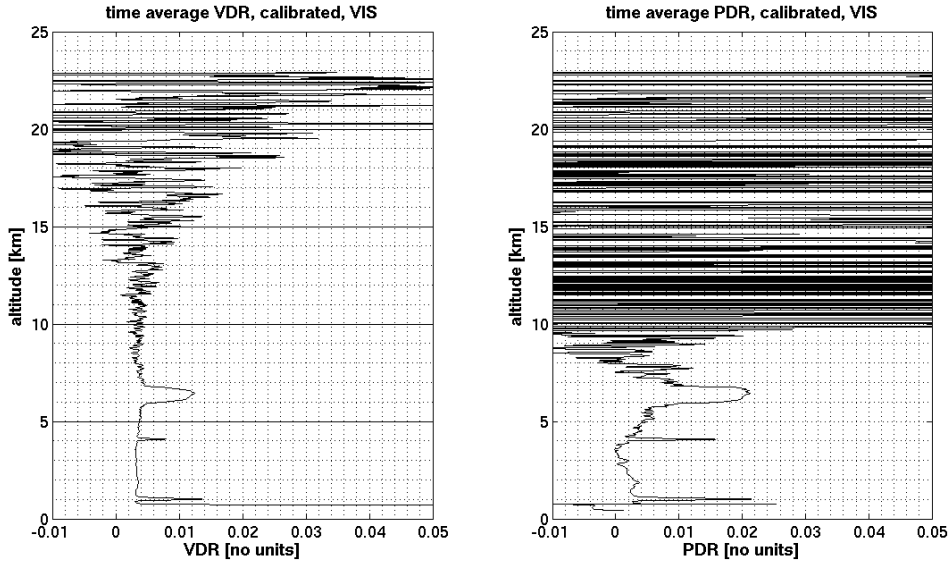

Figure 4.5: Left panel: calibrated, time-averaged volume depolarisation ratio. Right panel: calibrated, time-averaged particle depolarisation ratio. The calibration factor was 0.2125. Averaging was done over the full temporal extend of the measurement.

A low PDR of 2.1% indicated almost spherical particles. Aged biomass burning particles are usually assumed to be mostly spherical. Murayama et al. (2004) found PDR values for biomass burning aerosols with a maximum value around 6-8%. To the knowledge of the author, so far no systematic investigation has been done on

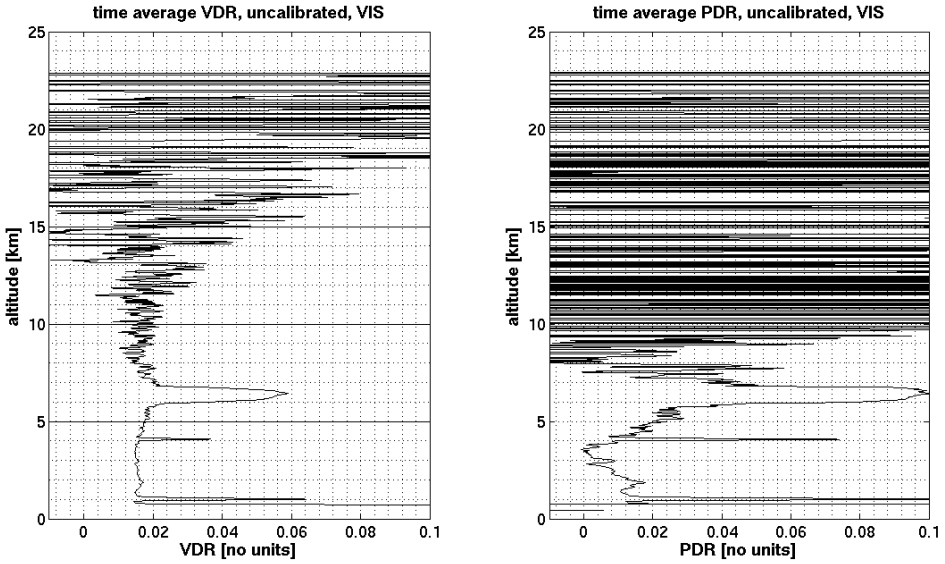

Figure 4.6: Left panel: uncalibrated, time-averaged volume depolarisation ratio. Right panel: uncalibrated, time-averaged particle depolarisation ratio. The calibration factor was 0.2125. Averaging was done over the full temporal extend of the measurement.

the PDR of aged wildfire aerosol particles. Many factors can change the shape of a particle during transport (e.g. activation as **C**loud **C**ondensation **N**uclei (CCN) and coagulation). However, all wildfire aerosol plumes have a low PDR in common. From the separate calibration procedure in 2011, the calibration factor for the photon counting channels was often found between 0.8 and 0.9. The calibration factor for this case seemed very low in comparison (0.2125). Some of the difference could have been caused by aerosols in the stratosphere as explained in Appendix A.4. However, changes were made at the LIDAR system in 2010, making a direct comparison between the calibration factors difficult. Even without any calibration, the maximum PDR value was 0.1, still pointing towards relatively spherical particles.
The weak signal directly below the potential aerosol layer was possibly part of the same layer. Any conclusions on the weak signal based on the PDR would have been biased too much by the simplifications that were made for the partial inversion, most of all from neglecting aerosol extinction within the aerosol layer.
An inconsistency was found in the short and strong signal towards the end of the measurement at an altitude around 4000 m. The signal strength in the time-averaged profiles was high, even though the layer only existed during a small fraction of the measurement time (less than 10 min). A wildfire aerosol layer above ALOMAR this dense can be ruled out, pointing towards a cloud. Radio-soundings suggested a temperature around -30° C, indicating an ice cloud. The PDR of the layer was too low for irregular ice crystals. However, horizontally aligned ice plates, frozen cloud droplets or super cooled water might have led to low PDR values. An in-depth analysis was not done since the signal lasted only for a very short time span and the analysis of clouds was not part of this study.

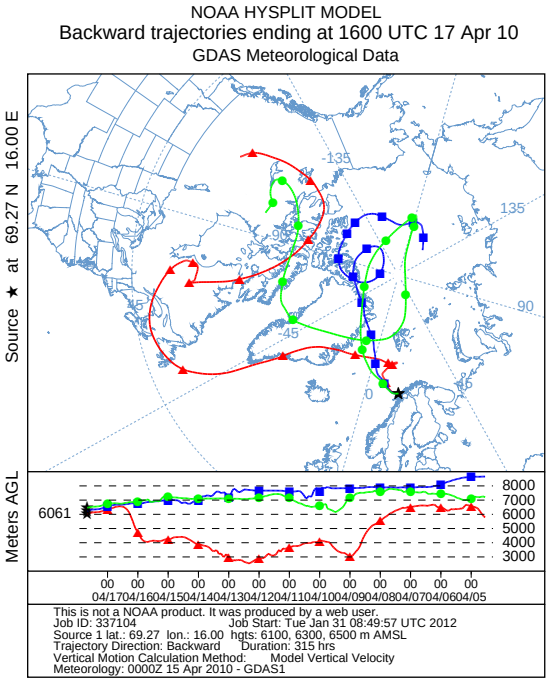

Figure 4.7: HYSPLIT backward-trajectory for April 17, 2010. Backwards-trajectories were started at 6100, 6300 and 6500 m within the layer of increased LIDAR signal at 16:00 UTC. Tick marks were included with a 24 hour interval.

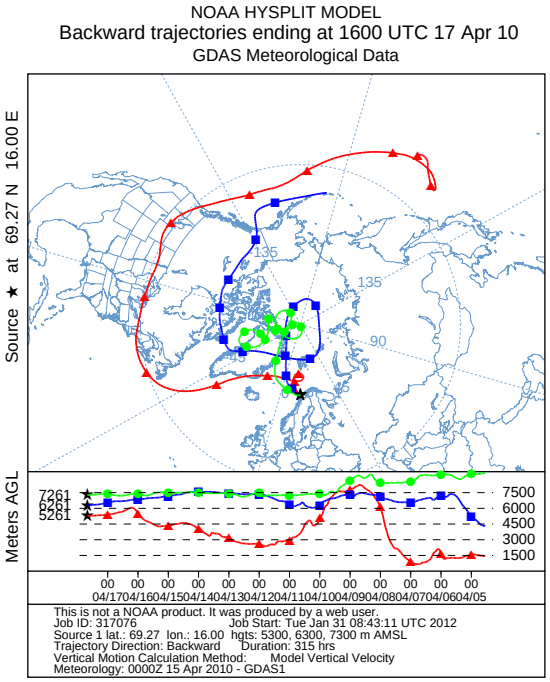

Figure 4.8: HYSPLIT backward-trajectory for April 17, 2010. Backwards-trajectories were started at 5300, 6300 and 7300 m below, within and above the layer of increased LIDAR signal at 16:00 UTC. Tick marks were included with a 24 hour interval.

4.2.2 HYSPLIT results

Figure 4.7 shows the results from a HYSPLIT simulation with 3 backward-trajectories, starting at altitudes of 6100, 6300 and 6500 m within the potential aerosol layer at 16:00 UTC. The trajectory from the lowest layer (red) grazed southern Greenland and originated from North America. The trajectories from the uppermost two layers grazed northern Greenland and originated from the Arctic. The backward-trajectory from the middle layer (blue) originated from the Arctic, whereas the backward-trajectory from the uppermost layer (green) originated from North America. The results from the simulation with trajectories starting at altitudes of 5300, 6300 and 7300 m, representing trajectories from below, within and above the potential aerosol layer are shown in Figure 4.8. Again, the trajectory starting below 6300 m originated from North America, whereas the trajectories starting at and above 6300 m originated from the Arctic.

From Figure 4.7, it appears that a shear in wind directions existed between 6100 and 6300 m in the meteorological input files, with air parcels below the layer originating from North America and air parcels above it from the Arctic. This assumption was confirmed by Figure 4.8.

From a comparison of those results to the LIDAR data it seemed that in HYSPLIT, the wind shear was placed too low. An aerosol layer from the Arctic was ruled out.

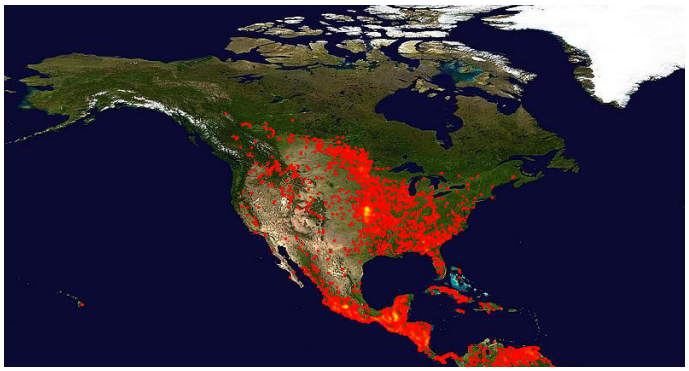

Figure 4.9: MODIS RRI quick plot from April 11, 2010 - April 20, 2010. Zoom over North America. Fires are indicated by tick-marks. Red colour indicates middle to low fire activity, yellow colour indicates high fire activity.

Assuming that the increased signal below the layer was caused by aerosols of the same origin, it could be concluded that the wind shear was placed a few hundred meters too low. No other source region for aerosols was found, except for North America. The remaining air came from clean air arctic regions.
In both Hysplit runs, one trajectory was started at an altitude of 6300 m. Those simulations should have given the exact same results, since identical initial conditions were used. However, the two runs gave different results. It is not known what caused those differences. When the same run with the same trajectories was started twice, the results were the same. One possible reason for the difference between the runs might have been rounding errors. The wind shear at the starting location of the trajectories might have enhanced whatever caused those differences. It is therefore important to keep in mind the uncertainties that are connected to single trajectory calculations. As already mentioned in Section 2.6, a Lagrangian particle dispersion model like FLEXPART does not show such problems, since a bulk of particles is released in each single run, leading to a PES that corresponds to a probability estimation of the source region, instead of the fully deterministic approach that is inherent in single particle trajectories.

4.2.3 MODIS RRI quick plot

The RRI quick plot is shown in Figure 4.9. The two trajectories from 6500 m and one of the trajectories from 6300 m originated from the Canadian and the U.S. Arctic. No fire activity was detected there. The 6100 m trajectory passed the Quebec region in a low altitude. Little to no fire activity was detected there neither. However, uncertainties were mentioned before for runs that started at exactly the same altitude. In addition, the wind shear might have been placed at a too low altitude. Looking therefore at the trajectory that started at an altitude of 5300 m, the source region was around the Great Lakes, where high fire activity was found.

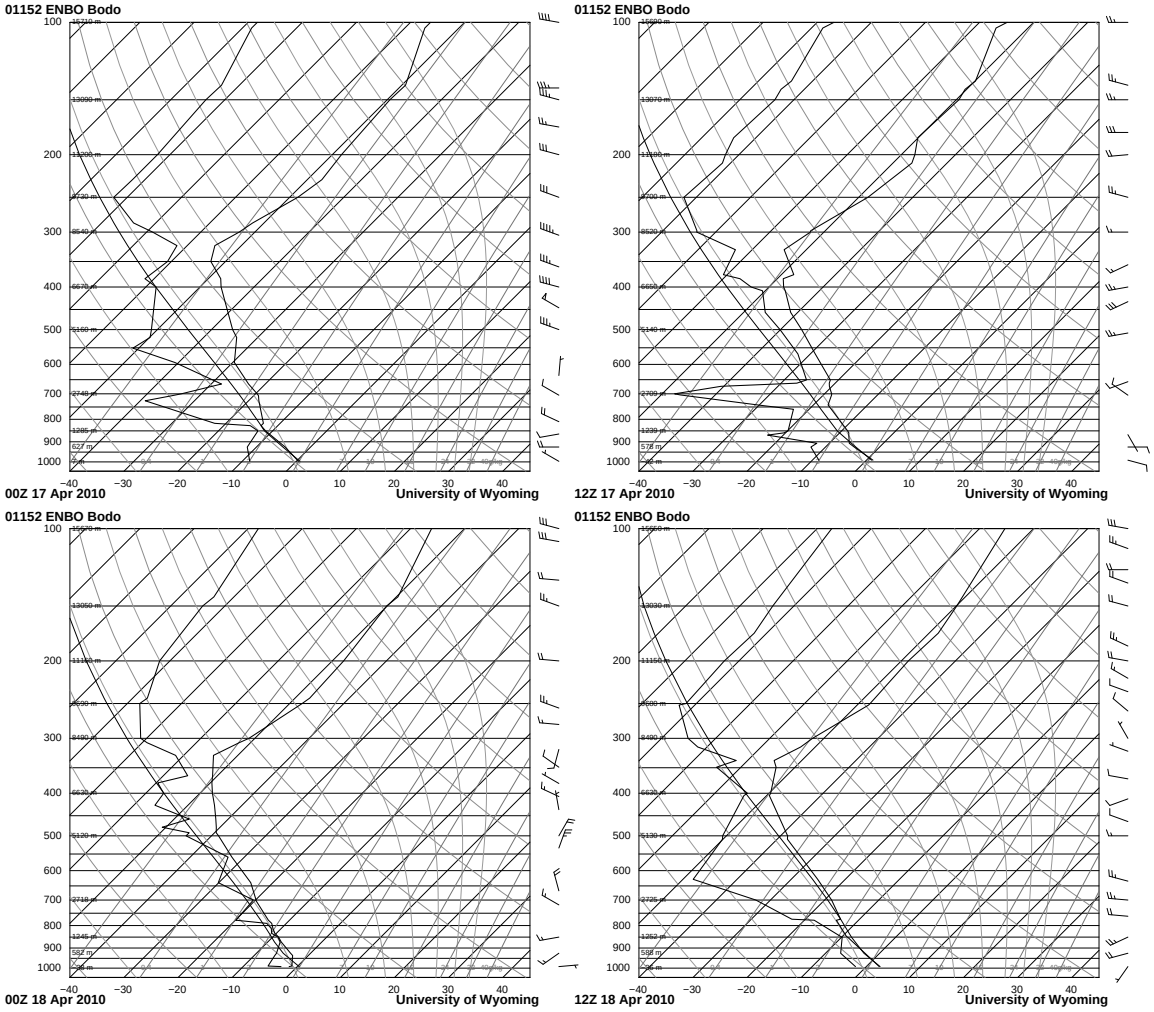

Figure 4.10: Radio-soundings from Bodø airport radio station. Plots are given for the 4 consecutive soundings from April 17, 2010, 00:00 UTC - April 18, 2010, 12:00 UTC, circumscribing the LIDAR measurement. No convergence was seen between the dew point and the temperature at altitudes around 6300 m.

4.2.4 Radio and SYNOP results

Figure 4.10 shows the radio-soundings from Bodø airport radio-sonde station. The four measurement sets from April 17, 2010, 00:00 UTC to April 18, 2010, 12:00 UTC were used. None of the measurements showed the necessary condition for clouds of converging temperature and dew-point temperature between 400 and 500 hPa (corresponding to an altitude between 5160 and 6670 m).

The SYNOP observations from April 17, 2010, 16:00 and 17:00 UTC were

SN 17/04/2010 16:00->
AAXX 17161 01010 41487 **2**2107 10005 21047 39909 49925 58006 70100 **82960**=
SN 17/04/2010 17:00->
AAXX 17171 01010 41487 **2**1907 11010 21046 39904 49920 57013 71500 **82960**=.

The cloud part (22107 and 82960) displayed relatively clear sky with total cloud cover of two oktas. Low-level clouds (cumulonimbus clouds with anvil) covered two oktas of the lower troposphere. Mid-level clouds (alto-cumulus cumulogenitus) covered an unknown part of the troposphere but less than two oktas and coinciding with the low-level clouds. No high-level clouds were observed.
The mid-level cloud type was in accordance with the very short and strong signal at an altitude around 4000 m with cumulus like structure and therefore small patches of strong clouds.

4.2.5 FLEXPART source specification results

Indications were found that the layer from April 17, 2010 could have originated from wildfires. Thus, a detailed analysis was done using FLEXPART simulations, together with MODIS wildfire data. First, the simulation results were time-averaged over the full extend of the simulations (20 days) to get an impression of the transport pathways and the overall source regions.

Time-averaged analysis

The result from the backward-simulation of the potential aerosol layer is shown in Figure 4.11. Three main transport directions were found: over the Arctic Ocean, towards North America, rotating over Quebec and towards North America, travelling over the Great Lakes and getting mostly dispersed afterwards. It was possible to recognise the location of the split between the transport directions towards the Arctic and towards North America over the east coast of Greenland.
The result of the backward-simulation from below the potential aerosol layer is shown in Figure 4.12. Only the two transport directions towards North America remained. The values for the PES were higher than for the potential aerosol layer itself. The PES from a layer covering the 1000 m above the potential aerosol layer showed transport only over the Arctic Ocean (not shown).
A comparison of the main plume parts in Figure 4.11 to the HYSPLIT trajectories showed resemblance of the parts that originated from North America with trajectories that ended at altitudes of 6100 and 5300 m, whereas the ones originating from over the Arctic Ocean resembled the trajectories that ended at altitudes of 6300, 6500 and 7300 m. Thus, the wind shear that was seen in the HYSPLIT simulations, was also found with FLEXPART. Since the simulated layer (6000 - 6700 m) included the northward and the south-westward turning plumes, the wind shear must have been located within this layer. Again, from the LIDAR results, it seemed like the altitude of the wind shear might have been too low, since the measured layer was located between altitudes of 6000 - 6700 m and even seemed to have extended further down. This allowed for an estimation of the altitude difference between the simulations and the measurements to a few hundred meters.

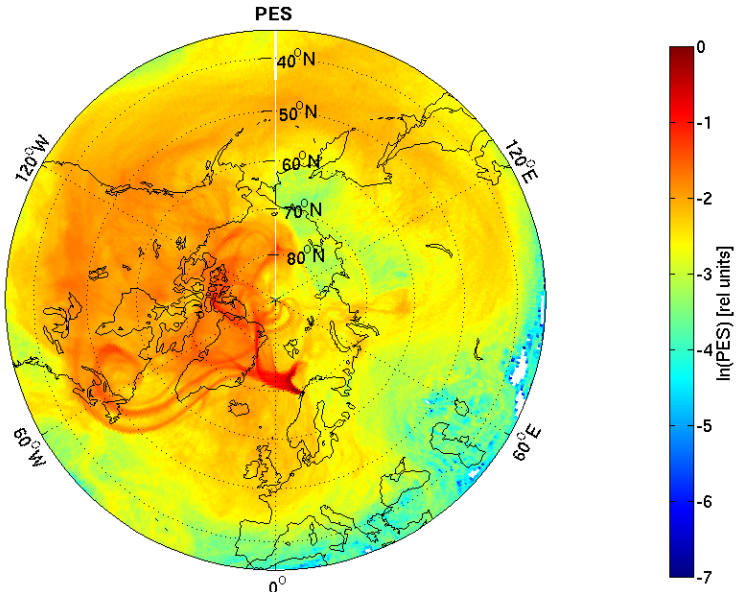

Figure 4.11: Time-averaged logarithmic relative FLEXPART PES for the potential aerosol layer (from 6000 - 6700 m, April 17, 2010). Maximum value 65.92 $\frac{s \cdot m}{kg}$. Averaging time was over the full extend of the FLEXPART simulation (from March 29, 2010 - April 17, 2010).

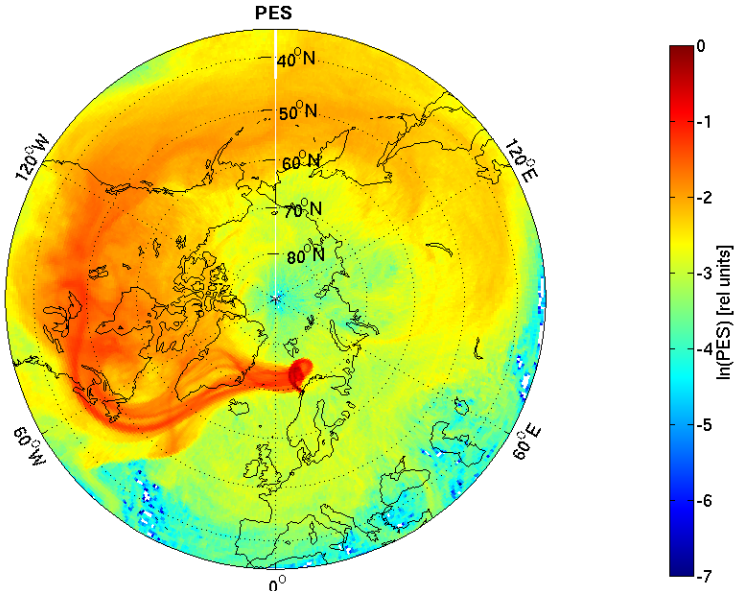

Figure 4.12: Time-averaged logarithmic relative FLEXPART PES from the layer 1000 m below the potential aerosol layer (from 5000 - 6000 m, April 17, 2010). Maximum value 84.71 $\frac{s \cdot m}{kg}$. Averaging time was over the full extend of the FLEXPART simulation (from March 29, 2010 - April 17, 2010).

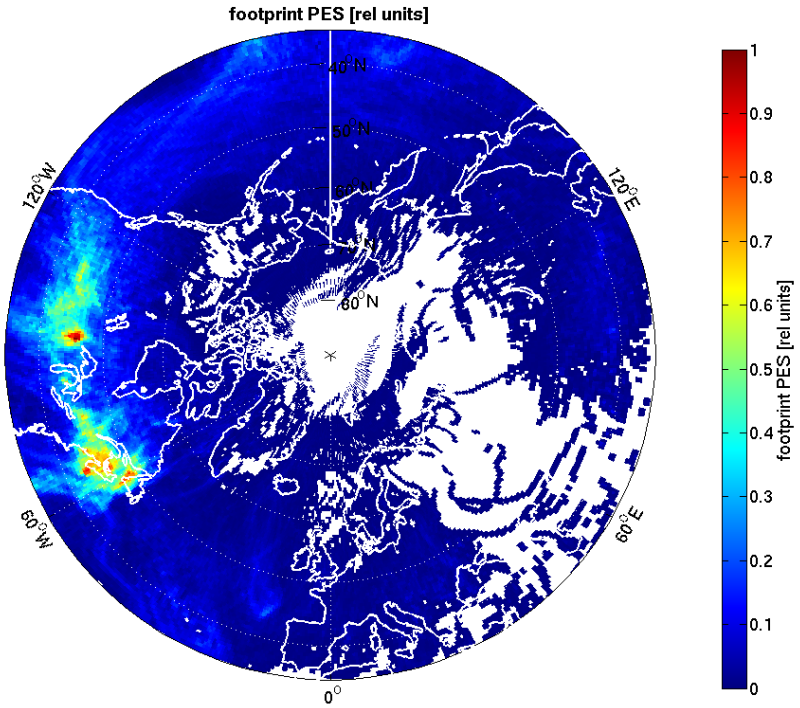

Figure 4.13: Time-averaged relative FLEXPART footprint PES for the potential aerosol layer (from 6000 - 6700 m, April 17, 2010). Footprint averaging height was 0 - 1000 m. Maximum value 0.48 $\frac{s \cdot m}{kg}$. Averaging time was over the full extend of the FLEXPART simulation (from March 29, 2010 - April 17, 2010).

A calculation of the footprint PES for both layers showed similar results, differing mostly in the maximum values of 0.48 $\frac{s \cdot m}{kg}$ for the potential aerosol layer and 1.38 $\frac{s \cdot m}{kg}$ for the layer below. Only the results from the potential aerosol layer are shown in Figure 4.13.

Two regions of high footprint PES were visible. The first region was located over Newfoundland and New Brunswick and the second one was located west of Lake Superior. A closer look at the daily averaged footprint PES yielded that the strong signal over Newfoundland and New Brunswick was caused by the circulation of the northern plume part, while the southern part had already passed the region (not shown). The footprint PES of the second region was more intense and connected to more direct transport.

The result of an overlay between the FLEXPART footprint PES with 24 days average MODIS CMG data is shown in Figure 4.14. A good correlation existed between relative fire cover (indicating high fire activity) and high footprint PES. The correlation between very high fire activity (with average total fire cover of more than 0.005 per grid-box) and high footprint PES was not as good, with the highest fire activity located a few grid-boxes further west.

The averaging time of the MODIS CMG data was 24 days, from March 30, 2010 to April 22, 2010. A high burning activity over this entire period was not expected and thus, it was necessary to analyse the temporal overlap between high fire activity and high footprint PES. Looking at the more intense fires at 37° N, 96° W over

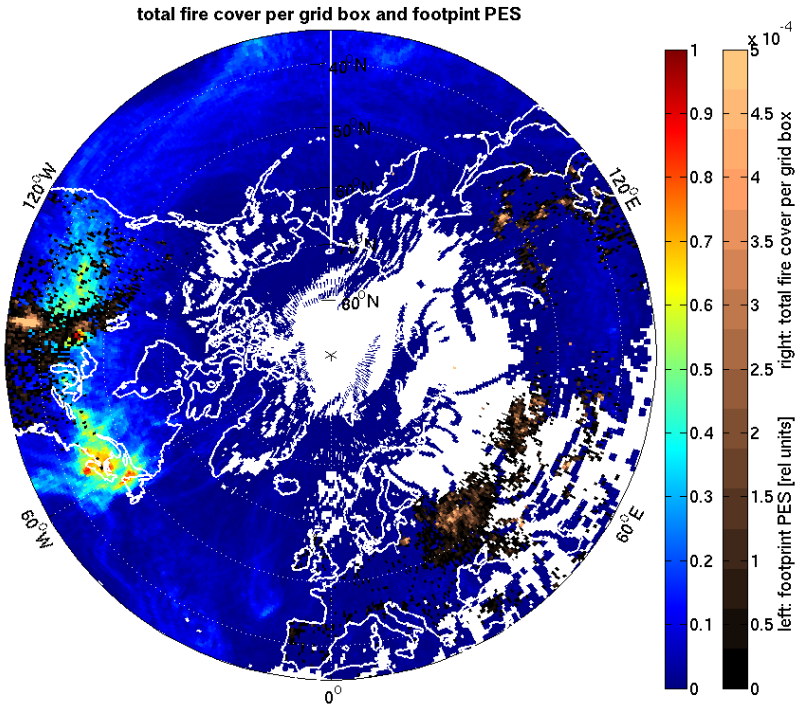

Figure 4.14: Time-averaged relative FLEXPART footprint PES for the potential aerosol layer (from 6000 - 6700 m, April 17, 2010) together with MODIS CMG relative fire cover per grid-box from March 30, 2010 - April 22, 2010. Footprint averaging height was 0 - 1000 m. Maximum value 0.48 $\frac{s \cdot m}{kg}$. Averaging time was over the full extend of the FLEXPART simulation (from March 29, 2010 - April 17, 2010).

Kansas and Oklahoma (from now on referred to as Kansas fires) in both Figures 4.13 and 4.14, it was found that the strongest fire activity covered a region of slightly increased footprint PES. Those fires could have contributed significantly to a potential aerosol layer above ALOMAR. To eliminate the possibility of a false positive identification of a wildfire plume and to analyse the contribution from the Kansas fires, it was necessary to identify the days, during which elevated PES occurred and to compare this with fire counts with higher temporal resolution.

Time-resolved PES

Figure 4.15 shows the PES from output step 15 - 22. Elevated footprint PES was found in output step 16 and 17, corresponding to April 10, 2010, 06:00 UTC - April 09, 2010, 18:00 UTC and April 09, 2010 18:00 UTC - 06:00 UTC. No elevated PES was visible in output step 15. In output step 18, the footprint PES was high over Newfoundland. The footprint PES in the Great Lakes region was lower than in step 16 and 17. Considering the difference in time of about 6 hours between UTC and local time, the build-up of highest PES took place only during April 09, 2010.

Burning activity was detected with MODIS at the same point and time.
A temporal and spatial overlap has been established between increased fire activity and elevated footprint PES for the region west of Lake Superior. The elevated footprint PES over Newfoundland indicated transport of air from that region into the layer above ALOMAR. The elevated PES around 38°N and 96°W in output step 21 could have indicated a contribution from the Kansas fires to the aerosol layer above ALOMAR, even though the highest fire counts were observed during earlier output steps.

Time-averaged PSC

Figure 4.16 shows the footprint PSC obtained as the product of the relative footprint PES and mean MODIS CMG relative fire cover and fire radiative power with averaging time from April 7 - 14, 2010. The PSC with the relative fire cover was highest over the Kansas fires. It appeared as if the stronger fires in the south might have had the biggest contribution to the plume above ALOMAR, despite their weak footprint PES. From the PSC with mean fire radiative power, the northern fires appeared to have had the bigger contribution.
Averaging time of the footprint PSC and the fire counts was still 7 days. To avoid an overestimation of the contribution from the Kansas fires, it was necessary to compare the build-up of high footprint PSC with daily wildfire detections.

Time-resolved PSC

The footprint PSC from April 09 - 12, 2010, obtained as the product of the daily averaged PES and the MODIS CMG relative fire cover and mean radiative power from April 07 - 14, 2010 is shown in Figure 4.17, together with daily MODIS wildfire counts. The highest fire numbers during April 09, 2010 and April 10, 2010 coincided with a very weak footprint PES at the Kansas fires, resulting in a lower footprint PSC than for the fires closer to the Great Lakes. During the build-up of the highest PSC during April 08, 2010, only few fires were found. Thus, the highest values of time-averaged footprint PSC were caused by the low temporal resolution of the MODIS CMG data. Judging from the FLEXPART analysis, the strong fires over Kansas did not have a significant contribution to the aerosol layer above ALOMAR.
Researchers from the University of Maryland reported high smoke pollution from Kansas in the Great Lakes states during April 10, 2010 [UMBC (2012)]. However, this was only public information on air pollution and no details were given on the exact extent of the plume.
It is possible that significant northward transport had taken place from the Kansas fires over to the Great Lakes. In that case, it is possible that the total amount of

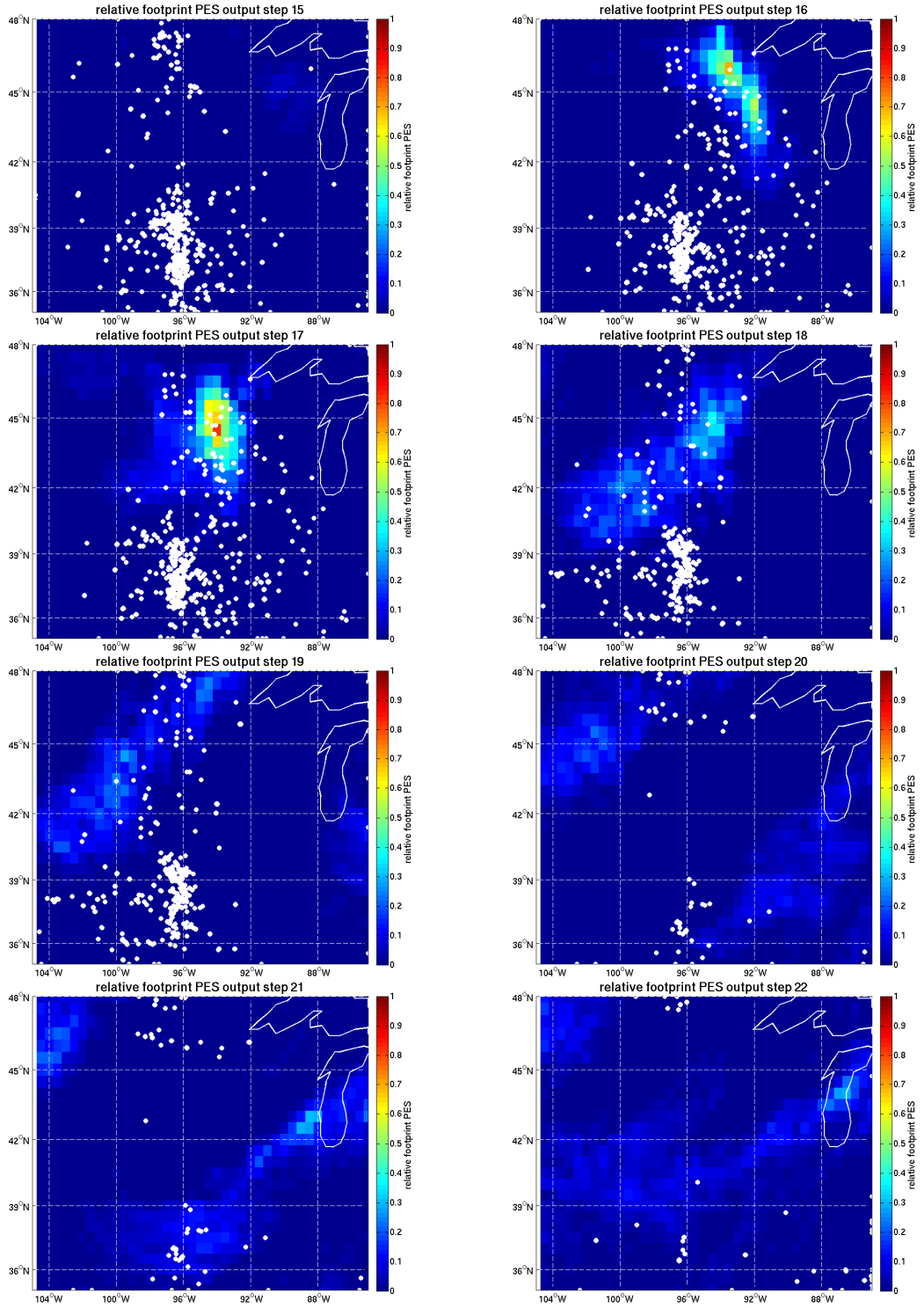

Figure 4.15: FLEXPART footprint PES for the 12-hourly output steps 15 - 22. White tick marks indicate MODIS daily fire detections. Magnification of the area south-west of the Great Lakes. MODIS fire detections were sampled sun synchronous around 13:30 and 10:30 LST. FLEXPART averaging time was 12 hours backwards in time, starting April 10, 2010, 18:00 - 06:00 UTC, corresponding to 12:00 - 00:00 LST at the potential source region for output step 15.

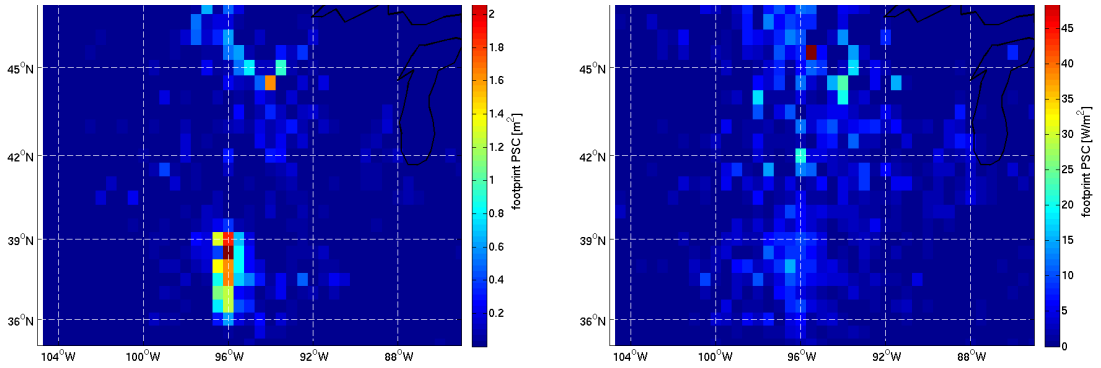

Figure 4.16: Time-averaged FLEXPART footprint PSC, obtained as the product of the averaged footprint PES and MODIS CMG relative fire cover (left) and fire radiative power (right). Magnification of the area south-west of the Great Lakes. Averaging time was from April 7 - 14, 2010.

aerosols that was transported towards ALOMAR was dominated through indirect transport from the strong Kansas fires. This could have been underestimated by the FLEXPART simulation. An error in the range of a few hundred kilometres cannot be ruled out after a transport time of 9 days and a distance of more than 10000 km [Stohl (2012)].
The analysis of the results from the simulation of the layer 1000 m below the potential aerosol layer showed a similar pattern and is therefore not discussed. An analysis of the simulation of the layer 1000 m above the potential aerosol layer above ALOMAR showed only transport from the Arctic Ocean.
The footprint PES was calculated for a layer that extended up to an altitude of 1000 m. A high footprint PES therefore corresponded to emissions into the lowest parts of the PBL. An analysis with a footprint layer extending up to 3000 m showed no significant difference in overlap between fire activity and transport.
Pollution in the region west and south of the Great Lakes seemed to have mostly been dominated by wildfire activity. No other source region was found that could have led to an extended aerosol layer above ALOMAR. Low relative humidity indicated the absence of clouds. However, no in situ measurements of the plume properties were taken that could have provided a definitive confirmation that the plume above ALOMAR was caused by wildfire aerosols. The altitude difference between measurements and the models could have been caused by self-lifting. Such lifting would neither have been simulated in FLEXPART, nor in HYSPLIT.
Because of the high overlap between the MODIS CMG fire detections and the FLEXPART results, the layer of increased LIDAR signal between 6000 and 6700 m during April 17, 2010 was identified as a wildfire aerosol layer.

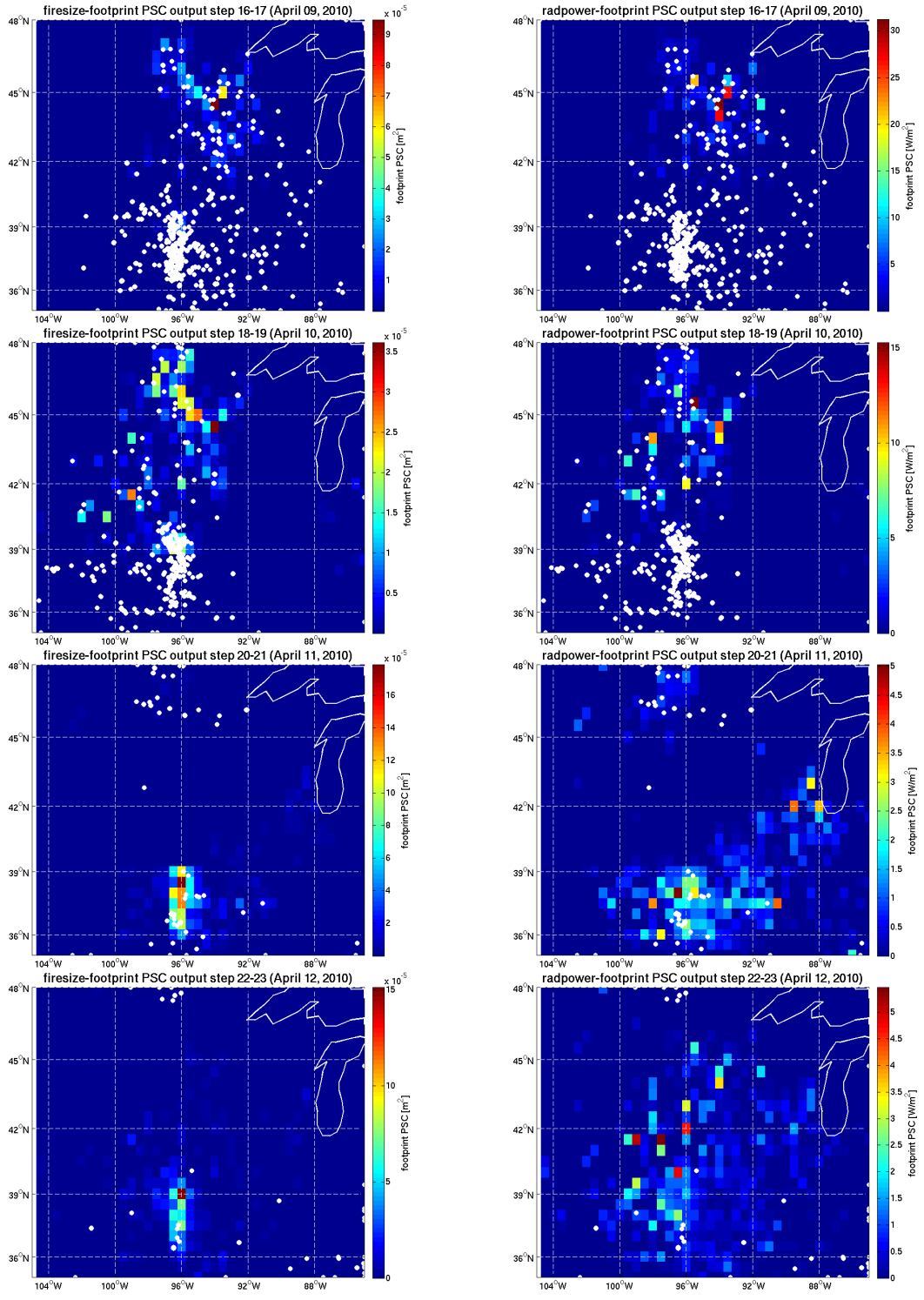

Figure 4.17: FLEXPART footprint PSC from April 09 - 12, 2010, obtained as the product of the relative daily averaged footprint PES and MODIS CMG relative fire cover (left) and fire radiative power (right) from April 07 - 14, 2010. White tick marks indicate MODIS daily fire detections. A missing overlap between the white tick marks and the PSC indicates a misidentification of high PSC due to the low temporal resolution of the MODIS CMG fire data. Magnification of the area south-west of the Great Lakes.

4.3 Weather maps

To illustrate the weather situation during the fire emissions, surface weather maps over the U.S. during April 09 and 10, 2010 are shown in Figure 4.18. From April 09 - 10, 2010, a cold front (blue line) passed the Kansas fires. An occluded front (purple line) passed the fires next to Lake Superior.
During April 09, 2010, two low-pressure systems were located over central and south-eastern Canada. One high-pressure system was located over the south-eastern U.S. and one high-pressure system extended from western Canada down to the north-central U.S. During April 10, 2010, the low-pressure systems were intact and had been advected in an eastward direction. The high-pressure system over the south-eastern U.S. had been advected towards the north-east and increased in size, covering almost the entire eastern U.S..
The 24-hourly total precipitation is shown in Figure 4.19. No precipitation took place over the fire sites between April 08, 2010, 07:00 UTC and April 09, 2010, 07:00 UTC. An area of precipitation was located over Lake Ontario. Between April 09, 2010, 07:00 UTC and April 10, 2010, 07:00 UTC, little precipitation took place over the fires next to Lake Superior. No more fires were observed in this area from April 10, 2010 (Figure 4.17). No precipitation took place over the Kansas fires.

4.4 WRF-Chem transport analysis

The LIDAR measurement from April 17, 2010 showed a single, clearly defined layer of wildfire aerosols. A high correlation was found between the FLEXPART source specifications and MODIS wildfire detections. No signals of elevated moisture and clouds were found in the air above Bodø and ALOMAR during the measurement time. This case was chosen as case-study with WRF-Chem for the analysis of self-lifting. To get a better impression of the transport of the plume from the fires towards ALOMAR, the most important steps in the development of the plume are presented here.

Figures 4.20 - 4.23 show the temporal evolution of the plume (hereafter referred to as plume A), as it was advected towards Andøya. The positions of the plume were found by manually following the relatively isolated, elevated BC signal backwards in time from above ALOMAR to the emission region. Thus, the positions of the plume became more uncertain towards the emissions and it was not possible to determine the exact emission region to a high degree of certainty. However, the region with the highest time-averaged FLEXPART PES fell into the region of possible emissions. The two strongest fires in that region are marked with arrows in Figure 4.20 (top). The left fire (white arrow) will be referred to as fire 1 and the right one (red arrow) as fire 2. The positions of plume A are indicated with black rectangles.
The highest aerosol concentrations were observed 3 h after the emission maximum, when the emission strength was still 85 %. The vertical profile of the BC concentration through the highest concentrations in the lowest atmospheric layer showed that the plumes reached altitudes of up to 4500 m close to the emission sites (Fig-

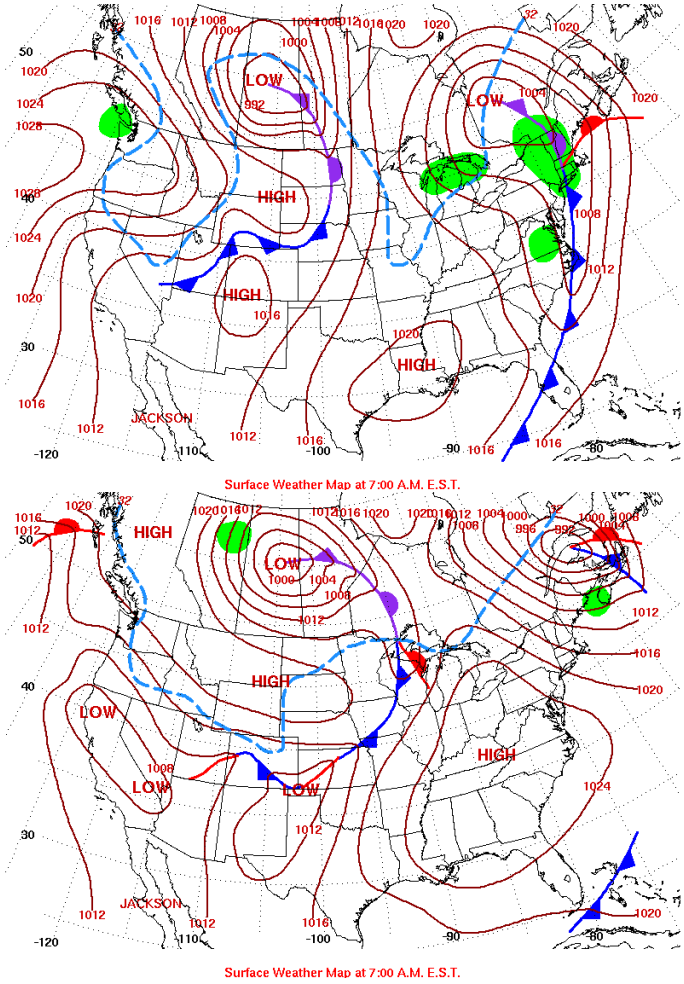

Figure 4.18: NCEP surface weather analysis over the U.S. during April 09, 2010 (top panel) and April 10, 2010 (bottom panel). Analysis times were 07:00 EST, corresponding to 02:00 UTC.

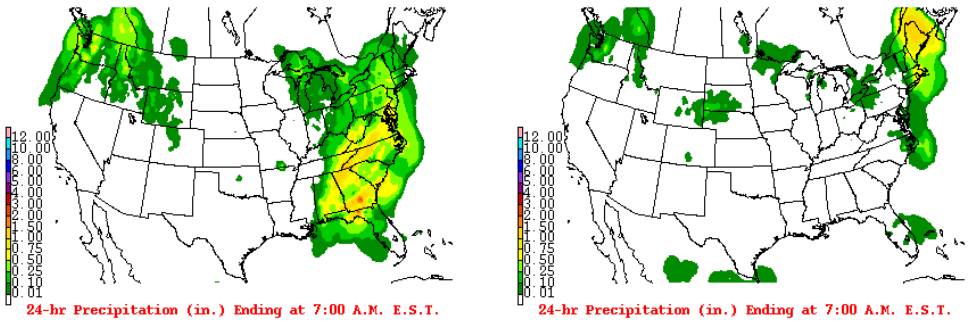

Figure 4.19: NCEP total 24-hr precipitation (inch) over the U.S. ending at 07:00 EST April 09 (left panel) and 10 (right panel), 2010 corresponding to 02:00 UTC, respectively.

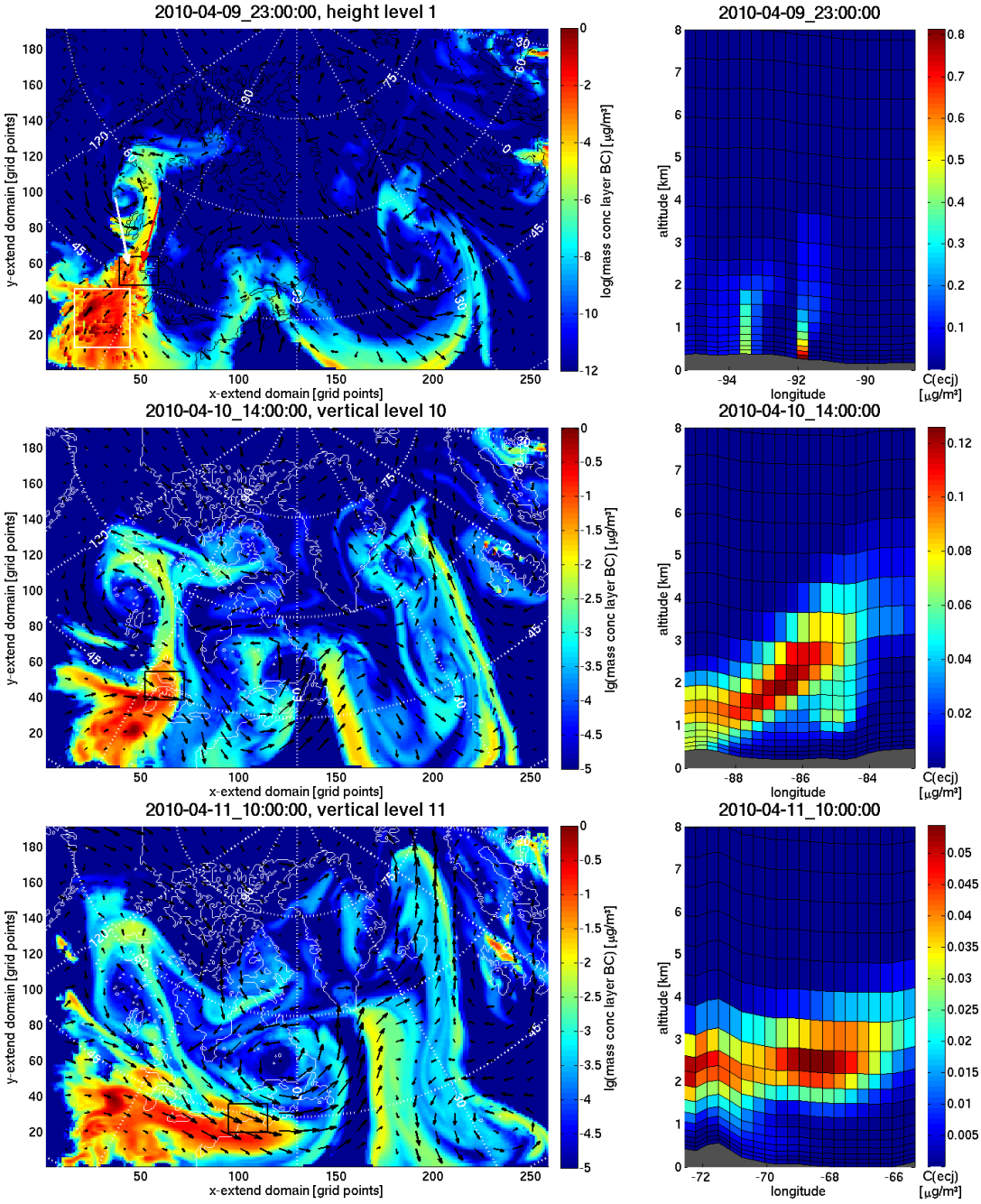

Figure 4.20: WRF-Chem BC concentration between April 09, 2010 (time of the fire emissions) and April 17, 2010 (time of the detection at ALOMAR). Times (in UTC) are given in the subfigure titles. The left panels show a horizontal cut through the domain (the altitude levels are given in the Figure captions). The right panels show a vertical cut through the domain along the x-direction (not along constant latitude). Black rectangles indicate the position of plume A (the plume that was transported towards ALOMAR). Grey space on the lower part of the vertical plots indicates topography. The position of the vertical cuts is always the horizontal symmetry axis of the black rectangles. The two strongest fires contributing to plume A are marked with arrows (white arrow for fire 1, red for fire 2). Only one plot is given for the time of maximum concentration at the emission site. The plume from fire 1 can be seen on the left side of the vertical cut. The values are somewhat low, since the cut was placed over fire 2 and thus, one grid point upwind of fire 1. The emission region for plume B is indicated with a white rectangle. The output times are chosen to illustrate the most important steps in the development of plume A.

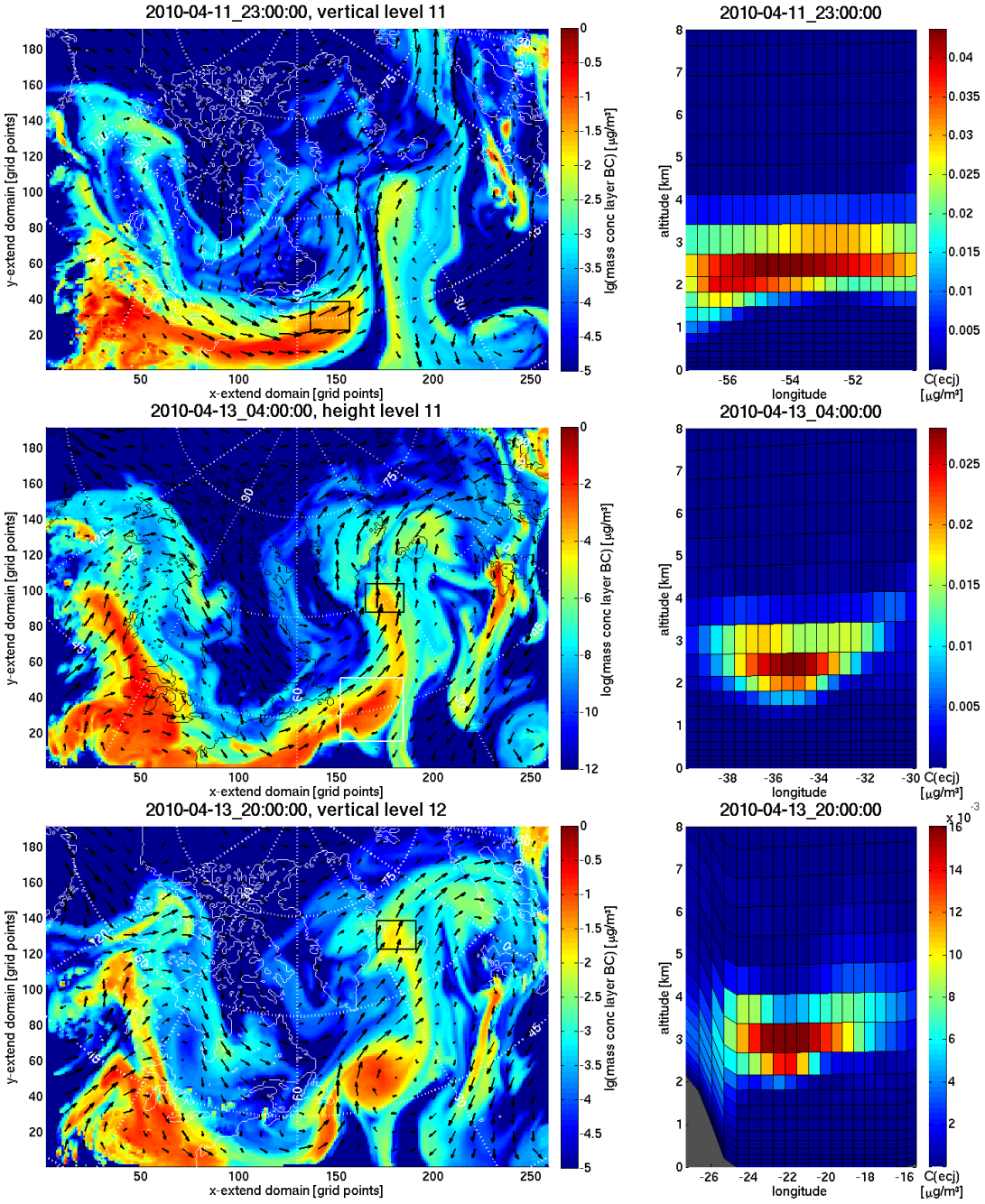

Figure 4.21: Same as for Figure 4.20 for output times April 11, 2010, 23:00 UTC - April 13, 2010, 20:00 UTC. Plume B is indicated with a white rectangle in the centre panel.

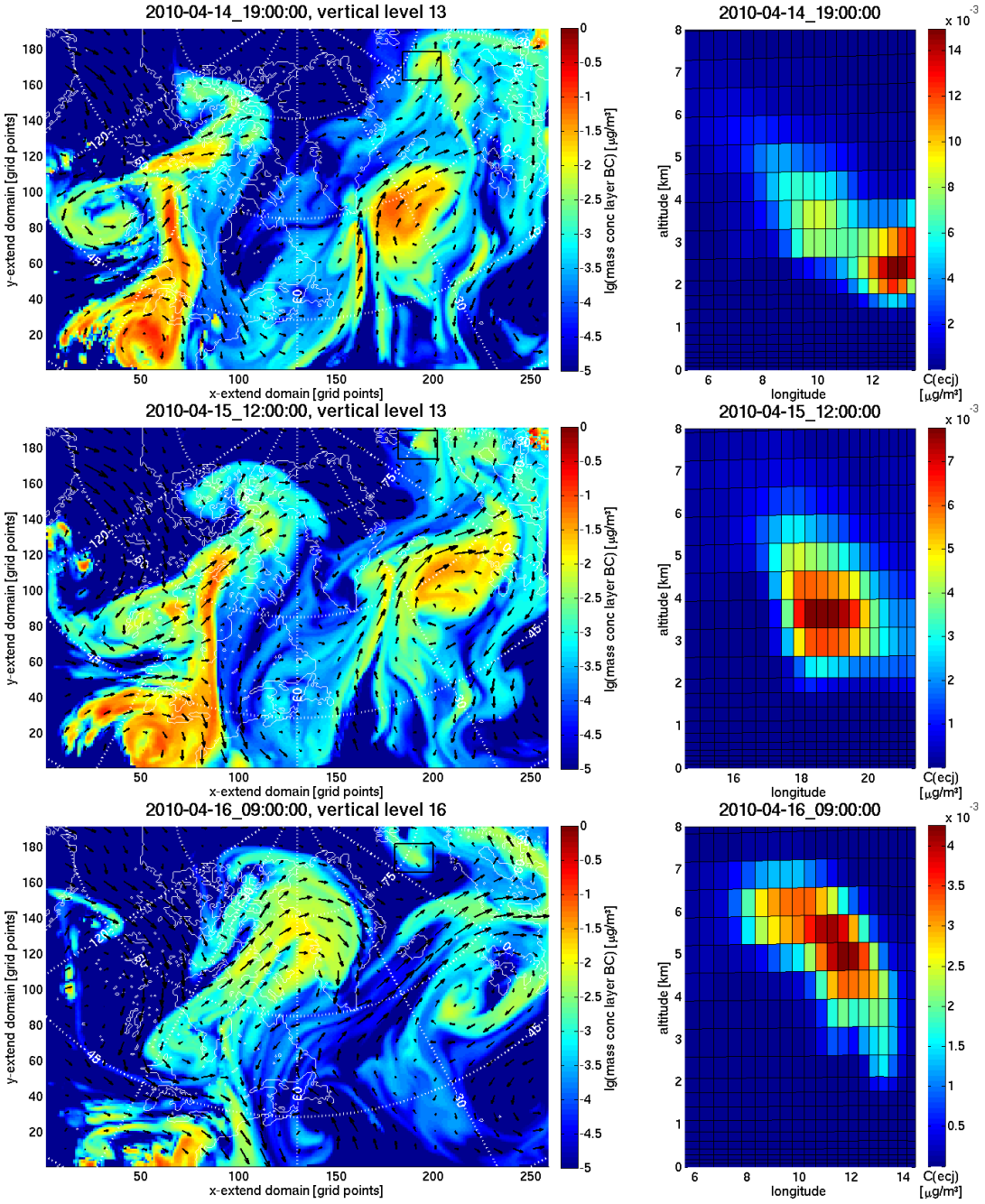

Figure 4.22: Same as for Figure 4.20 for output times April 14, 2010, 19:00 UTC - April 16, 2010, 09:00 UTC.

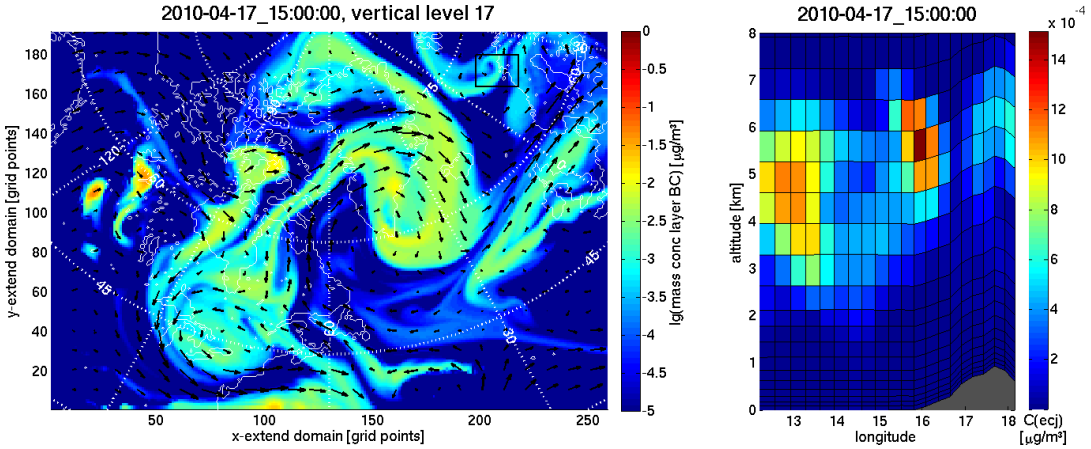

Figure 4.23: Same as for Figure 4.20 for output time April 17, 2010, 15:00 UTC.

ure 4.24 [1,1] and [1,2]). The BC concentration for fire 1 decreased with altitude, following a logarithmic function. The BC concentration for fire 2 decreased with altitude, following a logarithmic function up to an altitude of 1700 m and showed an elevated plume in altitudes between 2000 and 4000 m with maximum BC concentration around 2500 m.

15 hours later, the plume was located over Lake Superior (Figure 4.20, middle). The plume reached up to a maximum altitude of 5 km with maximum BC concentration around 2400 m (Figure 4.24 [1,3]). In the south, plume A fused together with the plume from the Kansas fires (hereafter referred to as plume B). Both were advected together in eastward direction by a strong wind field on the south side of the cyclonic vorticity anomaly around a low-pressure system with the centre over Newfoundland and Labrador (Figure 4.20, middle and bottom) that was also seen in the weather maps (Figure 4.18, bottom).

The plumes split again 48 h after the emissions (Figure 4.21 (top)). Plume A was advected in northward direction by the strong winds aside the cyclonic anomaly and plume B was advected in eastward direction. The splitting happened in connection with a developing anticyclonic vorticity anomaly that was first seen in Figure 4.21 (middle). Plume A was advected at an increased speed between the dissipating cyclonic anomaly and the anticyclonic anomaly. Shearing winds protracted the plume and led to efficient dilution. Plume B was relatively confined in space by the size of the anticyclonic anomaly, keeping it intact and in the same altitude over a longer period, while transporting it in an eastward direction.

Based on the long, parallel transport, it was expected that both plumes might have undergone some degree of mixing. From FLEXPART source specifications, the degree of direct mixing during transport appeared small since otherwise, an elevated PES and PSC would have been found at the Kansas fires temporally coinciding with the build-up of the high PES at the fires west of Lake Superior. However, only a minor misplacement of the wind fields in Figure 4.20 (bottom) and 4.22 (top) could have led to a much higher contribution from the more active Kansas fires. The cyclonic vorticity anomaly that was found during April 11, 2010 was probably the reason for the increased PES over Newfoundland and New Brunswick. The degree

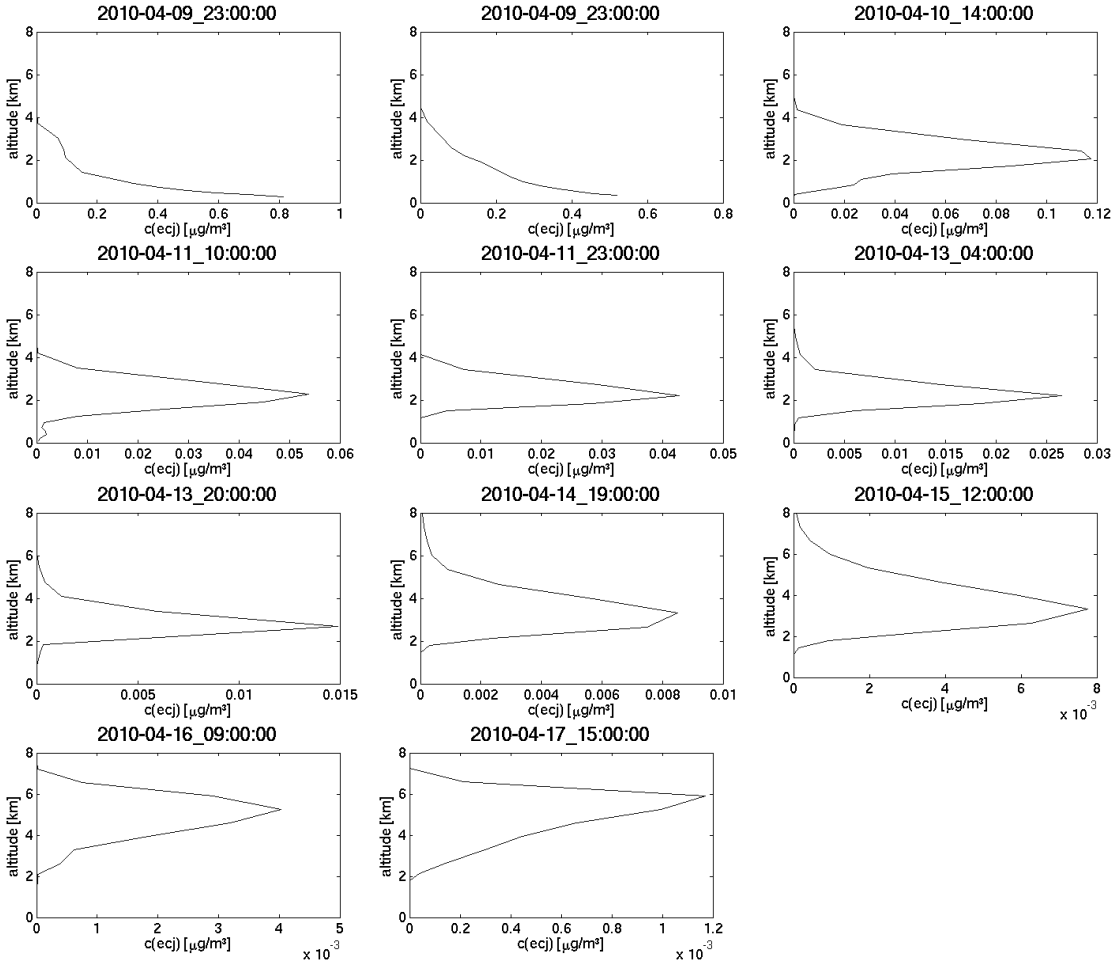

Figure 4.24: Vertical profile of WRF-Chem BC concentration at the maximum concentration of plume A for the same output times as Figures 4.20 - 4.23. An additional panel is added for fire 2 during April 09, 23:00 UTC. The Matlab pcolor function was used for the vertical profiles in Figures 4.20 - 4.23. This function assumes grid points at the edge of the pixels, instead of the centre. Thus, the more correct altitudes from this plot differ from the altitudes in the vertical cut by $\frac{1}{2}$ grid height. For easier referencing in the text, the panels of this figure are counted [row, column].

of mixing from that clear region into the aerosol layer above ALOMAR was also dependent on the placement of the wind fields. This was a potential source of high uncertainty for the simulated strength of the aerosol layer above ALOMAR.
Coming back to plume A: Another splitting was observed in Figure 4.22 (top). The splitting was caused by a wind-shear off the coast of northern Norway. 133 h after the emissions (Figure 4.22, middle), the eastern plume had been transported out of the computational domain. The western plume part was advected further by a cyclonic vorticity anomaly and redirected back towards northern Norway.
During the next few hours, the plume underwent vertical transport (Figures 4.24 [3,3] and [4,1]) in connection with a low-pressure system with the centre at the position of the plume, clouds below and at the altitude of the plume and rain release below. The rising motion combined with high moisture suggested transport by a

warm conveyor belt, as studied by Cooper et al. (2004). 154 h after the emissions, the plume maximum was at around 5300 m altitude (Figure 4.22, bottom). Plume A finally arrived above ALOMAR as a thin but elongated signal with maximum strength around $1.2 \cdot 10^{-3}$ $\frac{\mu g}{m^3}$ at an altitude around 5920 m (Figure 4.24 [4,2]).
The altitude of maximum plume strength was around 400 m too low, which was consistent with the FLEXPART simulations. Nudging of the horizontal velocities was used in the WRF-Chem simulation, forcing the simulation towards the observations and allowing for a comparison between the FLEXPART and WRF-Chem simulations (both used the same input data, only with different resolution).
The simulated aerosol layer was extending further down towards the ground than in the LIDAR measurements, suggesting a higher vertical dispersion within the layer. The low vertical resolution (chosen for run-time efficiency) could have had an influence on the vertical dispersion. The ratio between BC and total pm25 aerosol concentrations (all aerosols smaller than $2.5\mu m$) was around $\frac{1}{10}$, leading to a total maximum pm25 concentration of around $1.2 \cdot 10^{-2}$ $\frac{\mu g}{m^3}$. This value seemed very low for an aerosol layer to be recognisable with a LIDAR instrument, even against clear polar background air.
At this point, the altitude differences between the observations and analysis could not be explained by self-lifting, as hypothesised in subsection 4.2.5.

4.4.1 Comparison of the simulated AOD to measurements

Comparison directly after the emissions

The simulated aerosol concentrations above ALOMAR were low. Therefore, it was decided to compare the simulated AOD to AOD measurements.
First, MODIS AOD measurements were used to validate the wildfire emission rates. Preferably, the comparison would have been done between identical wavelengths. However, WRF-Chem AOD was calculated at 300, 400, 600 and 1000 nm and MODIS AOD data were provided at 550 nm. The Ångstrøm exponent between 400 and 600 nm was used to calculate the simulated AOD at 550 nm.
A comparison between the measured and simulated AOD was only possible during April 10, 2010. The aerosols were emitted during April 09, 2010. Possible timing errors through the diurnal cycle of the FINN emissions (Section 3.10.3) would have caused unnecessary confusion during that day. During April 11 and 12, 2010, MODIS and GOES satellite images (not shown) displayed clouds at the simulated location of the plume, possibly leading to large uncertainties in the MODIS AOD retrievals.
The simulation strongly underestimated the AOD. It was unknown, whether the emission rates per fire were too low or if strong fires were missed entirely because of cloud contamination or thick smoke plumes that prevented the detection of the underlying fires. Adding fires to the emission regions was not considered useful, since it was unknown, where to add those fires and with what emission rates. A test-simulation was done, scaling the original emissions per fire by a factor of 10.
The column integrated MODIS and WRF-Chem AOD with scaled emissions are

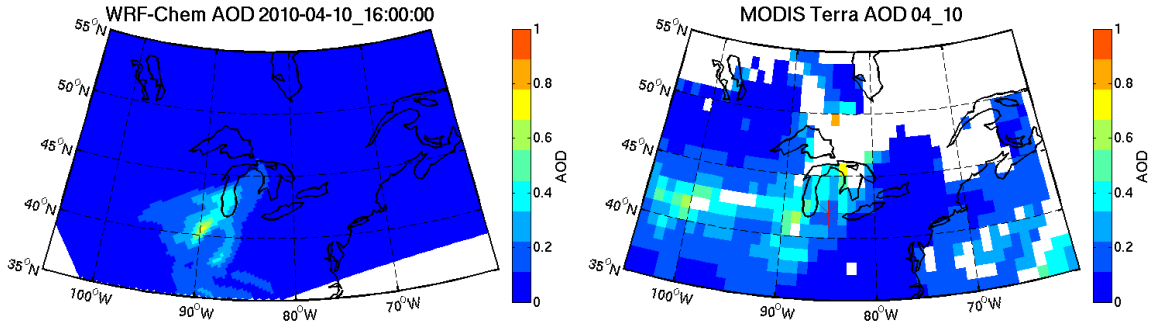

Figure 4.25: Column integrated AOD at 550 nm from WRF-Chem (left panel) with 10-times increased aerosol emissions and MODIS Terra (right panel) from April 10, 2010. Satellite passing time of MODIS Terra was around 10:30 **L**ocal **S**olar **T**ime (LST), corresponding to around 19:00 UTC. The Great Lakes can be seen in the centre of the plots. The position of the Kellog **L**ong-**T**erm **E**cological **R**esearch (LTER) sun-photometer is indicated with a tick mark in the plot for the MODIS measurement.

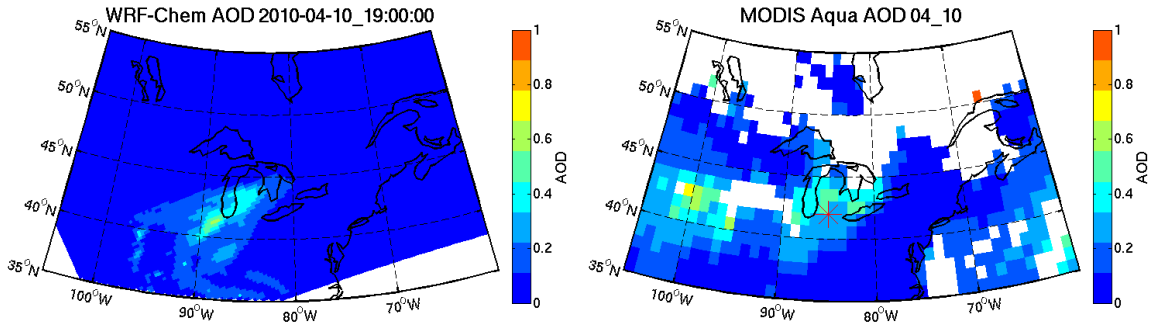

Figure 4.26: Column integrated AOD at 550 nm from WRF-Chem (left panel) with 10-times increased aerosol emissions and MODIS Aqua (right panel) from April 10, 2010. Satellite passing time of MODIS Aqua was around 10:30 LST, corresponding to around 19:00 UTC. The Great Lakes can be seen in the centre of the plots. The position of the Kellog (LTER) sun-photometer is indicated with a tick mark in the plot for the MODIS measurement.

shown in Figures 4.25 and 4.26. The region of elevated AOD around 40° N, 90° W and extending over Chicago and Lake Michigan (corresponding to plume B, Section 4.4), was found in both the MODIS Terra measurement and the corresponding simulation. A comparison between the later MODIS Aqua measurement and the simulation is shown in Figure 4.26. The centre of the plume has been advected further to the north-east in both the measurement and the simulation. Overall, during both satellite over flights, the simulated plumes were located further south-west than in the measurements. Plume A was visible neither in the measurements nor in the simulation; the column integrated AOD was probably too low.

The discrepancy in the location of the plumes could have been caused by the diurnal cycle of the FINN emissions (Section 3.10.3). With the overall transport in north-eastward direction it appeared, as if aerosols were emitted too late in the simulation.

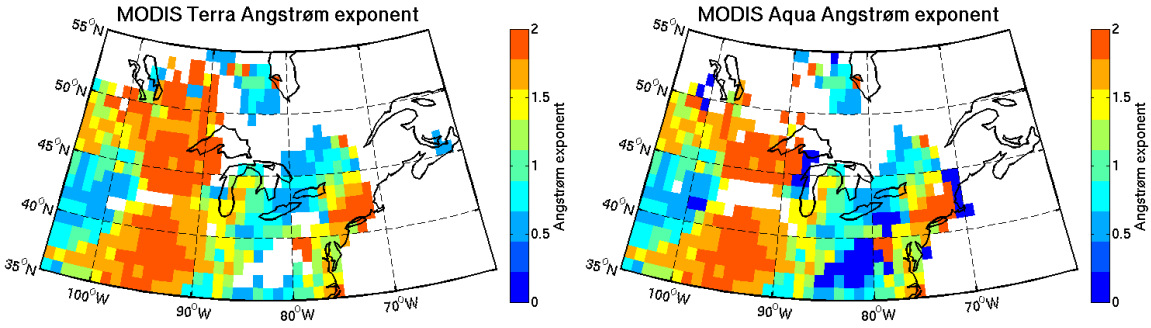

Figure 4.27: Column integrated Ångstrøm exponent between 470 and 660 nm from MODIS Terra (left panel) and Aqua (right panel) from April 10, 2010. The Great Lakes can be seen in the centre of the plots.

The region of elevated AOD in the measurements around 42° N, 100° W was not reproduced by the simulation. A short discussion is given here, if that could have been wildfire aerosols which might have been entirely missed by the simulation.
The Ångstrøm exponent of fresh wildfire aerosols was reported between 1.2 and 2.3 [Reid et al. (2005)]. The Ångstrøm exponent of around 1.5 at the plumes that were reproduced by the simulations (40° N, 88° W) fitted well within those values (Figure 4.27). The Ångstrøm exponent in the region around 42° N, 100° W was around 0.6, suggesting larger particles like dust or pollen. From a HYSPLIT backward-trajectory, the origin of this atmospheric column was further west, outside the computational domain.
A comparison with the only close-by sun-photometer (Michigan state University Kellog (LTER) station [NASA (2012a)], tick marks in Figures 4.26 and 4.25) was difficult, because of the strong horizontal gradient in AOD. However, values during overpass time fitted within the range of the MODIS measurements.
Scaling the emissions by a factor of 10 led to a good agreement between the measurements and the simulations. Even though the highest contribution to the AOD over Lake Michigan was caused by wildfire aerosols, anthropogenic emissions might still have had some contribution. The WRF-Chem simulation did not include anthropogenic emissions. If that is taken into account, the simulations with 10 times the original FINN emissions probably overestimated the wildfire attributed AOD, suggesting an actual underestimation of the original emissions by a factor lower than 10. However, the contribution from anthropogenic emissions to the aerosol layer above ALOMAR was concluded to be small because of the good agreement in spatial distribution of elevated AOD between satellite measurements and simulations (it is unlikely that two weak sources at two different locations produce a similar spatial distribution as one strong source).

Comparison after 8 days of transport

The aerosol layer above ALOMAR was reproduced by the WRF-Chem simulation in Section 4.4. However, the simulated aerosol concentrations above ALOMAR seemed

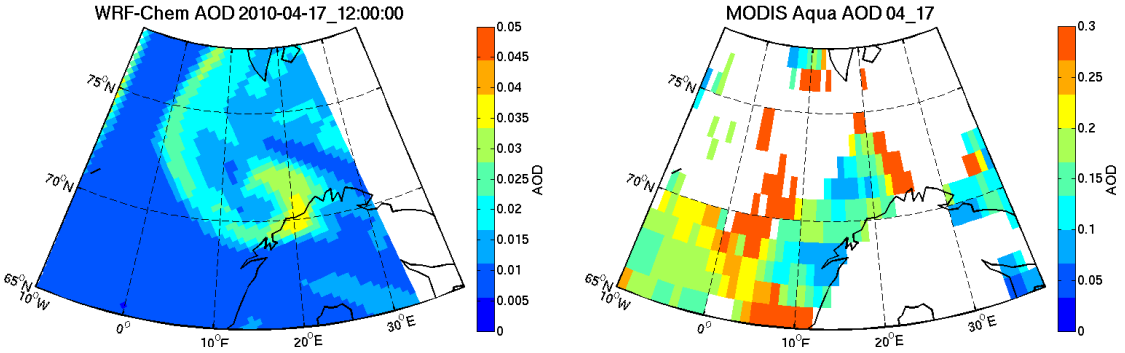

Figure 4.28: Column integrated AOD at 550 nm from WRF-Chem with 100-times increased aerosol emissions (left panel) and MODIS Aqua (right panel) from April 17, 2010. Satellite passing time of MODIS Aqua over the centre of the plume was around 13:30 local solar time, corresponding to around 12:30 UTC. northern Scandinavia is indicated in the lower right of the plots. Note the different scales of the colorbars.

very low. In the last paragraph, a comparison of the column integrated AOD from MODIS measurements and WRF-Chem simulations led to the conclusion that emissions were underestimated by around a factor of 10. An analysis of the simulated AOD for the scaled emissions showed almost no elevated AOD signal over ALOMAR during April 17, 2010.

The apparent inconsistency of existing aerosols without an elevated AOD was probably caused by the initialisation of aerosols in WRF-Chem. All aerosol species except for sulphate were assumed to have long chemical life-times and little production within the free atmosphere. Therefore, those aerosol species were initialised with a low background concentration of $10^{-16}\frac{\mu g}{kg(dry\ air)}$. Sulphate aerosols were initialised with higher concentrations because of the constant production from SO_2. Because of this, it was possible to identify a weak layer of aerosols other than sulphate, whereas the AOD signal from that layer was masked by the sulphate signal.

A plot of the AOD from a test simulation with 100 times increased wildfire emissions is shown in Figure 4.28 (left panel). The simultaneously measured MODIS Aqua AOD is shown in Figure 4.28 (right panel). The measured AOD over the ocean is highly elevated. The reason for those high values is unknown, but the measurements could have been biased by cloud contamination. A comparison between the simulated plume shape and the measurements was inconclusive because of the overall low AOD in the respective region and the high background AOD around. However, the plume shapes were similar over the Norwegian coast around 70° north, 20° east. The AOD from MODIS was only used for a comparison of the plume shapes. A quantitative comparison of the simulated AOD was done with the more exact AOD from the sun-photometer.

Figure 4.29 shows the AOD measurement from April 17, 2010. The AOD at 500 nm at 12:30 was around 0.09, the maximum value during that day was around 0.105. The simulated AOD at 500 nm was calculated using the Ångstrøm exponent between 400 and 600 nm. The result is shown in Figure 4.30. A maximum AOD of 0.029 was observed between 12:00 - 13:00 UTC. The decrease in AOD that was observed in the sun-photometer measurements from 16:00 UTC was found in the WRF-Chem

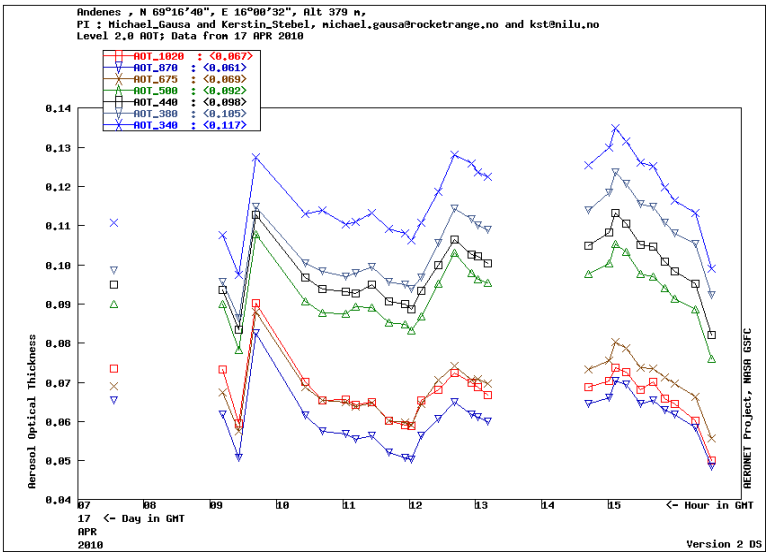

Figure 4.29: Time-resolved CIMEL sun-photometer AOD measurement above ALOMAR, April 17, 2010 for different wavelengths. The wavelengths are denoted in the legend.

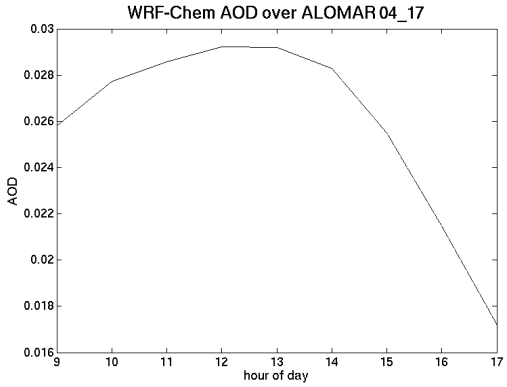

Figure 4.30: Time-resolved WRF-Chem AOD at 500 nm above ALOMAR, April 17, 2010.

simulation around two hours earlier.

From other measurements with the sun-photometer, the AOD for relatively clean air was found to be around 0.04. Considering this as background, the underestimation of the simulations with increased emissions was around a factor of 2. However, the actual background aerosol burden during the sun-photometer measurement was unknown.

An indicator for an increased background aerosol burden was the increased LIDAR signal up to an altitude around 1.5 km, displaying a stronger signal than the elevated layer (Figure 4.1). Hence, the difference of a factor of 2 should be understood as an upper limit.

The Ångstrøm exponent from the sun-photometer measurement fitted well with values that have been retrieved for aged smoke particles [Murayama et al. (2004), Mattis et al. (2004)], but might have been biased by the pollution in the PBL. A comparison of the simulated Ångstrøm exponents to the measurements showed an

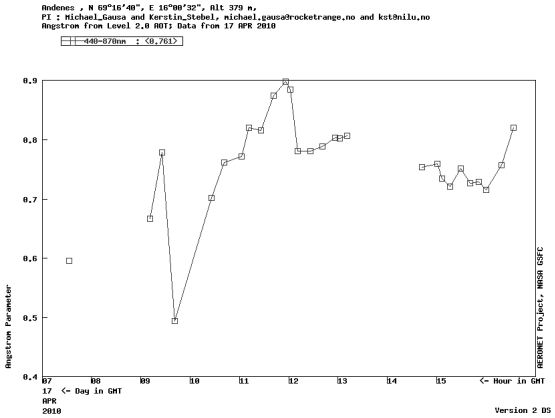

Figure 4.31: Time-resolved CIMEL sun-photometer Ångstrøm exponent between 440 and 870 nm above ALOMAR, April 17, 2010.

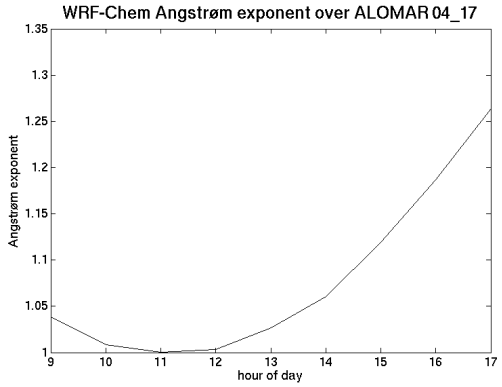

Figure 4.32: Time-resolved WRF-Chem Ångstrøm exponent between 400 and 600 nm above ALOMAR, April 17, 2010.

overestimation in WRF-Chem that could have been caused by the too low simulated aerosol concentrations, preventing coagulation or by a contamination of the sun-photometer measurement with large particles like sea salt. The strong influence of the concentration on coagulation can directly be seen from the anticorrelation of the simulated AOD and Ångstrøm exponent (Figures 4.31 and 4.32).

Following the previous argumentation, no other sources were found that could have caused the elevated LIDAR signal above ALOMAR during April 17, 2010. Together with the results from the comparison during the first day after the emissions in the last subsection, it was hypothesised that errors in transport led to a strong underestimation of the simulated aerosol concentrations above ALOMAR by around a factor of 20, even though the underestimation could have been lower because of uncertainties in the influence of background aerosol contamination on the sun-photometer measurement.

Uncertainties in wet-scavenging could have accounted for some of the underestimation of aerosol concentrations above ALOMAR. A test-run was conducted with suppressed grid-resolved wet-scavenging. The aerosol concentrations increased by a factor of three. However, even when grid-resolved wet-scavenging was ignored, the

aerosol concentrations for the corrected (10-times) emissions were still too low. It was not possible to suppress subgrid wet-scavenging in this version of WRF-Chem. Its effect on the aerosol concentrations above ALOMAR remained unknown. From the discussion in Section 4.6.2, subgrid wet-scavenging was around 100 times less efficient than grid-resolved wet-scavenging. Thus, the contribution to the underestimation of aerosol concentrations above ALOMAR was probably small.
The aerosol plume was split at least twice during transport (Figures 4.20 - 4.23). Both times, only a weak part of the plume was advected further towards ALOMAR. It is hypothesised that a minor misplacement of the wind fields or a minor change in timing could have led to e.g. a strong underestimation of the contribution from the Kansas fires to plume A.

4.5 Influence of the Eyjafjallajökull eruption

The LIDAR measurement during April 17, 2010 coincided with the Eyjafjallajökull eruption in April and May, 2010. Since the simulated aerosol concentrations above ALOMAR did not fit well with the measurements, a short discussion is given on, whether the LIDAR measurement might have been influenced by the volcanic eruption.
The maximum measured PDR was around 2.1%. Ansmann et al. (2010) found a PDR as high as 35% for the Eyjafjallajökull plume, resulting in a factor of 16.7 between the PDR of the volcanic ash plume and the potential aerosol layer. Even without calibration, the PDR of the layer above ALOMAR would still have been too small by a factor of around 3.6 compared to the ash.
HYSPLIT results (Figure 4.7 and 4.8) showed no trajectories passing over Iceland. The trace of high FLEXPART PES in Figure 4.11 and 4.12 passed Iceland in the north-west, whereas the eruption site was located in the south. An analysis of the time-resolved PES (not shown) yielded that the elevated PES over Iceland in Figure 4.11 was not built up before simulation day 9, corresponding to April 8 and 9, 2010, 6 days before the first ash plumes were emitted by the volcano. No PES was built up over Iceland at a later time (from April 9 - 17, 2010). FLEXPART forward runs from the volcanic eruption confirmed that no ash existed over ALOMAR during April 17, 2010 [Stohl et al. (2011)].
In the WRF-Chem simulations (Figure 4.21, bottom) a part of the fire plume was indeed transported over Iceland. However, plume A underwent splitting (Figure 4.22). The left plume part was detected above ALOMAR, whereas the right plume part that passed Iceland was transported out of the computational domain.
The LIDAR PDR and all model results pointed against an influence from the Eyjafjallajökull eruption on the situation above ALOMAR during April 17, 2010.

abbreviation	scaling-factor emissions	emissions from...until	wet-scavenging
10-l-w(-a, -n)	10	04/04 - 04/18	yes
10-s-w(-a, -n)	10	04/04 - 04/10	yes
10-s-n(-a, -n)	10	04/04 - 04/10	no
50-l-w(-a, -n)	50	04/04 - 04/18	yes
50-s-w(-a, -n)	50	04/04 - 04/10	yes
50-s-n(-a, -n)	50	04/04 - 04/10	no
100-l-w(-a, -n)	100	04/04 - 04/18	yes
100-s-w(-a, -n)	100	04/04 - 04/10	yes
100-s-n(-a, -n)	100	04/04 - 04/10	no

Table 4.1: Summary of the WRF-Chem simulations for the analysis of radiatively induced self-lifting. All simulations extended from April 4 until April 18, 2010. An abbreviation code is used for the simulations. The first entry in the code indicates the factor, the original FINN emissions have been scaled with. l or s (long or short) indicates if emissions were enabled over the entire simulation or if they were stopped after April 10. The entries n or w indicate, whether grid-resolved wet-scavenging was disabled or enabled. The additional letter -a, attached at the end, means absorbing simulations, while -n means non-absorbing simulations.

4.6 Analysis of radiatively induced self-lifting

A number of WRF-Chem simulations were made for the analysis of radiatively induced self-lifting. A list of the simulations, including an abbreviation code for each scenario, is given in Table 4.1. Every run extended from April 4 until April 18, 2010. At first, simulations were also made for the original FINN emissions. However, they were seen as an underestimation of the actual emissions based on a comparison to MODIS AOD measurements. No significant lifting was observed in those simulations due to the very low aerosol concentrations. Those simulations were not analysed any further.

The effects of radiation absorption by BC were extracted by two corresponding simulations with and without BC radiation absorption (Section 3.10.2). Different transport was found as a problem in the comparison of corresponding runs. Even though nudging made sure that the horizontal transport was similar, altitude differences that were caused by different vertical transport caused changes in horizontal transport. Thus, vertical profiles could only be compared for a few simulation steps.

4.6.1 Single plumes

Plume A

In this section, possible indications of self-lifting for plume A are discussed. For this, the maximum concentration within the plume was manually followed in time from the emissions and vertical profiles between the absorbing and the non-absorbing

simulations were compared.
No significant differences in plume altitude were found between the simulations 10-l-w-a and 10-l-w-n. The maximum column integrated AOD at 600 nm was low with values below 0.1 for both simulations, already 15 h after the emissions.
Nearly no differences in plume altitude were found for the simulations 50-l-w-a and 50-l-w-n, either. The emissions took place April 09, 23:00 UTC (17:00 LST). No strong self-lifting was expected until the next morning. 15 hours later (14:00 UTC, 08:00 LST), the AOD was 0.57 (50-l-w-a) and 0.52 (50-l-w-n), 21 hours later the AOD was 0.23 and 0.20, respectively. The SSA was 0.80 and 0.99, respectively.
A direct comparison to the study from Boers et al. (2010) was difficult because of the simplifications in their simulations (step-like vertical concentration profile, uniform heating throughout the entire plume, no aerosols above or below the plume). However, they suggested a self-lifting of 300 m per day for a plume with an average AOD of 0.4 and a SSA of 0.75 at 500 nm and 45° N during June 21 (Figure 2.4). The fires in this study burned in early April and the SSA was higher at a smaller wavelength. Thus, the lifting per 24 h would have been lower explaining, why no significant self-lifting was observed. Later in the simulation, the AOD was even lower.
Figure 4.33 shows the maxima of plume A for the simulations 100-l-w-a and 100-l-w-n during the first time-steps that were already presented in Figure 4.24. The temperature differences between the absorbing and the non-absorbing simulations are shown in Figure 4.34. The horizontal positions of the plume maxima deviated by a few grid-boxes in comparison to the weaker emission scenarios. This was expected because of the impact of the higher aerosol concentrations on the vertical propagation. The maximum AOD for the absorbing simulation during the emissions was between 2.23 and 4.11. The SSA was between 0.81 and 0.82 during the emissions and decreased to a minimum of 0.79 above ALOMAR. The SSA for the non-absorbing simulation was larger than 0.99 through the entire simulation.
The aerosol concentrations close to the ground above the fires were more than twice as high for simulation 100-l-w-a than for simulation 100-l-w-n (Figure 4.33 top left and centre panel). The temperature differences between the simulations 100-l-w-a and 100-l-w-n were negative close to the ground and positive above (Figure 4.34, top left and centre panel). It was concluded that the low temperatures at the ground led to a capturing of the aerosols directly above the fires in the absorbing simulation. The effect is discussed in more detail in the next section.
The column integrated AOD, 15 hours after the emissions (Figure 4.33, top right) was 1.21 and 1.38 for the simulations 100-l-w-a and 100-l-w-n, respectively. No altitude differences were observed, indicating no self-lifting. This was expected since the maximum concentrations at the fires were found 23:00 UTC (around 17:00 LST), leaving not much day-time for the aerosols to be heated by SW radiation. However, 21 hours later (Figure 4.33, second row, left) still, no differences in altitude were found between the absorbing and the non-absorbing simulations. The column integrated AOD was 0.52. A difference in maximum concentration suggested different transport that could have been connected to a self-lifting of the absorbing plume or to changes in the initial plume shape.
Small differences in altitude during later output steps were probably caused by small

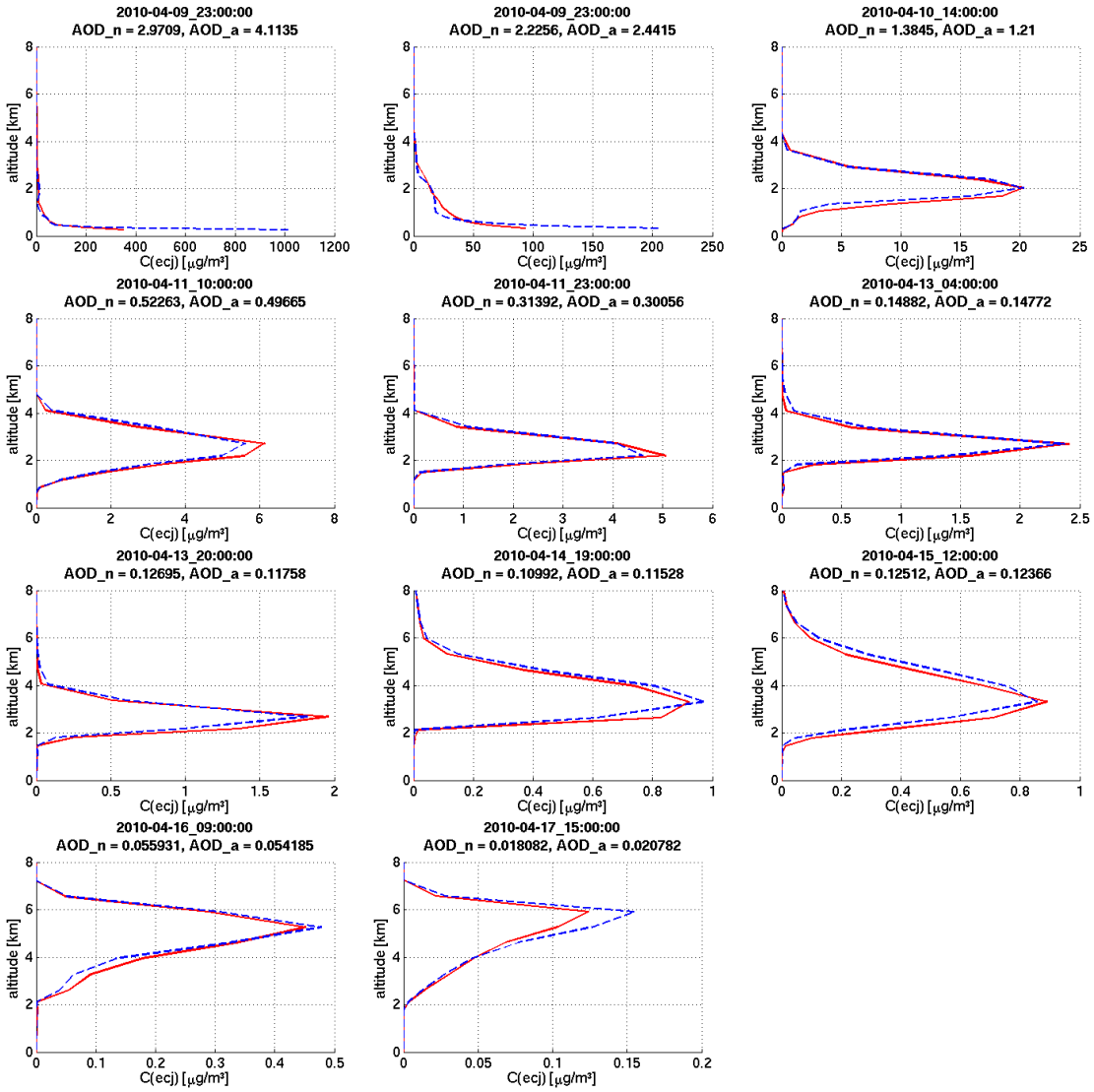

Figure 4.33: Vertical profiles of the WRF-Chem BC concentration for the 100-fold emission scenario at the maxima of plume A for the same time-steps as in Figure 4.24. Times are in UTC. The profiles for simulation 100-l-w-a are blue, the profiles for simulation 100-l-w-n are red. Two panels were added for the two strongest fires contributing to plume A at the time of the maximum concentrations at the emission sites (top left for fire 1 and top centre for fire 2).

differences in the plume shape or position. In Figure 4.33, bottom centre, it can be seen that already those minor changes in the plume shape or position caused higher aerosol concentrations above ALOMAR, as hypothesized in Section 4.4.1.
The differences in temperature suggested at least some warming through SW radiation. The differences were increasing through the first two days and maximum during April 11, 23:00 UTC (Figure 4.34, second row, centre panel). However, no self-lifting was caused by the temperature differences. This is discussed in more detail in the next section.
No evidence was found for radiatively induced self-lifting of plume A, making a val-

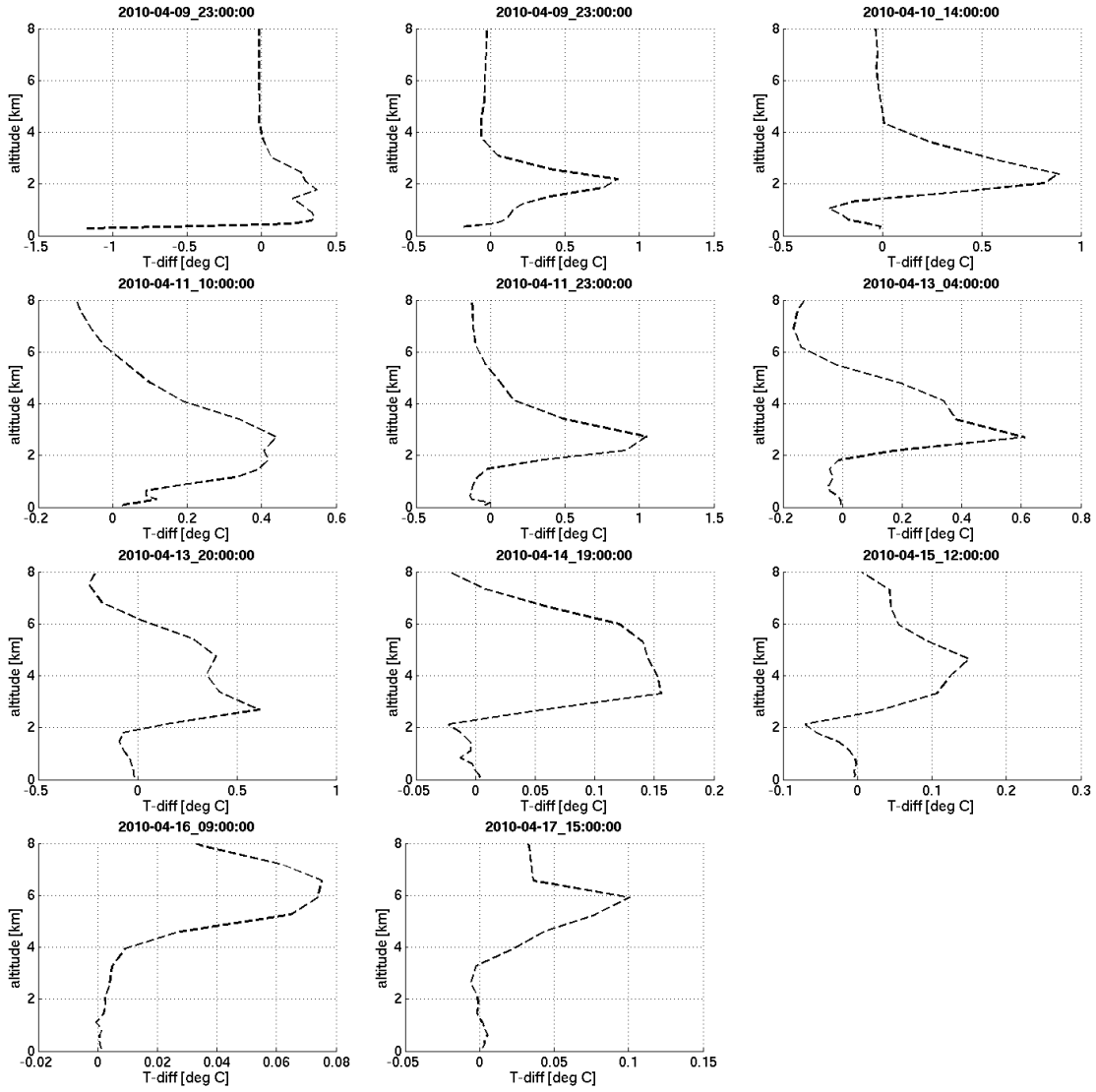

Figure 4.34: Vertical profiles of the temperature difference between the simulations 100-l-w-a and 100-l-w-n for the same output times and coordinates as in Figure 4.33. A positive temperature difference corresponds to warmer air in the simulation with enabled BC radiation absorption. Two panels were added for the time of the maximum concentrations at the emission sites (top left for fire 1 and top centre for fire 2).

idation of the vertical transport based on the LIDAR measurements impossible in the present study. A comparison to Boers et al. (2010) showed that at least some lifting could have occurred during the first day. Possible reasons, why no lifting was found, are discussed in the next section. Other than during the first day, the aerosol concentrations and therewith the AOD were too low to enable significant self-lifting. It was therefore decided to analyse the stronger Kansas fires that contributed to plume B regarding self-lifting.

The altitude difference between the model simulations and the LIDAR measurements that were first observed with HYSPLIT and reproduced in FLEXPART and WRF-Chem could not be explained by self-lifting.

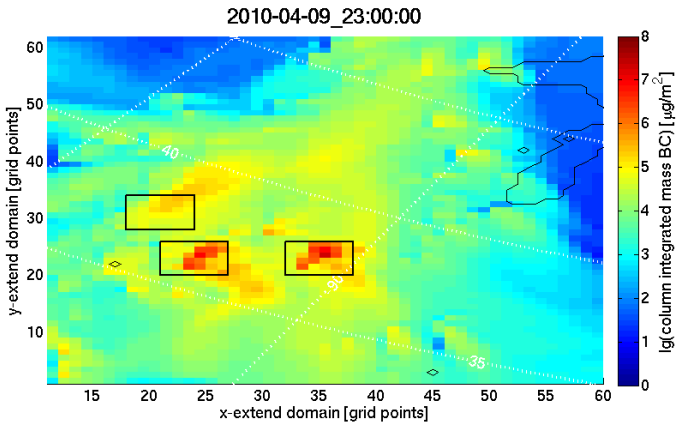

Figure 4.35: Column integrated total BC mass per m^2 during April 17, 2010, 23:00 UTC, when the maximum aerosol concentrations were found above the fires. Zoom over the main emission regions. The rectangles indicate the two strongest fires that contributed to plume B.

Plume B

As for plume A, the maximum concentration within plume B was manually followed in time. The strongest emission scenario was chosen for analysis since the strongest self-lifting was expected here.
Figure 4.35 shows a zoom over the fire emission region. The plumes from the strongest fires, which contributed to plume B, are marked with rectangles. Lake Superior and the plumes from the fires that contributed to plume A can be seen in the upper right. They were significantly weaker. The lower two rectangles show the strongest fires within the analysed time. Soon after the emissions, the plumes from those fires merged together to one very strong plume that had a significant contribution to plume B. However, horizontal transport was different between the absorbing and the non-absorbing simulations already within a few hours after the emissions. The plume in the upper rectangle showed more similar horizontal transport for the simulations 100-l-w-a and 100-l-w-n, at least for the first two days. Therefore, this plume was chosen for a direct comparison between the absorbing and the non-absorbing simulations.

Figure 4.36 shows a comparison of vertical profiles of the BC concentration, temperature and SW heating-rate between the simulations 100-l-w-a and 100-l-w-n. The vertical profiles at the point of maximum BC concentration in the upper rectangle (in Figure 4.35) are shown in the top panels. Model time was April 09, 23:00 UTC (coinciding with the maximum concentrations at the emission sites). Subsequent plots are shown for every six hours during the first two days.

During the emissions, the BC concentration in the lowest model layer was again higher for simulation 100-l-w-a than for simulation 100-l-w-n (left panel). The temperature in the lowest model layer was 0.2° C lower and was higher further up (second panel from the left) and the skin temperature (not shown) was 4.3° C lower. It was concluded that the additional absorption of SW radiation above the fires caused a reduction of the soil-temperature. The reduced soil-temperature led to a

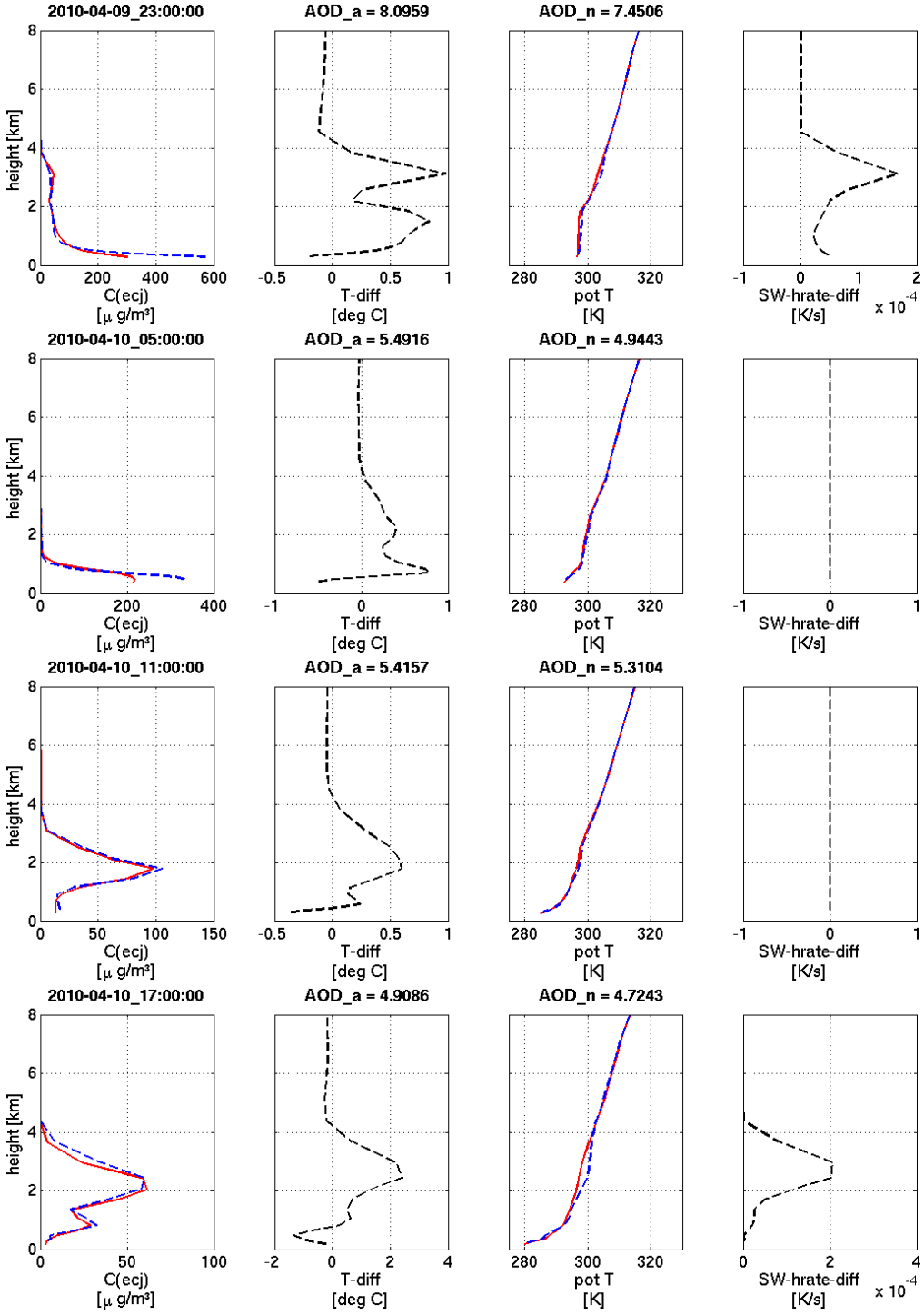

Figure 4.36: 6 -hourly comparison of vertical profiles between the simulations 100-l-w-a and 100-l-w-n for the aerosol plume that originated in the upper square in Figure 4.35, from April 9, 2010, 23:00 UTC - April 10, 2010, 17:00 UTC. Vertical profiles of differences are black, the profiles for simulation 100-l-w-a are blue and the profiles for simulation 100-l-w-n are red. Panels are, from left to right, the total BC concentration, the temperature difference, the potential temperature and the difference in SW radiative heating. The SW radiative heating is decoupled, meaning that it is calculated independent of nudging. It can be used as a direct indicator for day and night.

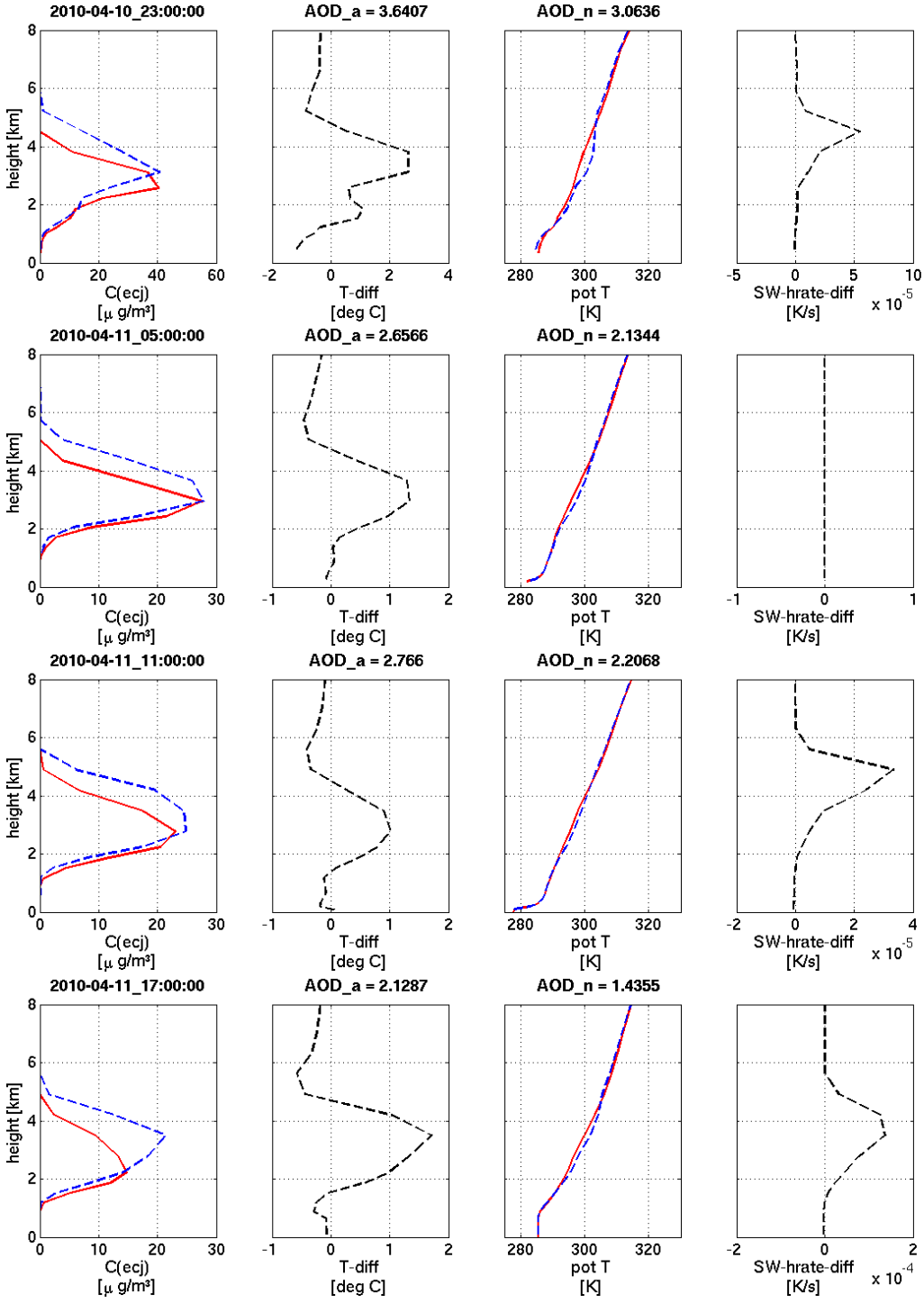

Figure 4.37: Same as Figure 4.36 from April 10, 2010, 23:00 UTC until April 11, 2010, 17:00 UTC

reduced warming of the lowest atmospheric layer and a reduction of turbulence and thus, transport out of the PBL. The higher temperatures further up were caused by SW heating of the aerosol layer. The lower temperature in the lowest atmospheric layer together with the higher temperature further up caused an increase in stability, leading to a lower release height of the aerosols.
The trapping of the aerosols at the ground created a feedback: The higher aerosol concentrations increased absorption and scattering of SW radiation. This additionally cooled the ground, leading to even more aerosols to be trapped directly above the fires.
However, the observed differences in concentration and temperature were not as large as for other, even weaker fires (Figure 4.33). It was concluded that this was caused by the relatively strong winds close to the ground at the fire location (Figure 4.20, top panel). Thus, the strength of the feedback was dependent on the wind velocities in the lowest atmospheric layers. This explained, why such strong differences were found at the fires in the lower two rectangles in Figure 4.35. The horizontal wind velocities were low.
Coming back to the aerosols from the upper rectangle in Figure 4.35. A temperature difference of 1°C was observed at an altitude around 3200 m during the emissions. This temperature difference was caused by SW radiation absorption in an elevated aerosol layer (Figure 4.36, top right panel). The elevated layer was weaker for simulation 100-l-w-a than for simulation 100-l-w-n, but in nearly the same altitude. This was in contradiction to the lower release height due to the ground cooling.
An indication that self-lifting might have been the reason for the unexpectedly high altitude of the elevated layer was found in the nearly neutral stability in the upper part of the plume (Figure 4.36, top, third panel from the left) and the negative temperature difference above the plume (Figure 4.36, top, second panel from the left). This was interpreted as a sign of self-lifting (the discussion for this is given below).
As before, no significant self-lifting was observed overnight until April 10, 11:00 UTC. (Figure 4.36, third row). During the next six hours, the temperature differences increased by more than a factor of three (Figure 4.36, last row). The AOD was 4.91 and 4.7 for the simulations 100-l-w-a and 100-l-w-n, respectively. The SSA was around 0.78 and 0.99 and remained nearly constant for the subsequent time-steps. Even though, the maximum temperature difference was already more than 2° C, nearly no lifting had occurred. This was in contradiction to the theoretical study from Boers et al. (2010). There, every temperature change was assumed to result in an altitude gain. The explanation for this contradiction was found in the potential temperature profile (Figure 4.36, fourth column).
Boers et al. (2010) assumed a step-like vertical profile of the aerosol concentrations and a constant energy deposition throughout the entire plume. Radiation absorption within this plume would have led to an instantaneous rising motion. However, instead of a step-like increase, real plumes follow a gradual increase in concentration. Hence, even a strong warming can occur in a stably stratified atmosphere, without triggering self-lifting, as long as no destabilisation of the air column is reached. The maximum temperature difference that can exist without showing any lifting depends on the vertical extent of the plume and the stability of the background air.

From the small altitude differences during April 10, 17:00 UTC (Figure 4.36, last row), together with the almost neutral temperature profile for the absorbing simulation, it was concluded that lifting must have been initiated from this point on.
The first significant difference in plume altitude that could be connected to self-lifting was found during April 10, 23:00 UTC (Figure 4.37, first row). The maximum temperature difference in comparison to the previous output step remained constant. The AOD was 3.64 and 3.06. The increase in difference in MWMA (Section 3.10.5), starting with a difference of only 15 m from April 10, 11:00 UTC was 458 m until April 10, 23:00 UTC, plus an increase in maximum temperature difference of 2.0° C. If the temperature change would have contributed entirely to a lifting of the plume, this would have corresponded to an altitude gain of around 765 m over 12 hours, assuming a lapse rate of 6.5 $\frac{K}{km}$.
Overnight, the difference in MWMA decreased by 40 m (Figure 4.37, third row) and increased again by 120.5 m during the next day (Figure 4.37, last row). The maximum temperature difference at that point was less than 2.0° C, instead of 2.5° C from 24 h earlier.
In the meantime, both plumes were diluted. The surrounding air that was mixed into the diluting plumes was not heated. Therefore, dilution decreased the temperature difference between the absorbing and the non-absorbing simulation, creating an additional resistance against self-lifting.
Judging from the differences in maximum BC concentration and the differences in plume shape in Figure 4.37 (bottom panel), the plumes had detached and a direct comparison was not possible anymore. During April 12, 05:00 UTC, the plume merged together with the plumes marked by the lower rectangles in Figure 4.35. The maximum altitude of maximum BC concentration that was reached by plume B stayed below 4 km, even though the AOD was greater than 1.5 until April 13, 08:00 UTC. It was not possible to draw conclusions on lifting through the comparison of the plume maxima anymore. It remained unknown, whether the constant altitude was caused by a lack of lifting or by other effects.
An additional pattern was found in the vertical profiles of the temperature differences. The differences were maximum around the altitude of maximum BC concentration, as expected due to the SW heating (last columns in Figures 4.36 and 4.37). Above the plume, the temperature differences were negative, just like in the lower parts of the plume and below the plume.
The differences in the SW heating rates were not negative in those regions. LW heating (not shown) was much weaker than SW heating and always of opposite sign from the temperature differences. Thus, the observed negative temperature differences were not explainable by radiative heating or cooling and must have been of dynamic origin. The cooling at the top could have been the result of the production of a convectively mixed layer, corresponding to the first type of lifting that was suggested by Herring and Hobbs (1994) (Section 2.3).
However, in a mixed layer, concentration gradients in altitude were expected to decrease with time. Therefore, the dilution of the plume at the top should have been larger for the absorbing simulation than for the non-absorbing one. This was not observed. Even though the vertical extend of the layer was higher for simulation 100-l-w-a than for simulation 100-l-w-n, no dilution was found. The increase in the

vertical extend of the layer could have been caused by small differences in transport and could therefore not be seen as an indicator of dilution.
The temperature difference below the plume could have been partially caused by lifting of the entire plume corresponding to the second type of lifting as suggested by [Herring and Hobbs (1994)]. However, this would only have accounted for a temperature decrease in a narrow layer below the plume, as seen in Figure 4.37 (bottom panel). The negative temperature difference all the way down to the ground, such as in Figure 4.37 (top panel), was not explainable by self-lifting.
Liu (2003) reported a reduction of heat transfer from the ground due to a cooling of the ground, competing against the absorption of solar radiation by the aerosols. The plume was placed in the lowest 3000 m of the atmosphere.
In this simulation, the layers were detached from the PBL within a day after the emissions so that no heating of the air close to the ground existed and the surface cooling was the dominating effect. The effect of the reduced heat transfer from the ground was removed for the last two rows in Figure 4.37, since the plume had moved over the ocean.
When lifting of the entire plume is discussed, it is necessary to consider the possible impact of aerodynamic resistance on the temperature differences and thus, the lifting potential. As already mentioned before, for self-lifting to occur, a temperature difference $> 0°$ C in comparison to the surrounding air had to be sustained over a longer time. This temperature difference was probably reduced through the dilution of the plume that was independent of the radiation absorption (compare the maximum concentrations of successive time-steps in Figures 4.36 and 4.37). The aerodynamic resistance could have reduced the lifting speed, increasing the temperature difference and the time, over which that difference had to be sustained. Hence, the reduction of the temperature difference through dilution could have been larger. The nudging of the horizontal velocities could have had a similar impact as the aerodynamic resistance, leading to a slower self-lifting.

4.6.2 Domain averaged effects

As already mentioned at the beginning of Section 4.6, vertical wind shears lead to a detaching of the transport between non-absorbing and absorbing simulations. After significant self-lifting had occurred, a direct comparison of single plume parts was not possible anymore. For domain-averaged effects, a direct comparison between overlying plumes is not necessary and therefore, the self-lifting can be analysed over a longer time. The domain averaged effects of radiation absorption on the vertical propagation and intactness of the plumes are presented here.

Mass weighted mean altitude

Figure 4.38 shows the differences in domain averaged MWMA (Section 3.10.5) of BC for the simulations 10-l-w-a - 10-l-w-n, 50-l-w-a - 50-l-w-n and 100-l-w-a - 100-l-w-n. Thresholds were introduced for the column integrated AOD. Grid-columns with

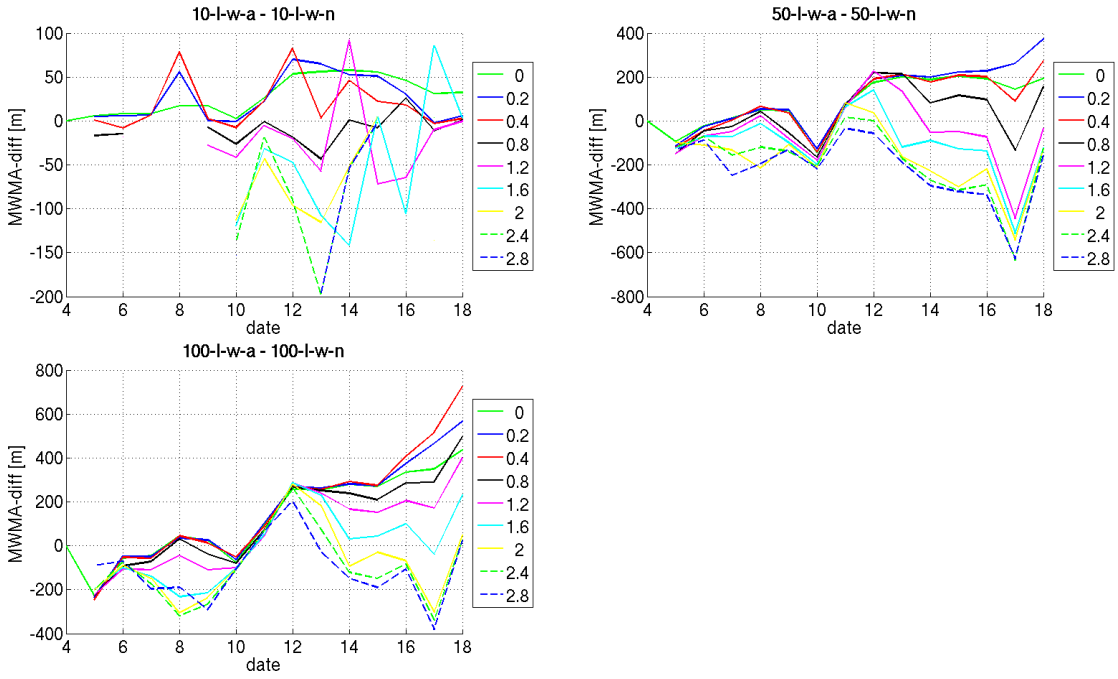

Figure 4.38: Differences in mass weighted mean altitude (Section 3.10.5) of all black carbon aerosols for the simulations 10-l-w-a - 10-l-w-n, 50-l-w-a - 50-l-w-n and 100-l-w-a - 100-l-w-n (long emissions, including wet-scavenging). Lower AOD thresholds are given in the legend. Grid-columns with AOD below the lower AOD thresholds were excluded from the calculation of the MWMA. The x-axis states the day of April 2010.
Missing line parts suggest that no column was found with AOD values higher than the respective threshold.

AODs lower than the thresholds were excluded from the calculation of the MWMA. This was done to get an estimation of the self-lifting in dependence on the plume strength (Section 3.10.5).

As before, the altitude differences between the simulations 10-l-w-a and 10-l-w-n remained small. No significant tendency was found that pointed towards self-lifting. Furthermore, the altitude differences for the highest AOD thresholds were mostly negative, indicating a higher mean altitude for the non-absorbing than for the absorbing simulations. Between the simulations 50-l-w-a - 50-l-w-n and 100-l-w-a - 100-l-w-n, the altitude differences increased towards the end of the simulations for the lowest thresholds, up to a maximum AOD threshold of 0.2 for the simulations 50-l-w-a - 50-l-w-n and 0.4 for the simulations 100-l-w-a - 100-l-w-n. With further increasing thresholds, the MWMA differences decreased towards negative values.
From the last section, where the plume maxima were followed, it was found that the absorption of SW heating in the air above the fires led to a cooling of the ground and the lowest atmospheric levels, causing a trapping of the aerosols close to the ground. For the domain-averaged MWMA, the lower release height and the self-lifting were competing. The highest AOD thresholds were mostly reached by recently emitted plumes, where the lower release height was still dominating. Even though the lower AOD thresholds also included those recently emitted plumes, the MWMA for the lowest thresholds was mostly dominated by older, more diluted plumes that had

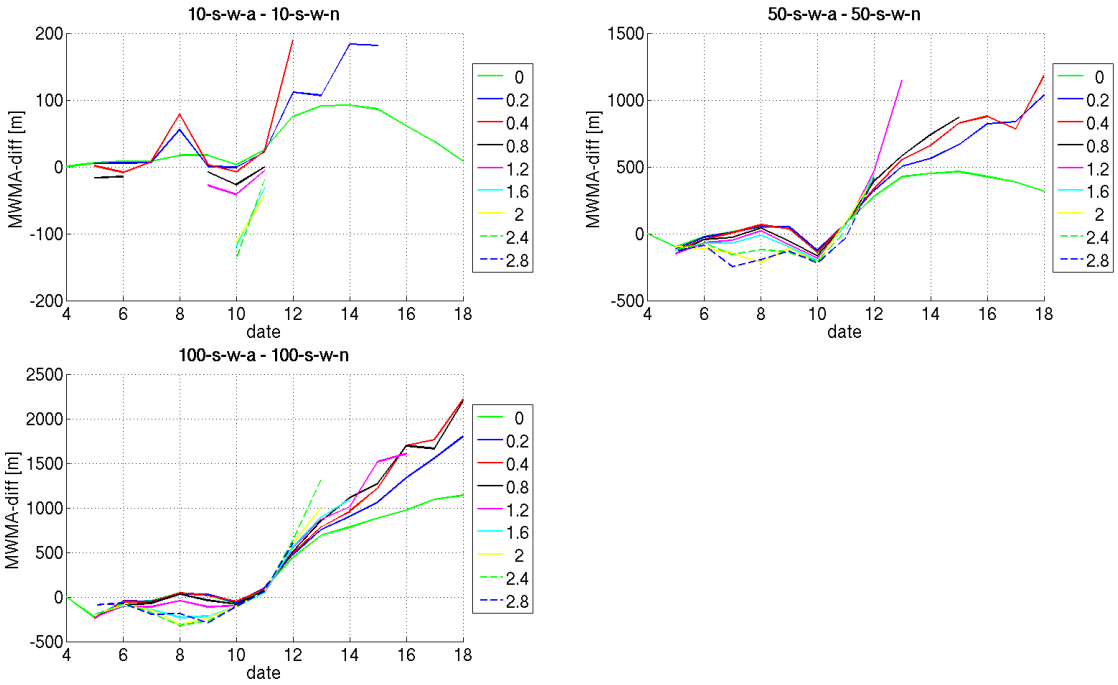

Figure 4.39: Same as Figure 4.38 for the simulations 10-s-w-a - 10-s-w-n, 50-s-w-a - 50-s-w-n and 100-s-w-a - 100-s-w-n (short emissions, including wet-scavenging).

time to lift.

To remove the effects directly at the fires, simulations were made with short emissions. The emissions were stopped after April 10, 2010, 23:00 UTC. The results for the same concentration thresholds as before are shown in Figure 4.39.

From April 11 (after the emissions were stopped), a clear tendency became visible in all three emission scenarios with a positive altitude difference between the absorbing and the non-absorbing simulations, pointing towards self-lifting. The differences were small for the emission scenario 10-s-w-a - 10-s-w-n and increased for the scenarios with stronger emissions. Within each emission scenario, altitude differences were increasing towards larger thresholds.

Dilution led to decreasing concentrations, resulting in an absence of grid-columns with AOD above the largest thresholds. This was especially evident for the emission scenario 10-s-w-a - 10-s-w-n. Even the very low AOD threshold of 0.2 was not reached anymore towards the end of the simulations. For the two stronger emission scenarios, the increase in MWMA was nearly monotonous after the emissions had been stopped.

Even though transport might still have played some role, with e.g. transport of aerosols over topography or out of the computational domain, the monotonous increase in MWMA difference, especially for the 100-fold emission scenario, was seen as a clear sign of self-lifting. The effect of a lower initial release altitude through ground-cooling was compensated quickly after the emissions were stopped.

However, the MWMA differences remained small in comparison to what was suggested by Boers et al. (2010). From their argumentation, a plume with an AOD of

2.0 should have experienced an altitude gain of around 1.25 km per 24 h (Figure 2.4). In the present study, an increase in MWMA difference of only 1.0 km was found for AODs larger than 2.0 from April 11 - 13, 00:00 UTC (Figure 4.39, bottom panel). A comparison to the purely theoretical study from Boers et al. (2010) was difficult, since the total column AOD was used as a measure for the plume optical thickness in this simulation. The plumes could have had a vertical extent of more than 3 km. That however, could have been compensated by the layer with the largest aerosol concentrations. As explained above, the value of 2.0 was the lower threshold. The stronger lifting of columns with higher AOD contributed to the increase in the MWMA differences for the lower thresholds, making the 1.0 km an overestimation of the self-lifting for a total column optical depth of 2.0.
On the other hand, Boers et al. (2010) assumed an undiluted plume with a uniform heating rate over the entire plume. As already discussed in Section 4.6.1, this led to an overestimation of self-lifting due to the step-like increase of the temperature differences. Furthermore, it was mentioned that inefficiencies in vertical transport could have been caused by aerodynamic resistance (Section 2.3). During the slow ascent, a dilution of the plume with horizontal or vertical entrainment of cooler air could have counteracted the SW heating, leading to an even slower vertical propagation. This effect could have been enhanced by the nudging of the horizontal winds that are essential for this type of lifting (Figure 2.6). To better understand the influence of nudging on self-lifting, a sensitivity study should be conducted. If nudging leads to a lower self-lifting rate of wildfire aerosols, this needs to be considered in future studies.
A breakup of plumes into smaller cells as suggested by Herring and Hobbs (1994) was not observed in the present study. They suggested a breakup of plumes with horizontal extent of several 1000 km into cells of few hundred kilometres. The plumes in this study were probably too small for that. It can be speculated that even smaller convective cells might be produced in large-scale plumes. It would be interesting to conduct an in-depth analysis of the importance of such dry convection on self-lifting with simulations with higher resolution.

Dry- and wet-deposition

For long-range transport, removal by dry-deposition and wet-scavenging is important. Together, both processes determine the atmospheric lifetime and therewith the transport efficiency of the aerosols. While dry-deposition is more important for aerosols within the PBL and is therefore an indirect measure of self-lifting (aerosols that are lifted away from the ground cannot be deposited at the same), wet-scavenging can have an impact on the thickness of elevated plumes that directly feeds back on the SW heating rate an thus, self-lifting.
It was found that the total rates of dry-deposition and grid-resolved wet-scavenging were of similar magnitude. The total rates of subgrid wet-scavenging were 100 times lower than for grid-resolved wet-scavenging (indicating that subgrid-scale cumulus precipitation was not important for the wet-removal of aerosols in the prevailing meteorological conditions) and are therefore not shown. No clear tendency existed

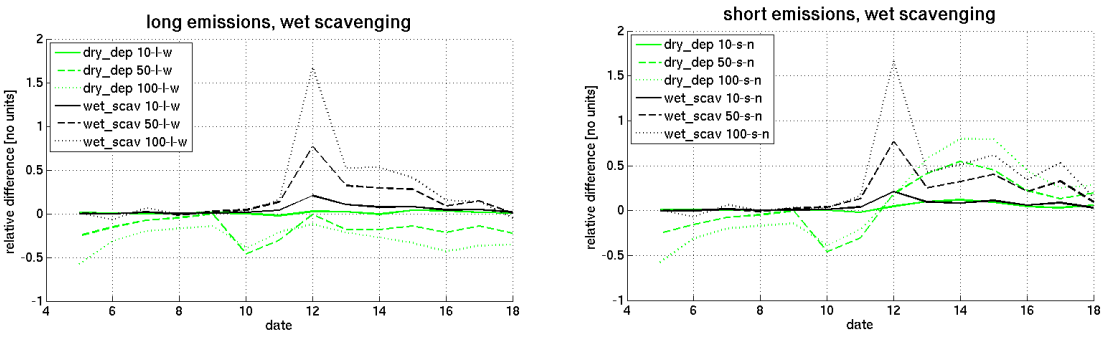

Figure 4.40: Left panel: relative difference ($\frac{\text{dep}_{\text{non-abs}} - \text{dep}_{\text{abs}}}{\text{dep}_{\text{abs}}}$) in grid-resolved wet-scavenging and dry-deposition between the simulations 10-l-w-a - 10-l-w-n, 50-l-w-a - 50-l-w-n and 100-l-w-a - 100-l-w-n (long emissions). Right panel: relative difference in grid-resolved wet-scavenging and dry-deposition for the simulations 10-s-w-a - 10-s-w-n, 50-s-w-a - 50-s-w-n and 100-s-w-a - 100-s-w-n (short emissions). Negative differences indicate a higher removal rate of aerosols by the respective mechanism in the absorbing simulations. The rates of grid-resolved wet-scavenging and dry deposition were in the same order. (The rates of subgrid-resolved wet-scavenging were 100 times lower. They showed no clear tendency an are not shown.)

for the difference between subgrid wet-scavenging for absorbing and non-absorbing simulations.

Relative differences in dry-deposition and grid-resolved wet-scavenging rates between absorbing and non-absorbing simulations for the full emissions are shown in Figure 4.40 (left-panel). The relative differences in grid-resolved wet-scavenging were always positive and increased with the emission strength until a maximum of 1.7. This means that at maximum almost double the mass of BC was removed by wet-scavenging in the non-absorbing simulation in comparison to the absorbing simulation. The differences in dry-deposition were mostly negative with a minimum for the strongest emission scenario, meaning that more aerosols were removed by dry deposition in the absorbing simulation.

Relative differences in dry-deposition and wet-scavenging rates between absorbing and non-absorbing simulations for the short emission scenario are shown in Figure 4.40 (right-panel). The relative differences in wet-deposition showed the same tendency as for the long emission scenarios. The relative differences in dry-deposition, however, were negative at first and became positive after the emissions had been stopped.

The negative relative differences in dry-deposition during emissions were most likely caused by the cooling of the ground at the emission sites. The positive relative differences in dry-deposition (after the emissions had been stopped) pointed towards a lifting of the aerosols away from the ground and a connected increase of total aerosol life-time and potential transport distances. The positive relative differences in wet-scavenging pointed either towards a reduction of rain through the semi-direct aerosol effect or towards a lifting of the aerosols above the clouds, where they could no longer be washed out. Either way, the reduction in wet-scavenging for the absorbing simulation pointed towards a longer life-time of plumes. This was

in contradiction to what was found by Westphal and Toon (1991) for fires that were also emitted in the Great Lakes region during July 1982.
A reduced self-lifting efficiency because of the coarse grid-resolution or nudging could have had an influence on the temperature within the plume, as it was discussed before. It would be interesting to analyse the impact of the setup of the simulations on the wet-scavenging efficiency and if the differences in wet-scavenging between an absorbing and a non-absorbing plume had any seasonal dependence.

Probability distribution functions

To estimate the potential importance of self-lifting on a longer time scale, its influence on the intactness of the plume is important. A highly diluted plume causes only small and gradual temperature changes, so that it is no longer lifted.
In this section, the intactness of the plumes over time is analysed through the differences in PDF of the BC concentrations between the absorbing and the non-absorbing simulations. The difference in PDF is an abstract construct. A detailed explanation is therefore given in Appendix D.
The differences in PDF between the simulations 10-l-w-a - 10-l-w-n, 50-l-w-a - 50-l-w-n and 100-l-w-a - 100-l-w-n are shown in Figure 4.41. The same is shown in Figure 4.42 and 4.43 for short emission scenarios and short emission scenarios with suppressed grid-resolved wet-scavenging, respectively.

A clear tendency towards increasing differences in PDF over time was observed at high concentrations for the full emission scenarios including wet-scavenging. The differences remained small between the simulations 10-l-w-a - 10-l-w-n (Figure 4.41, top left panel) and were larger between the simulations 50-l-w-a - 50-l-w-n and 100-l-w-a - 100-l-w-n (Figure 4.41, top right and bottom panel).
An increase of the differences in PDF at high concentrations over time generally pointed towards a stronger dilution of the plumes for the non-absorbing simulations. The strong increase of the differences in PDF at high concentrations for the full emission scenarios partially reflected the trapping of aerosols in the PBL. This effect was weak for the lowest emission scenario and increased with increasing emissions.
For the short emission scenarios, including wet-scavenging, the differences in PDF were small, for the 10-fold emission scenario (Figure 4.42, top left panel) and larger for the 50- and 100-fold emission scenarios (Figure 4.42, top right and bottom panel). The differences initially increased and remained nearly constant towards the end of the simulations. The initially increasing differences in PDF at the highest concentrations for the short emission scenarios partially reflects the trapping of the aerosols close to the ground at the fires. However, the continuing increase after April 10, 2010 illustrates that at least a part of the conservation of the plumes must have been independent of the trapping of the aerosols close to the ground.
So far the total effect of the radiation absorption was found to be a reduced depletion of the plumes for the absorbing simulations in comparison to the non-absorbing simulations. Absorbing plumes remained intact for a longer time, allowing for a longer self-lifting. This has an important implication for the long-range transport

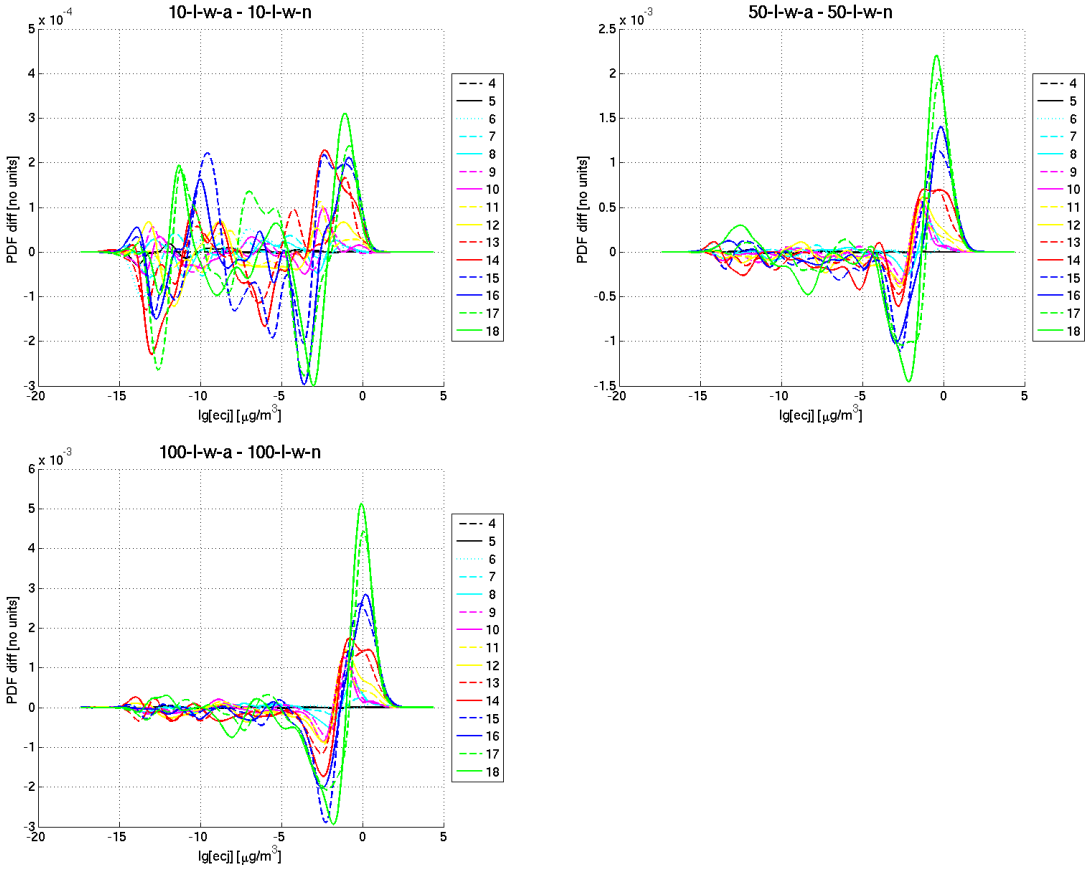

Figure 4.41: Difference in the probability distribution function ($\mathrm{pdf_{abs}} - \mathrm{pdf_{non\text{-}abs}}$) between the simulations 10-l-w-a - 10-l-w-n, 50-l-w-a - 50-l-w-n and 100-l-w-a - 100-l-w-n (long emissions, including wet-scavenging) for every simulation day, 00:00 UTC. The day of April, 2010 is given in the legend. The x-axis gives the decadic logarithm of the concentrations. The PDFs of both the absorbing and the non-absorbing simulations are normalized. Thus, differences in PDF are zero in average and show differences in the relative occurrence of the concentrations.

of wildfire aerosols.

This effect might have at least partially been caused by the reduced wet-scavenging rates that were described in the last section. A reduction in wet-scavenging could keep the plumes intact for a longer time. To assess the importance of wet-scavenging on the intactness of solar heated wildfire aerosol plumes and to analyse the effect of the self-lifting itself, the differences in PDF for the short emission scenarios with suppressed grid-resolved wet-scavenging are shown in Figure 4.43.

The tendency of growing differences in PDF at high concentrations over time did not exist anymore. For the 50-fold emission scenario (Figure 4.43, top panels), a pattern with a small but increasingly positive difference in PDF at the highest concentrations ($\geq 10^0 \ \frac{\mu g}{m^3}$) was observed. For the concentrations between $10^{-2} \ \frac{\mu g}{m^3}$ and $10^0 \ \frac{\mu g}{m^3}$, the differences were increasingly negative over time. The same tendency was observed for the 10-fold emission scenario (Figure 4.43, top left panel), but the differences were weaker. For the 100-fold emission scenario (Figure 4.43, bottom

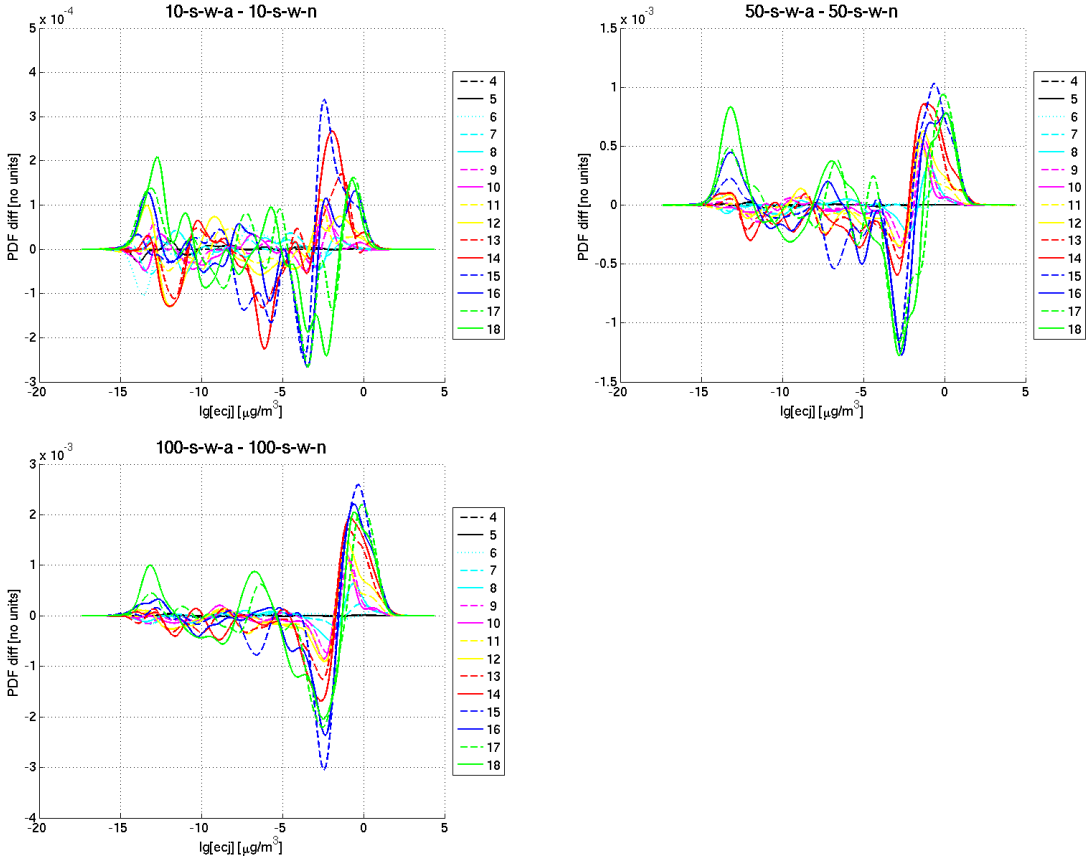

Figure 4.42: Same as Figure 4.41 for simulations 10-s-w-a - 10-s-w-n, 50-s-w-a - 50-s-w-n and 100-s-w-a - 100-s-w-n (short emissions, including wet-scavenging).

panel), a similar tendency was observed during the last three simulation days. For April 13, 14 and 15, however, increasing differences in PDF were found at the highest aerosol concentrations. This was not reproduced in any of the other emission scenarios and might have been connected to transport of aerosols out of the computational domain.

The tendency of decreasing differences in PDF for concentrations between 10^{-2} $\frac{\mu g}{m^3}$ and 10^{0} $\frac{\mu g}{m^3}$ could have been caused by a dilution in the upper part of the plumes by a convectively mixed layer (Section 2.3.2). Since the differences in PDF were not negative at the highest concentrations, it can be concluded that the mixed layer did not extend down to the plume maxima. Thus, the regions of maximum concentrations must have been lifted without additional dilution, pointing towards a lifting of the plume as a whole.

The small increase in differences in PDF for the highest concentrations could have been caused by a shielding of the plume maxima from turbulence from below the layer due to the strong stabilisation of the air in the lower parts of the plumes (compare to Figures 4.36 and 4.37).

The stable increase in differences in PDF for the short simulations with wet-scavenging in comparison to the short simulations with suppressed grid-resolved wet-scavenging shows that the reduction of wet-scavenging had a positive effect on the intactness of

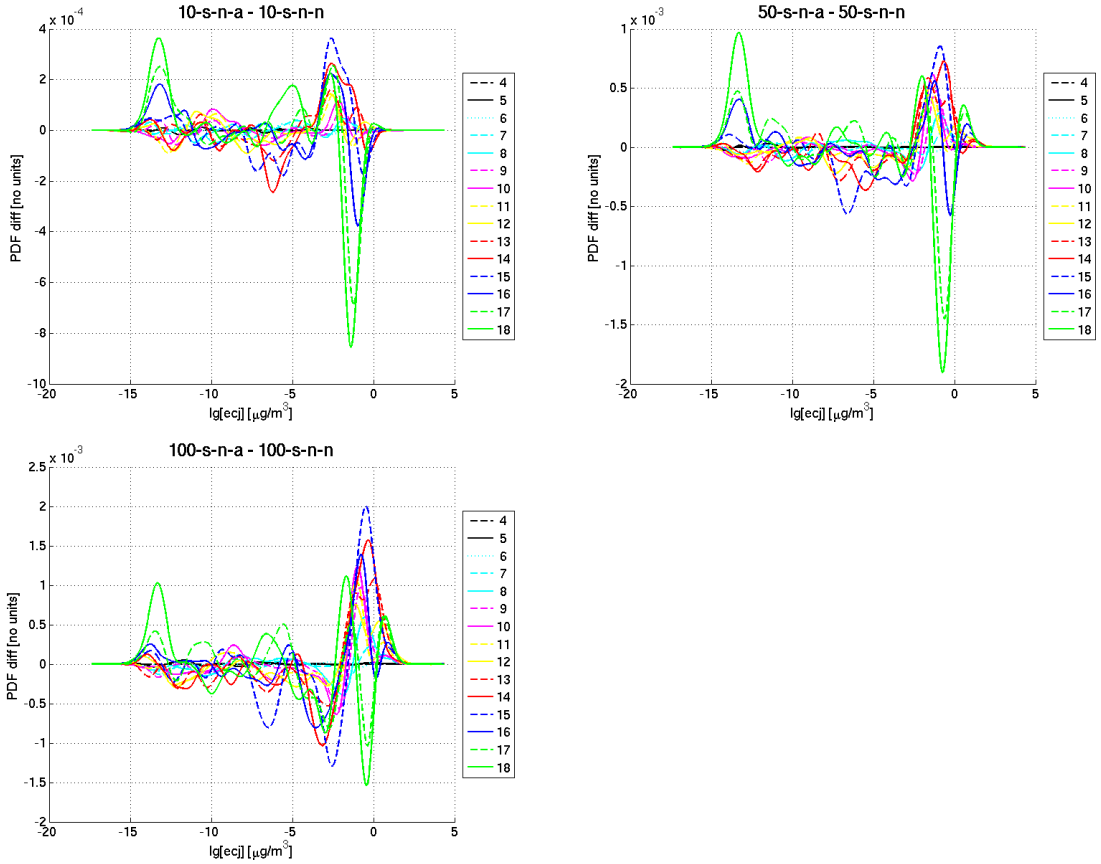

Figure 4.43: Same as Figure 4.41 for simulations 10-s-n-a - 10-s-n-n, 50-s-n-a - 50-s-n-n and 100-s-n-a - 100-s-n-n (short emissions, with disabled wet-scavenging).

the plumes. The effects of subgrid wet-scavenging remain unknown but are assumed to be small.

It was hypothesized before that nudging could have resulted in a slower self-lifting. This would have resulted in larger temperature differences between the absorbing and the non-absorbing simulations and thus, a stronger suppression of wet-scavenging. It would be interesting to assess the importance of the nudging on the self-lifting rates and on the differences in wet-scavenging.

Transport out of the computational domain might have played a role. However, the influence of that on the overall conclusions is expected to be small, since the conclusions were based on stable tendencies that could not have been caused by irregularly occurring transport out of the computational domain.

Chapter 5

Summary and Conclusions

5.1 Summary

The main objectives of this study were: (1) the identification of wildfire aerosol layers in the ALOMAR troposphere LIDAR data from 2010 and 2011 and (2) the analysis of the importance of radiatively induced self-lifting on transport towards the Arctic.
ALOMAR troposphere LIDAR data were analysed for the period from April - September 2010 and 2011. Layers of increased LIDAR signal were separated into potential wildfire aerosol layers and cloud or other pollution layers. For 2011, the volume depolarisation could be used to sort out highly depolarising signals, such as clouds or volcanic ash. This was not possible on a regular basis for 2010. To confirm the conclusions on the layers in 2011 and as basis for the rejection of layers in 2011, auxiliary data were used: SYNOP data, radio-soundings, HYSPLIT simulations and MODIS RRI wildfire detections.
The layers that were selected as potential wildfire aerosol layers were further analysed. FLEXPART backwards simulations were done to find the source regions of the potential aerosol layers. Those regions were compared to MODIS wildfire detections. Two events showing a clear LIDAR signal and a good overlap between wildfires and the simulated source region were identified. The aerosols from both events originated from North American fires. Due to a lack of time to do an in-depth analysis for both transport events, it was decided to choose only one for analysis with WRF-Chem. The event from April 17, 2010 had a stronger LIDAR signal and the transport simulations showed an overlap with higher fire activity than for the other event. The event from April 17, 2010 was therefore chosen for further analysis. It caused a strong and even layer between 6000 and 6700 m from 15:42 - 16:50 UTC. The FLEXPART backwards simulations showed a good overlap with high fire activity west of Lake Superior during April 09, 2010 and the LIDAR signal was the strongest of all aerosol layers in 2010 and 2011.
Transport analysis of the atmospheric column surrounding the aerosol layer above ALOMAR with FLEXPART and HYSPLIT indicated that the simulations placed the aerosol layer around 300 - 400 m lower than the LIDAR measurements suggested.

It was hypothesised that this misplacement could have been caused by self-lifting which was not covered in the offline transport models. However, this hypothesis could not be confirmed with the WRF-Chem simulations. The transport event from April 17, 2010 coincided temporally with the eruption of the Eyjafjallajökull volcano. However, a contribution to the aerosol layer above ALOMAR from the volcano was ruled out on the basis of the low particle depolarisation ratio of 2.1%, which is an indicator for mostly spherical particles (volcanic ash is highly non-spherical with a particle depolarisation ratio of more than 30%), and the transport simulations.
WRF-Chem simulations confirmed a wildfire aerosol layer above ALOMAR. Only wildfire emissions were included into the simulation. The emissions were specified with the help of NCAR's FINN fire emission inventory tool. The relatively isolated layer was followed manually backwards in time through the WRF-Chem output; black carbon was used as a tracer. The source region was in accordance with the source region from the FLEXPART simulations, even though there were uncertainties due to the approach of manually following the layer. The LIDAR measurements suggested a layer 300 - 400 m higher. During the transport, the plume that was transported towards ALOMAR merged with a stronger plume from wildfires in Kansas. Even though both plumes were transported together for two days, the FLEXPART simulations suggested that nearly none of the aerosols which were found above ALOMAR originated from Kansas. During the further transport, the plume underwent splitting over Iceland and lifting over the Norwegian See. It was finally protracted strongly before reaching ALOMAR during April 17, 2010.
The simulated aerosol concentrations over ALOMAR were very low with about $1.2 \cdot 10^{-2}\ \frac{\mu g}{m^3}$. It was unlikely that such a weak aerosol layer could be detected with a LIDAR. Therefore, it was decided to compare the simulated plume strengths to satellite measurements with the help of the AOD.
The simulated AOD was compared to measurements twice: over North America during April 10, 2010, the day after the emissions, and over ALOMAR during April 17, 2010. The analysis of the AOD directly at the emission site was underestimated by the simulations. An increase of the emissions by a factor of 10 showed a better agreement with the AOD which was measured with the MODIS instrument. However, even the 10-fold increased emissions led to an underestimation of the AOD above ALOMAR in comparison to a measurements with the sun-photometer. A simulation with emissions increased by a factor of 100 still underestimated the AOD by roughly a factor of two after the background of a clear day was subtracted. The underestimation of the AOD above ALOMAR by a factor of 200 could partially be explained by pollution of the PBL and by the underestimation of the emissions, as confirmed with the AOD measurements during the day after the emissions. However, an underestimation of the AOD above ALOMAR by a factor of 10 remained. It was concluded that the aerosol transport was too inefficient. Possible sources for this could have been a minor misplacement of the wind-fields after the emissions, a wrong timing of the emissions by a few hours or the splitting and protracting of the plume, during which only a weak fraction of the plume was transported towards ALOMAR.
Because of the low aerosol concentrations, no self-lifting was observed in the plume fraction that was transported towards ALOMAR, even in the simulation with 100-

fold increased emissions. The altitude differences between the model simulations and the LIDAR measurement were not explainable by self-lifting.
The comparison between the simulation with radiation absorption from black carbon and without showed temperature differences of maximum 1°C. However, they were too small to cause a destabilisation of the atmosphere that is necessary for self-lifting
Self-lifting has been found in the stronger plume from the Kansas fires. As for the plume that was transported towards ALOMAR, the plume maximum was followed manually in time and simulations with and without radiation absorption from black carbon were compared. Two mechanisms were found to influence the vertical propagation of an absorbing plume. The first mechanism was a cooling of the ground because of the additional extinction of SW radiation in the plume. This led to a lower release height of the aerosols and a trapping of the aerosols close to the ground directly above the fires. The second mechanism was self-lifting through SW radiation absorption.
However, the observed self-lifting rates were lower than suggested by Boers et al. (2010) in a theoretical study. The reason might have been non-instantaneous self-lifting that was suggested by Boers et al. (2010). Through the gradual decrease of aerosol concentrations towards greater heights at the top of the plume, the air column was not destabilised until a temperature difference of more than 2°C was reached. However, the temperature differences were continuously reduced through the dilution of the plumes with surrounding air that has not been warmed by SW radiation. In addition, it was hypothesised that the lifting of the plume as a whole reduced the lifting rates through the aerodynamic resistance against the lifting of a large layer. That, together with the dilution of the plumes could have slowed down the self-lifting even more. This was also concluded to be the reason, why no lifting was found for the plume that was transported towards ALOMAR. The cooling through the dilution might have happened at a faster rate than the warming through SW absorption. Finally, it was considered, that grid-nudging or the low resolution of the simulations might have had a negative influence on the self-lifting in the simulations.
However, different horizontal transport led to a detaching of the plumes from the absorbing and the non-absorbing simulations after self-lifting had happened. Therefore, it was decided to analyse domain-averaged differences. that were less affected by this.
The differences in mean altitude were analysed in dependence on lower thresholds for the AOD. The differences in mean altitude between the absorbing and the non-absorbing simulations were affected by the two factors: cooling of the ground and self-lifting. The cooling of the ground led to a lower mean altitude for grid-columns with high AOD thresholds in the absorbing simulations. Thus, simulations were done with emissions ending after April 10, 2010. After the emissions had been stopped, the mean altitude of the absorbing simulations increased in comparison to the mean altitude of the non-absorbing simulations. The maximum difference of roughly 2300 m, 8 days after the emissions had been stopped, was found for the lower AOD thresholds of 0.4 and 0.8 for the 100-fold increased emissions, showing a clear sign of self-lifting. The maximum mean altitude differences for the 10-fold

increased emission scenario stayed below 200 m.
The domain averaged wet-scavenging was lower for the absorbing simulations. It was concluded that the temperature difference that was necessary for the self-lifting reduced the precipitation rates. Dry deposition was higher in the absorbing simulations as long as emissions took place, because of the trapping of a large amount of aerosols close to the ground. However, it was lower after the emissions were stopped, indicating a lifting of the aerosols away from the ground.
Finally, the intactness of the plumes was analysed on the basis of differences in the probability distribution of black carbon. The trapping of the aerosols led to a more frequent occurrence of high concentrations in the absorbing simulations than in the non-absorbing simulations. The same effect was caused by the reduced wet-scavenging in the absorbing simulations. When both effects were removed, it was found that the concentrations corresponding to either weak plumes or the edges of strong plumes occurred less often. This was concluded to be connected to the appearance of convectively mixed layers at the plume tops. The occurrence of concentrations corresponding to the centres of strong plumes was not reduced, it was rather slightly elevated in the absorbing simulations, indicating that the centres of the plumes were not influenced by the convectively mixed layer and might have been shielded from turbulence from below the plumes.

5.2 Final conclusions and future work

- Two events of clear wildfire aerosol layers above ALOMAR were identified. The aerosols of both events originated from North America according to FLEXPART calculations. The layer showing the strongest LIDAR signal and a high overlap between strong fire activity and the source region during April 17, 2010 was chosen for an in-depth analysis.
- The importance of self-lifting has been assessed with the help of WRF-Chem. It was found that a temperature difference of more than 2°C was necessary for rapid self-lifting to occur. Therefore, it was concluded that self-lifting only plays a role for concentrated plumes. When the aerosol concentrations in a plume were too low, the dilution during normal transport reduced the temperature differences that were caused by SW radiation absorption and inhibited self-lifting.
- Radiation absorption had a second effect on the vertical propagation of the wildfire aerosols: The additional extinction of SW radiation in the atmosphere caused a cooling of the ground at the fires, leading to a trapping of aerosols close to the ground.
- Wet-scavenging was reduced in the absorbing simulations because of the warming of the surrounding air and the connected reduction of the relative humidity. Subgrid-scale wet-scavenging connected to convective clouds was significantly lower than grid-resolved wet-scavenging. It was concluded that cumulus-convection was not important for the wet-removal of aerosols in the prevailing

meteorological conditions. The reduction of wet-scavenging was in contradiction to Westphal and Toon (1991), who also analysed fires in the Great Lakes region. That poses the question if the influence of the radiation absorption on wet-scavenging has any regional or seasonal dependence.

- The overall effect of radiation absorption was an increased intactness of the elevated plumes. This was partially connected to the reduced wet-scavenging rate. When wet-scavenging was disabled, the concentrations corresponding to weak plumes or the plume edges occurred less often in the absorbing simulations, indicating dilution in a convectively mixed layer. The highest concentrations ($> 10^0 \ \frac{\mu g}{m^3}$ of BC), corresponding to the plume centres occurred more often. Even though the differences were small at those concentrations, it was concluded that the plume centres might have been shielded from turbulence from below by the strong temperature inversion at the bottom of the plume that was caused by the radiation absorption.

- To draw conclusions on the importance of radiation absorption on the vertical propagation of wildfire aerosols, it was necessary to compare simulations with and without radiation absorption. Different horizontal transport led to a detaching of the absorbing and the non-absorbing plumes, making a direct comparison between the absorbing and the non-absorbing simulations impossible after self-lifting had occurred. A study with idealised conditions, i.e. without background winds, could provide a useful tool to better understand the basic processes connected to self-lifting. The experiences from such a study could be transferred into future analyses of self-lifting in real-data simulations.

- The identification of wildfire aerosols mostly based on transport simulations is somewhat vague. Other sources (e.g. anthropogenic emissions) could not be ruled out. This can lead to high uncertainties. A full LIDAR inversion algorithm would be useful to reach a higher degree of certainty for the source specification. However, for a safe identification of wildfire aerosols, in-situ measurements are necessary. In addition, the use of a method not explicitly treating self-lifting (backwards simulations) could have led to a faulty rejection of wildfire aerosol layers in connection with diverging horizontal transport.

- The analysis of only one case study has limited outreach and should be confirmed with more studies under different meteorological conditions. To analyse the general importance of radiation absorption on the vertical propagation of wildfire aerosols and e.g. to be able to draw conclusions on offline simulations not explicitly treating this effect, an analysis of a large number of wildfire aerosol cases is necessary. This can e.g. be done using data from several LIDARs or data from airplane-campaigns.

- It was hypothesized that a coarse resolution and nudging could have reduced the rates of self-lifting. A sensitivity study in a smaller domain, where nudging is less crucial for stable results, can be useful to analyse those effects. Information on the dependence of self-lifting on the resolution and nudging would be important for future simulations of aerosol transport.

References

Achard, F., H. Eva, D. Mollicone, and R. Beuchle (2008). The effect of climate anomalies and human ignition factor on wildfires in Russian boreal forests. *Philosophical Transactions of the Royal Society B: Biological Sciences 363*(1501), 2329–2337.

Ackermann, I., H. Hass, M. Memmesheimer, A. Ebel, F. Binkowski, and U. Shankar (1998). Modal aerosol dynamics model for Europe: development and first applications. *Atmospheric Environment 32*(17), 2981 – 2999.

ALOMAR (2012). ALOMAR webpage. url: http://alomar.rocketrange.no/ (February 21, 2012).

Amiridis, V., D. Balis, E. Giannakaki, A. Stohl, S. Kazadzis, M. Koukouli, and P. Zanis (2009). Optical characteristics of biomass burning aerosols over Southeastern Europe determined from UV-Raman lidar measurements. *Atmospheric Chemistry and Physics 9*(7), 2431–2440.

Ansmann, A., M. Tesche, S. Groß, V. Freudenthaler, P. Seifert, A. Hiebsch, J. Schmidt, U. Wandinger, I. Mattis, D. Müller, and M. Wiegner (2010). The 16 April 2010 major volcanic ash plume over central Europe: EARLINET lidar and AERONET photometer observations at Leipzig and Munich, Germany. *Geophysical Research Letters 37*(13), L13810.

Ansmann, A., U. Wandinger, M. Riebesell, C. Weitkamp, and W. Michaelis (1992). Independent measurement of extinction and backscatter profiles in cirrus clouds by using a combined raman elastic-backscatter lidar. *Applied Optics 31*(33), 7113–7113.

Bates, D. (1984). Rayleigh scattering by air. *Planetary and Space Science 32*(6), 785 – 790.

Behrendt, A. and T. Nakamura (2002). Calculation of the calibration constant of polarization lidar and its dependency on atmospheric temperature. *Optics Express 10*(16), 805–817.

Boers, R., A. deLaat, D. S. Zweers, and R. Dirksen (2010). Lifting potential of solar-heated aerosol layers. *Geophysical Research Letters 37*(24), L24802.

Cooper, O. R., C. Forster, D. Parrish, M. Trainer, E. Dunlea, T. Ryerson, G. Hübler, F. Fehsenfeld, D. Nicks, J. Holloway, J. de Gouw, C. Warneke, J. Roberts, F. Flocke, and J. Moody (2004). A case study of transpacific warm conveyor

belt transport: Influence of merging airstreams on trace gas import to North America. *Journal of Geophysical Research 109*(D23), D23S08.

deLaat, A., D. S. Zweers, R. Boers, and O. Tuinder (2012). A solar escalator: Observational evidence of the self-lifting of smoke and aerosols by absorption of solar radiation in the February 2009 Australian Black Saturday plume. *Journal of Geophysical Research 117*(D4).

Eva, H. and E. Lambin (1998). Remote sensing of biomass burning in Tropical regions: sampling issues and multisensor approach. *Remote Sensing of Environment 64*(3), 292 – 315.

Fast, J., J. Barnard, E. Chapman, R. Easter, S. Ghan, W. G. Jr., R. Z. G. Grell, S. Peckham, and S. McKeen (2010). Aerosol-radiation-microphysics interactions: aerosol direct and indirect forcing. WRF-Chem Tutorial, August 2, 2010, Boulder CO.

Fernald, F. (1984). Analysis of atmospheric lidar observations: some comments. *Applied Optics 23*(5), 652–653.

Fiebig, M., A. Stohl, M. Wendisch, S. Eckhardt, and A. Petzold (2003). Dependence of solar radiative forcing of forest fire aerosol on ageing and state of mixture. *Atmospheric Chemistry and Physics 3*(3), 881–891.

Fiedler, J., G. Baumgarten, and G. von Cossart (2003). Noctilucent clouds above ALOMAR between 1997 and 2001: Occurrence and properties. *Journal of Geophysical Research 108*(D8), 8453.

Forster, C., U. Wandinger, G. Wotawa, P. James, I. Mattis, D. Althausen, P. Simmonds, S. O'Doherty, S. Jennings, C. Kleefeld, J. Schneider, T. Trickl, S. Kreipl, H. Jäger, and A. Stohl (2001). Transport of boreal forest fire emissions from Canada to Europe. *Journal of Geophysical Research 106*(D19).

Forster, P., V. Ramaswamy, P. Artaxo, T. Berntsen, R. Betts, D. Fahey, J. Haywood, J. Lean, D. Lowe, G. Myhre, J. Nganga, R. Prinn, G. Raga, M. Schulz, and R. V. Dorland (2007). Changes in atmospheric constituents and in radiative forcing. *Climate Change 2007: The Physical Science Basis. Contribution of Working Group I to the Fourth Assessment Report of the Intergovernmental Panel on Climate Change*, 129–234.

Freitas, S., K. Longo, R. Chatfield, D. Latham, M. S. Dias, M. Andreae, E. Prins, J. Santos, R. Gielow, and J. C. Jr (2007). Including the sub-grid scale plume rise of vegetation fires in low resolution atmospheric transport models. *Atmospheric Chemistry and Physics 7*(13), 3385–3398.

Freudenthaler, V., M. Esselborn, M. Wiegner, B. Heese, M. Tesche, A. Ansmann, D. Mueller, D. Althausen, M. Wirth, A. Fix, G. Ehret, P. Knippertz, c. Toledano, J. Gasteiger, M. Garhammer, and M. Seefeldner (2009). Depolarization ratio profiling at several wavelengths in pure Saharan dust during SAMUM 2006. *Tellus B 61*(1), 165–179.

Frioud, M., M. Gausa, G. Baumgarten, J. Kristjansson, and I. Føre (2006). New tropospheric lidar system in operation at ALOMAR (69°N, 16°E). pp. 179–182. Reviewed and Revised Papers of the 23rd International Laser Radar Conference.

Fromm, M. and R. Servranckx (2012). Transport of forest fire smoke above the tropopause by supercell convection. *Geophysical Research Letters 30*(10).

Gausa, M. (2011). Personal correspondence.

Ghan, S. (1989a). Unstable radiative-dynamical interactions. part i. basic theory. *Journal of the Atmospheric Sciences 46*(16), 2528–2543.

Ghan, S. (1989b). Unstable radiative-dynamical interactions. part ii: Expanded theory. *Journal of the Atmospheric Sciences 46*(16), 2544–2561.

Giglio, L. (2010). MODIS collection 5 active fire product user's guide version 2.4.

Giglio, L., J. Descloitres, C. Justice, and Y. Kaufman (2003). An enhanced contextual fire detection algorithm for MODIS. *Remote Sensing of Environment 87*(2-3), 273 – 282.

Giglio, L., J. Randerson, G. van der Werf, P. Kasibhatla, G. Collatz, D. Morton, and R. DeFries (2010). Assessing variability and long-term trends in burned area by merging multiple satellite fire products. *Biogeosciences 7*(3), 1171–1186.

Giglio, L., G. van der Werf, J. Randerson, G. Collatz, and P. Kasibhatla (2006). Global estimation of burned area using MODIS active fire observations. *Atmospheric Chemistry and Physics 6*(4), 957–974.

Gillett, N., A. Weaver, F. Zwiers, and M. Flannigan (2004). Detecting the effect of climate change on Canadian forest fires. *Geophysical Research Letters 31*(18), L18211.

Grell, G. (2012). Personal correspondence.

Grell, G., S. Peckham, R. Schmitz, S. McKeen, G. Frost, W. Skamarock, and B. Eder (2005). Fully coupled online chemistry within the WRF model. *Atmospheric Environment 39*(37), 6957 – 6975.

Guan, Z. (2011). Personal correspondence.

Hadley, O. and T. Kirchstetter (2011). Black-carbon reduction of snow albedo. *Nature Climate Change 2*(6), 437–440.

Hamamatsu (2012). How do I choose between a PMT, APD, or Photodiode for my application? url: http://sales.hamamatsu.com/en/support/faq/product-faqs/technical-questions-about-products.php?goto=13198815 (March 02, 2012).

Hedin, A. (1987). MSIS-86 thermospheric model. *Journal of Geophysical Research 92*(A5), 4649–4662.

Hedin, A. (1991). Extension of the MSIS thermosphere model into the middle and lower atmosphere. *Journal of Geophysical Research 96*(A2), 1159–1172.

Herring, J. and P. Hobbs (1994). Radiatively driven dynamics of the plume from 1991 Kuwait oil fires. *Journal of Geophysical Research 99*(D9), 4333–4351.

Hodnebrog, Ø., F. Stordal, and T. Berntsen (2011). Does the resolution of megacity emissions impact large scale ozone? *Atmospheric Environment 45*(38), 6852 – 6862.

Jacobson, M. (2001). Strong radiative heating due to the mixing state of black carbon in atmospheric aerosols. *Nature 409*(6821), 695 – 697.

Janhäll, S., M. Andreae, and U. Pöschl. (2010). Biomass burning aerosol emissions from vegetation fires: particle number and mass emission factors and size distributions. *Atmospheric Chemistry and Physics 10*(3), 1427–1439.

Keil, A. and J. Haywood (2003). Solar radiative forcing by biomass burning aerosol particles during SAFARI 2000: A case study based on measured aerosol and cloud properties. *Journal of Geophysical Research 108*(D13).

Koelbl, C. (2010). Depolarization of LIDAR signals in the Arctic atmosphere. University of Constance, Germany, Department of Physics, Bachelor thesis.

Licel (2011). Analog + photon counting. url: www.licel.com/analogpc.pdf (May 09, 2012).

Licel (2012). The Licel home page. url: http://www.licel.com/ (March 02, 2012).

Lilly, D. (1988). Cirrus outflow dynamics. *Journal of the Atmospheric Sciences 45*(10), 1594–1605.

Liou, K. (2002). *An introduction to atmospheric radiation* (2 ed.), Volume 84 of *International Geophysics Series*. Elsevier.

Liu, Y. (2003). Atmospheric response and feedback to smoke radiative forcing from wildland fires. pp. 1–4. Second international wildland fire ecology and fire management congress and fifth symposium on fire and forest meteorology.

Malone, R., L. Auer, G. G. M. Wood, and O. Toon (1986). Nuclear winter: Three-dimensional simulations including interactive transport, scavenging, and solar heating of smoke. *Journal of Geophysical Research 91*(D1), 1039–1053.

Manney, G., M. Santee, M. Rex, N. Livesey, M. Pittis, P. Veefkind, E. Nash, I. Wohltmann, R. Lehmann, L. Froidevaux, L. Poole, R.Schoeber, D. Haffner, J. Davies, V. Dorokhov, H. Gernandt, B. Johnson, R. Kivi, E. Kyroe, N. Larsen, P. Levelt, A. Makshtas, C. McElroy, H. Nakajima, M. Parrondo, D. Tarasick, P. v.d. Gathen, K. Walker, and N. Z. et al. (2011). Unprecedented Arctic ozone loss in 2011. *Nature 478*(7370), 469–475.

Mattis, I., D. Mueller, A. Ansmann, U. Wandinger, T. Murayama, and R. Damoah (2004). Siberian forest-fire smoke observed over central Europe in spring/summer 2003 in the framework of Earlinet. pp. 857. 22nd internation laser radar conference.

Mundomanz (2012). Current synop data including translation. url: http://www.mundomanz.com/meteo_p/main (February 29, 2012).

Murayama, T., D. Müller, K. Wada, A. Shimizu, M. Sekiguchi, and T. Tsukamoto (2004). Characterization of asian dust and siberian smoke with multi-wavelength raman lidar over tokyo, japan in spring 2003. *Applied Optics 31*(23).

NASA (2012a). AERONET web page. url: http://aeronet.gsfc.nasa.gov/new_web/index.html (April 25, 2012).

NASA (2012b). Giovanni - The bridge between data and science. url: http://disc.sci.gsfc.nasa.gov/giovanni/overview/index.html (April 30, 2012).

NASA (2012c). MODIS overview. Land Processes Distributed Active Archive Center.

NASA (2012d). MSIS-E-90 atmosphere model. url: http://omniweb.gsfc.nasa.gov/vitmo/msis_vitmo.html (February 02, 2012).

NASA (2012e). NASA Rapide Response Imagery. url: http://rapidfire.sci.gsfc.nasa.gov/cgi-bin/imagery/firemaps.cgi (January 12, 2012).

NCEP (2012). Weather maps NCEP. url: http://www.hpc.ncep.noaa.gov/dailywxmap/index_20100409.html (July 07, 2012).

NOAA (2012a). Main page Air Resource Laboratory. url: http://www.arl.noaa.gov/ (February 02, 2012).

NOAA (2012b). Real-time environmental applications and display system, Air Resource Laboratory, National Oceanic and Atmospheric Administration. url: http://ready.arl.noaa.gov/ (February 02, 2012).

NOAA (2012c). Real-time environmental applications and display system, Air Resource Laboratory, National Oceanic and Atmospheric Administration. url: http://ready.arl.noaa.gov/gdas1.php (February 02, 2012).

Noel, V. and K. Sassen (2005). Study of planar ice crystal orientations in ice clouds from scanning polarization lidar observations. *Journal of Applied Meteorology 44*(5), 653–664.

Prenni, A., P. DeMott, A. Sullivan, R. Sullivan, S. Kreidenweis, and D. Rogers (2012). Biomass burning as a potential source for atmospheric ice nuclei: Western wildfires and prescribed burns. *Geophysical Research Letters*.

Radtke, L., J. Lyons, P. Hobbs, and R. Weiss (1990). Smokes from the burning of aviation fuel and their self-lofting by solar heating. *Journal of Geophysical Research 95*(D9), 14071–14076.

Reid, J., T. Eck, S. Christopher, R. Koppmann, O. Dubovik, D. Eleuteri, B. Holben, E. Reid, and J. Zhang (2005). A review of biomass burning emissions part III:

intensive optical properties of biomass burning particles. *Atmospheric Chemistry and Physics 5*(3), 827–849.

Remer, L., Y. Kaufman, D. Tanre, S. Mattoo, D. Chu, J. Martins, R. Li, C. Ichoku, R. Levy, R. Kleidman, T. Eck, E. Vermote, and B. Holben (2005). The MODIS aerosol algorithm, products, and validation. *Journal of the Atmospheric Sciences 62*(4), 947–973.

Rogers, R. and M. Yau (1988). *A short course in cloud physics* (3 ed.). Elsevier.

Rudich, Y., A. Sagi, and D. Rosenfeld (2003). Influence of the Kuwait oil fires plume (1991) on the microphysical development of clouds. *Journal of Geophysical Research 108*(D15), 4478–4485.

Sakaeda, N., R. Wood, and P. Rasch (2011). Direct and semidirect aerosol effects of southern African biomass burning aerosol. *Journal of Geophysical Research 116*(D12), D12205.

Schell, B., I. Ackermann, H. Hass, F. Binkowski, and A. Ebel (2001). Modeling the formation of secondary organic aerosol within a comprehensive air quality model system. *Journal of Geophysical Research 106*(D22), 28275–28293.

Seibert, P. and A. Frank (2004). Source-receptor matrix calculation with a Lagrangian particle dispersion model in backward mode. *Atmospheric Chemistry and Physics 4*(1), 51–63.

Seinfeld, J. and S. Pandis (2006). *Atmospheric chemistry and physics: from air pollution to climate change* (2 ed.). Wiley.

Sessions, W., H. Fuelberg, R. Kahn, and D. Winker (2010). An investigation of methods for injecting emissions from boreal wildfires using WRF-Chem during ARCTAS. *Atmospheric Chemistry and Physics Discussions 10*(11), 26551–26606.

Skamarock, W., J. Klemp, J. Dudhia, D. Gill, D. Barker, M. Duda, X. Huang, W. Jordan, and G. Powers (2008). A Description of the Advanced Research WRF Version 3. Technical Note.

Stenchikov, G., M. Fromm, and A. Robock (2006). Regional simulations of stratospheric lofting of smoke plumes. *AGU Fall Meeting Abstracts*, A5.

Stohl, A. (2012). Personal correspondence.

Stohl, A., E. Andrews, J. Burkhart, C. Foster, A. Herber, S. Hoch, D. Kowal, C. Lunder, T. Mettford, J. Ogren, S. Sharma, N. Spichtinger, K. Stebel, R. Stone, J. Stroem, K. Tørseth, C. Wehrli, and K. Yttri (2006). Pan-Arctic enhancements of light absorbing aerosol concentrations due to North American boreal forest fires during. *Journal of Geophysical Research 111*(D22214).

Stohl, A., T. Berg, J. Burkhart, A. Fjaeraa, C. Forster, A. Herber, O. Hov, C. Lunder, W. McMillan, S. Oltmans, M. Shiobara, D. Simpson, S. Solberg, K. Stebel, J. Strom, K. Torseth, R. Treffeisen, K. Virkkunen, and K. Yttri (2007). Arctic smoke - record high air pollution levels in the European Arctic due to agricultural

fires in Eastern Europe in spring 2006. *Atmospheric Chemistry And Physics 7*, 511–534.

Stohl, A., J. Burkhart, D. Hirdman, and H. Sodemann (2007). An integrated internet-based system for analyzing the influence of emission sources and atmospheric transport on measured concentrations of trace gases and aerosol. url: http://transport.nilu.no/flexpart/web_based_tool.pdf (March 15, 2012).

Stohl, A., C. Forster, S. Eckhardt, N. Spichtinger, H. Huntrieser, J. Heland, H. Schlager, S. Wilhelm, F. Arnold, and O. Cooper (2003). A backward modeling study of intercontinental pollution transport using aircraft measurements. *Journal of Geophysical Research 108*(D12), 4370–4387.

Stohl, A., C. Forster, A. Frank, P. Seibert, and G. Wotawa (2005). Technical note: The Lagrangian particle dispersion model FLEXPART version 6.2. *Atmospheric Chemistry and Physics 5*(9), 2461–2474.

Stohl, A., A. Prata, S. Eckhardt, L. Clarisse, A. Durant, S. Henne, N. Kristiansen, A. Minikin, U. Schumann, P. Seibert, K. Stebel, H. Thomas, T. Thorsteinsson, K. Toerseth, and B. Weinzierl (2011). Determination of time- and height-resolved volcanic ash emissions and their use for quantitative ash dispersion modeling: the 2010 Eyjafjallajöekull eruption. *Atmospheric Chemistry and Physics 11*(9), 4333–4351.

Stohl, A., H. Sodemann, S. Eckhardt, A. Frank, P. Seibert, and G. Wotawa (2011). The Lagrangian particle dispersion model FLEXPART version 8.2. FLEXPART user guide, url: http://zardoz.nilu.no/ flexpart/flexpart/flexpart82.pdf (March 14, 2012).

Toledano, C. (2012). Personal correspondence.

Trentmann, J., M. Andreae, H. Graf, P. Hobbs, R. Ottmar, and T. Trautmann (2002). Simulation of a biomass-burning plume: Comparison of model results with observations. *Journal of Geophysical Research 107*(D2), 4013.

Twomey, S. (2007). Pollution and the planetary albedo. *Atmospheric Environment 41*(0), 7120 – 125.

UMBC (2012). U.S. air quality archives. url: http://alg.umbc.edu/usaq/archives/2010_04.html (May 05, 2012).

University of Maryland (2012). University of Maryland ftp server, MODIS CMG products. url: fuoco.geog.umd.edu, name: fire, password: brunt, path: modis/C5/cmg/8day/hdf (Dezember 12, 2011).

University of Wyoming (2012). Radiosonde archive. url: http://weather.uwyo.edu/upperair/sounding.html (February 02, 2012).

Valor, B. (2012). OGIMET. url: http://www.ogimet.com/synops.phtml.en (February 29, 2012).

Weather, U. (2012). Unisys weather information systems. url:

http://weather.unisys.com/wxp/Appendices/Formats/SYNOP.html (February 29, 2012).

Westerling, A., H. Hidalgo, D. Cayan, and T. Swetnam (2006). Warming and earlier spring increase western U.S. forest wildfire activity. *Science 313*(5789), 940–943.

Westphal, D. and O. Toon (1991). Simulations of microphysical, radiative, and dynamical processes in a continental-scale forest fire smoke plume. *96*(D12), 22379–22400.

Wiedinmyer, C., S. Akagi, R. Yokelson, L. Emmons, J. Al-Saadi, J. Orlando, and A. Soja (2010). The Fire INventory from NCAR (FINN) - a high resolution global model to estimate the emissions from open burning. *Geoscientific Model Development Discussions 3*(4), 2439–2476.

Appendix A

LIDAR

A.1 LIDAR schematic and specifications

Transmission			
Laser type	seeded ND:YAG Quanta Ray GCR 6-30		
Wavelengths	355, 532, 1064 nm		
Pulse energies (typical)	180, 180, 520 mJ		
Repetition rate	30 Hz		
Beam full divergence	60 - 210 μrad		
Reception			
Channel	**Interference filter characteristics**		
	CW [nm]	BW [nm]	Transm [%]
1064 nm	1064.6	0.2	>50
532 nm p	532.3	0.35	>50
532 nm s	532.3	0.35	>50
355 nm	354.8	0.2	>30
387 nm (N_2 Raman)	386.8	0.2	>50
608 nm (N_2 Raman)	407.6	0.2	>50
Acquisition			
Transient recorder:	LICEL TR 20-160		
Analogue mode			
A/D resolution	12 bits (4096 quantisation levels)		
Raw resolution	7.5 m		
Photo counting mode			
Max count rate	250 MHz		
Discriminator	64 quantisation levels		

Table A.1: Specifications of the ALOMAR troposphere LIDAR. The 532 nm channel is split into p (parallel) and s (perpendicular) polarised light. CW and BW indicate the centre wavelength and the bandwidth, respectively [Frioud et al. (2006)].

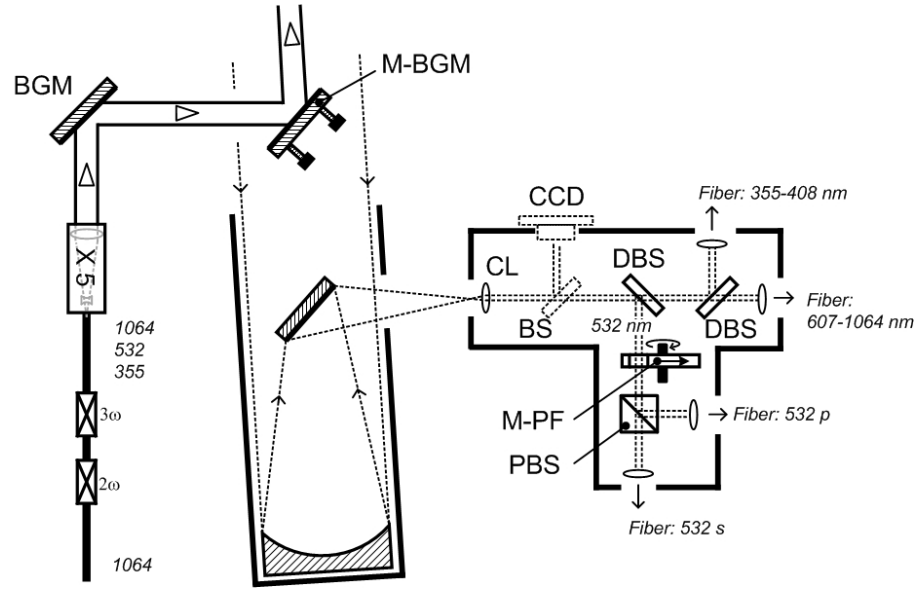

(a)

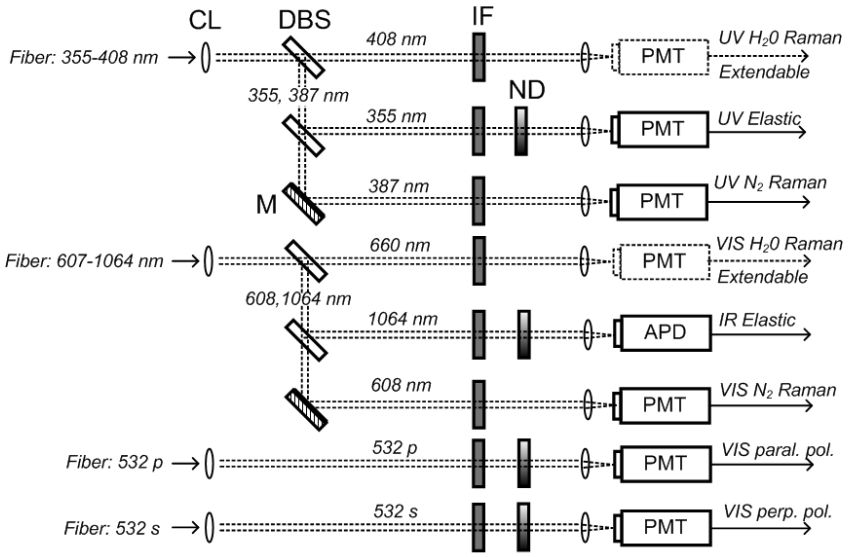

(b)

Figure A.1: Schematic of the laser and the focal box (a) and the detection boxes (b).The laser is tilted to reduce the strong reflectance from horizontally aligned ice particles.

A.2 Description of the LIDAR components

A.2.1 Transmission unit

The transmission unit consists of the laser, a refractive beam-widening telescope and beam guiding mirrors.
The laser is a neodymium-doped yttrium aluminium garnet laser. The three output wavelengths are the original (1064 nm) wavelength and the second (532 nm) and third (355 nm) harmonic frequencies. The laser system was a donation from IAP and was used in the RMR LIDAR system at ALOMAR. Due to its high power, together with narrow-banded filters, the LIDAR is suitable for daylight conditions and extends its range up into the lower to middle stratosphere. A detailed description of ND:YAG lasers and harmonics generation is beyond the scope of this work and can be found in text books on laser physics.
The beam widening telescope is a refractive Galileo type telescope, expanding the beam thickness by 5 times. It reduces the laser divergence to less than 210 μrad.
The first beam guiding mirror reflects the beam from the laser room to the telescope hall. The second beam guiding mirror aligns the laser beam coaxial to the receiving telescope. The common axis is tilted three degrees out of zenith to reduce the strong reflectance from horizontally aligned ice crystals as they can occur in cirrus clouds [Noel and Sassen (2005)].

A.2.2 Reception unit

The reception unit consists of the telescope, the focal box and the optical components of the detection boxes.
The telescope is a Newtonian type with a parabolic primary mirror (diameter 18.6 cm, focal length 125 cm). Like the laser system, the main mirror was a donation from IAP.
In the focal box, the light first hits a collimator lens, reducing the LIDARS effective focal length to 60 cm. After that, the light passes a first **D**icroic **B**eam **S**plitter (DBS) that extracts the 532 nm wavelength light. With a second DBS, the light is then split into the two wavelength bands of 355-408 nm and 607-1064 nm. The two outer wavelength bands are coupled into fibres and guided into the two first detection boxes. The 532 nm wavelength band is transmitted through a **P**olarizing **B**eam **S**plitter cube (PBS), where it is separated into its s- and p-polarised components. Before the light is lead through the PBS, it passes a **M**otorized **P**olarisation **F**ilter (MPF) (a linear polarisation filter, with a hole in one position that is fixed on a rotating plate with a stepper-motor). During depolarisation calibration, which has been installed in 2010 and is discussed in Subsection A.4, the MPF is rotated stepwise by a total of 180°, allowing the light to be linearly polarised at different angles relative to the PBS polarisation angles. During normal detection mode, the MPF is rotated to a position, where the light is transmitted through the hole and therefore has no influence on the measurements. After having passed the PBS, the

two 532 nm wavelength signals are coupled into optic fibres and guided into two separate detection boxes.
In the detection box, the two outer wavelength bands are again split by DBSs. The wavelength band 355-408 nm is split into wavelength bands around 355 and 387 nm. The wavelength band 607-1064 nm is split into the two wavelength bands around 1064 and 608 nm. The 355 nm, 1064 nm and 532 nm bands are sent through **N**eutral **D**ensity filter (ND) to control the intensity reaching the **P**hoto **M**ultiplier **T**ubes (PMTs). Between the DBS and the detectors, all wavelength bands are transmitted through **I**nterference **F**ilters (IF) to reach a small **B**and**W**idth (BW) around their **C**enter **W**avelength (CW). The filters are chosen as narrow as possible to ensure the daylight usability of the LIDAR.

A.2.3 Acquisition unit

The acquisition unit consists of the detectors, the multiple channel discretizers and the acquisition computer.
After the signals have passed the reception unit, they are detected by PMTs with exception of the 1064 nm signal that is detected by an **A**valanche **P**hoto **D**iode (APD).
The detection principle of a PMT is based on Einstein's photoelectric effect, after which each photon causes one electron to be emitted when hitting a negatively charged photo-cathode. The kinetic energy of the electrons is only dependent on the photons wavelength. On the other hand, the number of emitted electrons is dependent on the intensity of the incident light (i.e. the number of in-falling photons). The electrons accelerate on a cascade of dynodes leading to a signal gain of around 10^6.
The 1064 nm signal is still too strong for the PMTs. Therefore, an APD is used. An APD is a semiconductor detector with a gain factor of around $50-100$ [Hamamatsu (2012)]. Its function is also based on the photoelectric effect. However, instead of multiplying the photons by a cascade of dynodes, the multiplication in an APD is reached within a semiconductor. When the voltage applied to the APD is high enough, electrons accelerate strongly. On their way, they will 'knock' other electrons free, leading to an avalanche of electrons that is travelling towards the positive voltage that accelerated them in the first place.
After leaving the PMTs and APD, the signal is detected by a multiple-channel transient digitizer in analogue and photon counting mode. In the analogue mode, the current from the in-falling photons is detected and discretised. This detection method is linear for relatively strong signals, but has the disadvantage of electronic noise. Therefore, the signal from the PMTs is detected in photo counting mode as well. Here, the signal of each single photon is enhanced to a voltage peak with constant height. This detection method is applicable for very weak signals and is less sensitive to noise, since faulty peaks can easily be identified through their wrong height.
However, detection in photo counting mode experiences a dead-time. Each pulse

from the detection of a photon has a finite length. If the intensity of the in-falling light is high, it is possible that two electrons enter the detector at a too short time interval so that they appear as one pulse. That causes the detection efficiency to decrease. A dead-time correction, based on the probability that two electrons enter the detector at a too close range, solves that problem to a certain degree. However, with further increasing signal strength, the detection efficiency decreases too much and detection is not linear any more. A combination of both detection methods can significantly increase the LIDAR's dynamic range.
The APD's performance in the photon counting mode is low. Thus, the 1064 nm signal is only used in analogue mode. A closer description of the acquisition unit can be found in Licel (2012).
After detection and discretisation (i.e. digitalisation), the signals are averaged over 70 s to reduce noise and stored by the acquisition PC.

A.3 Filter design for LIDAR data evaluation

The filter was chosen to reduce high frequency noise in the height resolved signals while simultaneously keeping the vertical dispersion as low as possible. Figure A.2 shows the impact of the filter on a step function. In a distance of 5 bins from the step, corresponding to a distance in height of 45 m, the filter produces only an error of 0.04. In a distance of 15 bins, corresponding to a distance in height of 135 m, the impact of the filter has faded. Doubling the iterations, the error at 5 bins distance increases to 0.12 and the fadeout distance becomes 30 bins. For most cases, 5 iterations have been sufficient to improve the signal to noise ratio, while keeping the diffusive peak broadening at a minimum.

A.4 LIDAR signal calibration

The calibration of the p- and s- polarised channels for the cases in 2010 was based on the known Rayleigh depolarisation ratio within the stratosphere and utilized regular measurement data. For the cases in 2011, a separate calibration procedure was done before using the LIDAR. Both methods are discussed below.

A.4.1 Calibration on the basis of the Rayleigh signal

The calibration method for 2010 was based on the method from Behrendt and Nakamura (2002). They calculated the depolarisation ratio for pure Rayleigh scattering to be 0.0036 and a temperature dependent error between 200 K and 280 K air temperature of almost as low as 0.2% for the interference filters that were used at ALOMAR. Under the assumption of an aerosol-free stratosphere, the s- polarised signal could be

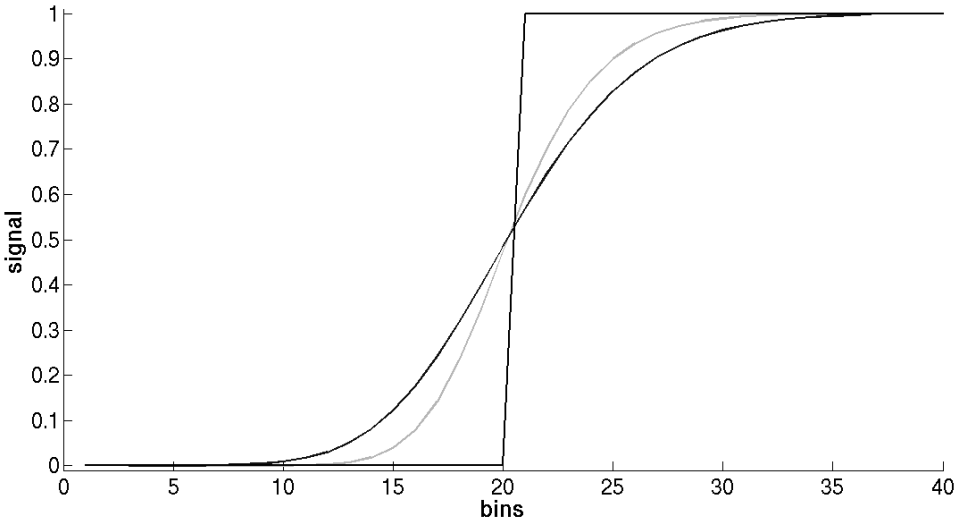

Figure A.2: The impact of the averaging filter on a step function (black, step) after 5 (grey) and 10 (black, curved) iterations. The error after 5 iterations in a distance of 5 bins from the step is 0.04. The error has faded out entirely after 15 bins.

calibrated relative to the p-polarised signal using the Rayleigh signal in an altitude around 12 km with

$$R_1 = \frac{0.0036}{\frac{\bar{P}_r(r)_s}{\bar{P}_r(r)_P}} \tag{A.1}$$

and

$$\bar{P'}_s(r) = \bar{P}_s(r) \cdot R_1, \tag{A.2}$$

whereby $\bar{P}_r(r)$ and $\bar{P}_s(r)$ were the dead-time corrected and range corrected signals. As already mentioned above, the method was based on the assumption of pure Rayleigh scattering within the stratosphere. However, even the stratosphere is never entirely aerosol free. That could lead to high uncertainties in connection with this calibration method. Nevertheless, the LIDAR calibration method based on an aerosol free part of the atmosphere has been used for a long time and is still in use today, even though the method is being more and more replaced by separate calibration methods like the one that is described below.

A.5 Calibration routine based on the MPF

In 2010, the LIDAR was equipped with the MPF (Subsection A.2). From 2011 on, the new calibration method has been used on a routine basis before doing measurements with the LIDAR system. For this, the MPF is rotated stepwise from -90° to +90°. The procedure is equivalent for both the analogue and photon counting channels. At every step, the intensity is averaged over 80 - 100 shots. The resulting intensity is fitted with an $a \cdot \cos^2(\theta + \theta_0)$ curve, according to Malus' law. The variable a displays the ratio in detector gain and θ_0 is the constant angle between

the laser linear polarisation and the PBS. θ_0 was mostly found within a range from -3° to +3°. For the calibration of the channels, only the ratio for the detector gain a was used:

$$\bar{P'}_s(r) = \bar{P}_r(r) \cdot a. \tag{A.3}$$

The VDR was further calibrated by taking into account a constant angle between the laser linear polarisation and the PBS:

$$VDR = \frac{\frac{\bar{P'}_s(r)}{\bar{P'}_p(r)} - \sin^2(\beta)}{1 - \frac{\bar{P'}_s(r)}{\bar{P'}_p(r)} \cdot \sin^2(\beta)}. \tag{A.4}$$

For a possible calculation of the PDR, the last step would not have been used, since it introduced a non-linearity into the calibration procedure and the failure from ignoring it was small ($sin^2(5°) = 0.0076$). Uncertainties from this method were considered much smaller than the uncertainties from the calibration method that was used for 2010. Sources of uncertainties could be the fitting method, putting too much weight on the minima of the Malus' curve and a possible rotation of the laser linear depolarisation over the first hour of measurements each day. However, preliminary results of an investigation of the two issues showed that they led to only small failures [Gausa (2011)].

A.6 Electronic noise

There are a number of instruments on site at ALOMAR. Thus, interferences cannot be avoided a priori. In some of the datasets, electronic noise was found. Three types of noise were identified: two in the time-resolved plots and one in the time-averaged plots. Figure A.3 shows an example of the first two types of noise and Figure A.4 shows an example of the third type. Most of the sources of noise were identified and the problems were resolved throughout 2010. Datasets that contained strong noise, were sorted out manually. Datasets that contained only noise in the analogue channels from high altitudes (>15 km) could be fixed through the glueing of analogue and photon counting channels.

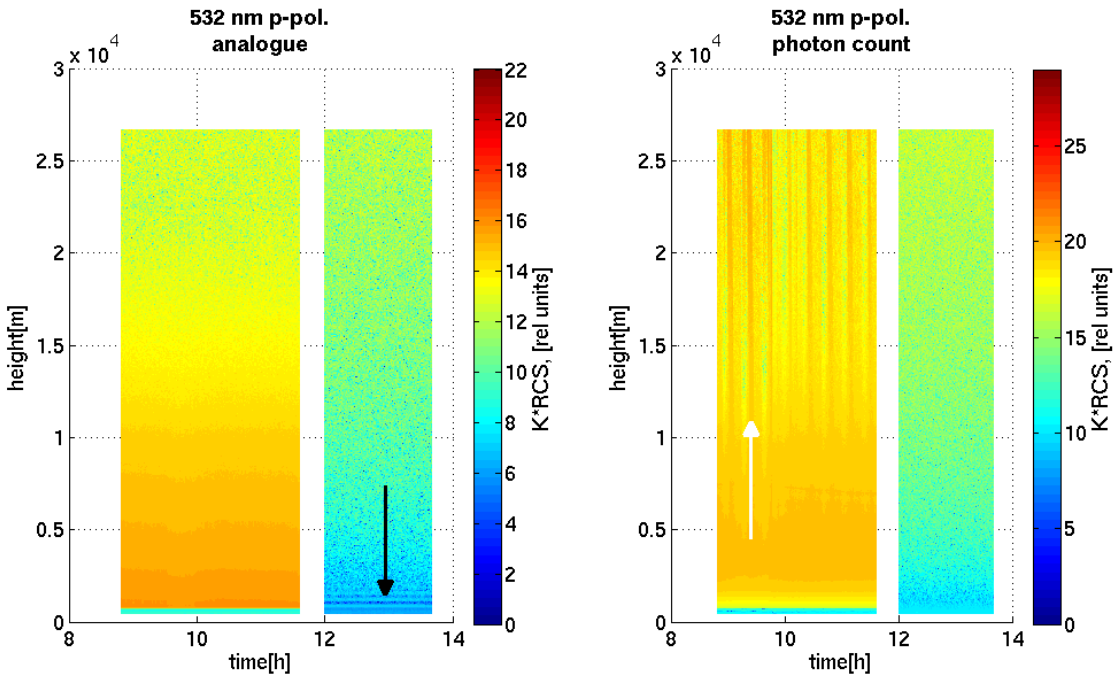

Figure A.3: 532 nm p analogue and 532 nm p photon counting channels for April 6, 2010. The analogue channel shows horizontal stripes corresponding to high temporal frequency intensity variations (black arrow). The photon counting channel shows vertical stripes corresponding to low temporal frequency intensity variations (white arrow).

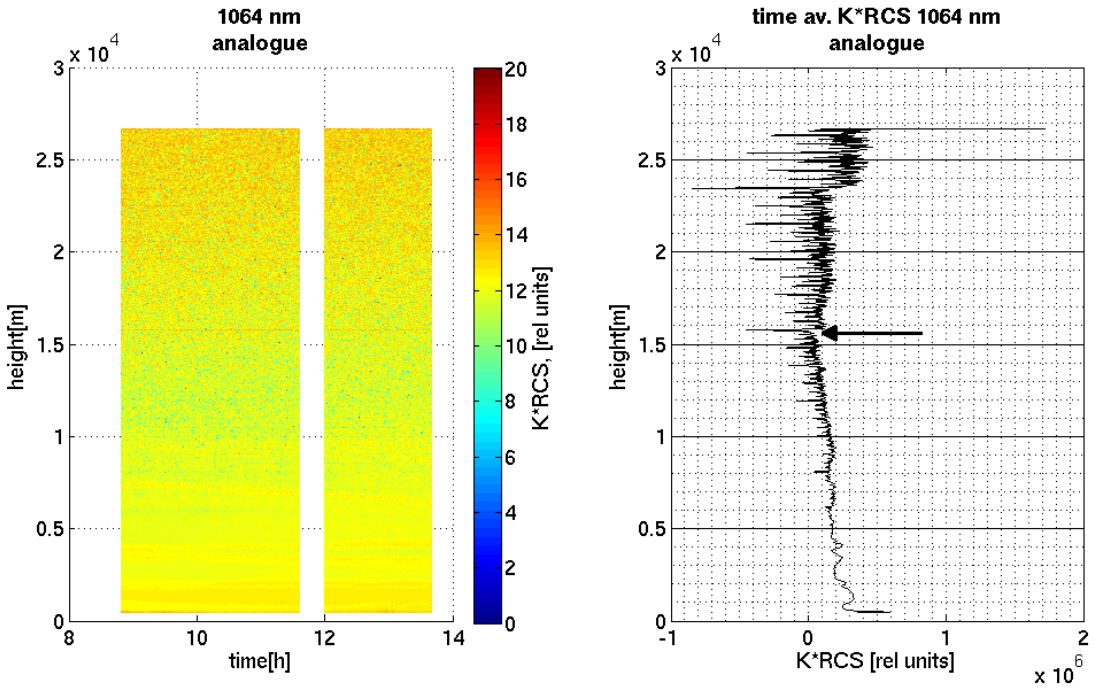

Figure A.4: 1064 nm channel for April 6, 2010. Systematic noise in the time-averaged plots appears as steps in the signal. In the time-resolved plot, no periodic noise is visible.

Appendix B

WRF-Chem

B.1 Description of RADM2/MADE/SORGAM(aq)

The aerosol and chemistry scheme RADM2/MADE/SORGAM(aq) consists of three different parts:

- The gaseous chemistry scheme is based on the **R**egional **A**cid **D**eposition **M**odel (RADM) 2. Inorganic chemistry is represented by 14 stable, 4 reactive and 3 abundant stable species (O_2, N_2 and H_2O). Atmospheric chemistry is represented by 26 stable species and 16 peroxy radicals. For 22 diagnosed and 38 predicted species, a quasi steady-state approximation method is used for the chemical production and loss tendency terms. Initial and boundary conditions are based on NASA aircraft measurements of clean oceanic midlatitude air and consist of laterally invariant vertical profiles [Grell et al. (2005)].
- The aerosol module is based on the **M**odal **A**erosol **D**ynamics Model for **E**urope (MADE) [Ackermann et al. (1998)]. Primary aerosols are defined in 40 variables, including 21 variables for dry aerosols and 19 variables for cloud related aerosols. For each species, concentrations in $\frac{\mu g}{kg(\text{dry air})}$ are given separately for the Aitken and accumulation mode. Coarse mode particle concentrations are only separated into anthropogenic, marine and soil-derived aerosols. Additionally, the total number of particles for each mode is given for dry and cloud water related aerosols.
- Organic aerosol chemistry is based on the **S**econdary **ORG**anic **A**erosol **M**odel (SORGAM) [Schell et al. (2001)]. Secondary aerosols are treated for 32 variables, of which dry and cloud water related particles include 16 variables, each.

B.2 Model control

WRF-Chem was run on UiO's parallel computing cluster TITAN. For efficiency, bash-scripts were written for model control. For creating the domain and reading

the input data, a single bash-script was run to control the three parts of WPS. A second bash-script was subsequently run to control the real.exe part of WRF-Chem. It vertically interpolates the meteorological input data sets and produces one file for the initial and the boundary conditions. When grid-nudging was used to force WRF-Chem towards the meteorological input data, the files for that were also produced by real.exe. A third bash-script was run to control the main part of WRF-Chem. All scripts were set up in a way, so that the model control and the model output were done in separate directories. This avoided to work in the directory, where WRF-Chem was stored. All necessary data were stored on the computing nodes disc space, so that changes in the model could be done, while simulations were running.

Appendix C

Bugs and added routines in WRF-Chem

A number of changes were made in WRF-Chem. The FINN tool was modified so that wildfire emissions could be constrained in time and space. In WRF-Chem, the dry and wet-deposition rates were not part of the output. A routine was added to WRF-Chem, to calculate the incremented deposition rates. Additionally, three bugs were found.

C.1 FINN

When using fire emissions in WRF-Chem, it was necessary to specify emission files for all input time-steps. However, for parts of the analyses, the emissions needed to be constrained in time. A possibility to reduce the spatial extend of fire emissions was added as well but not used for the final runs.
The FINN source code file fire_emis.f90 was modified so that temporal and spatial constraints could be set in the control namelist. Therefore, new variables were defined

```
72  !++TW
73     real                  :: minlat, maxlat, minlon, maxlon
74     integer               :: temp_1, temp_2, temp_3
75     double precision      :: temp_min, temp_max, temp
76     character(len=10)     :: min_date
77     character(len=10)     :: max_date
78  !--TW
```

and added to the namelist,

```
96  namelist /control/ domains, fire_directory, wrf_directory, fire_filename, &
97                     srf_type_filename, wrf2fire_map, start_date, end_date, &
98                     avrg_fire_size, max_fire_size, diag_level, resol,      &
99                     output_timing, glb2fire_map, minlat, maxlat, minlon,   &
100                    maxlon, min_date, max_date
```

```
!++TW
!added minlat, maxlat, minlon, maxlon, min_date, max_date above incl line break
!--TW
```

the date and time was transformed into a real number

```
!++TW
        read(wrk_date(1:4), '(I4)') temp_1
        read(wrk_date(6:7), '(I2)') temp_2
        read(wrk_date(9:10), '(I4)') temp_3
        temp = 10000*temp_1+100*temp_2+temp_3
!--TW
```

and an if-loop was included which set the emissions to zero, if the emissions took place outside the temporal and spatial constraint.

```
!++TW
          if( lat(m) < minlat .or. lat(m) > maxlat .or. lon(m) < minlon .or. lon(m) > maxlon ) then
            fire_emissions(:,m) = 0
            fire_size(m) = 0
          endif

          if( temp < temp_min .or. temp > temp_max ) then
            fire_emissions(:,m) = 0
            fire_size(m) = 0
          endif

!--TW
```

C.2 Added routines to WRF-Chem

A routine for the calculation of dry- and wet-deposition rates was added to WRF-Chem. The method was based on Hodnebrog et al. (2011). The steps were the same for both dry- and wet-deposition and wet-scavenging. A description of the method is given only for the BC dry-deposition. The total mass of BC and cloud water related BC in every grid-box was calculated before and after calling the routine dry_deposition_driver for the calculation of vertical mixing and dry-deposition. The output variables were incremented by the differences between the total mass after and before the routine. The dry-deposition rate between two arbitrary time-steps was calculated by subtracting the masses from each other for every grid-box. Since only the dry-deposition at the ground was to be calculated, the vertical mixing introduced a failure in the dry-deposition. This effect was corrected for by a vertical integration. The changes in the code are presented below.
The new variables were defined,

```
!++ TW

      REAL(KIND=8),DIMENSION(grid%sm31:grid%em31,grid%sm32:grid%em32,grid%sm33:grid%em33) :: temp_ecj_1, temp_ecj_2
```

```
145       REAL(KIND=8),DIMENSION(grid%sm31:grid%em31,grid%sm32:grid%em32,grid%sm33:↩
              grid%em33) :: temp_eci_1, temp_eci_2
146       REAL(KIND=8),DIMENSION(grid%sm31:grid%em31,grid%sm32:grid%em32,grid%sm33:↩
              grid%em33) :: temp_eccwj_1, temp_eccwj_2
147       REAL(KIND=8),DIMENSION(grid%sm31:grid%em31,grid%sm32:grid%em32,grid%sm33:↩
              grid%em33) :: temp_eccwi_1, temp_eccwi_2
148       REAL(KIND=8) ↩
                                                                                ↩
              :: increment_ecj, increment_eci
149       REAL(KIND=8) ↩
                                                                                ↩
              :: increment_eccwj, increment_eccwi
150
151   !-- TW
```

the total mass of BC was calculated in each grid-box before

```
850   !++ TW
851
852   !initialising new variables to be 0 in first time-step
853         if(grid%itimestep .EQ. 1) then
854           grid%dry_dep_eci = 0.D0
855           grid%dry_dep_ecj = 0.D0
856           grid%dry_dep_eccwi = 0.D0
857           grid%dry_dep_eccwj = 0.D0
858         end if
859
860   !calculating total mass eci and ecj per gridbox before running dry-deposition
861         increment_ecj = 0.D0
862         increment_eci = 0.D0
863         increment_eccwj = 0.D0
864         increment_eccwi = 0.D0
865         temp_ecj_1 = 0.D0
866         temp_ecj_2 = 0.D0
867         temp_eci_1 = 0.D0
868         temp_eci_2 = 0.D0
869         temp_eccwj_1 = 0.D0
870         temp_eccwj_2 = 0.D0
871         temp_eccwi_1 = 0.D0
872         temp_eccwi_2 = 0.D0
873
874         do nv=1,num_chem
875            do j=jts,jte
876               do k=kts,kte
877                  do i=its,ite
878                     if(nv .EQ. p_ecj) then
879                        temp_ecj_1(i,k,j)=chem(i,k,j,p_ecj)*rho(i,k,j)*dz8w(i,k,j)*↩
                               grid%DX*grid%DX/grid%msft(i,j)/grid%msft(i,j)
880                     else if(nv .EQ. p_eci) then
881                        temp_eci_1(i,k,j)=chem(i,k,j,p_eci)*rho(i,k,j)*dz8w(i,k,j)*↩
                               grid%DX*grid%DX/grid%msft(i,j)/grid%msft(i,j)
882                     else if(nv .EQ. p_eccwj) then
883                        temp_eccwj_1(i,k,j)=chem(i,k,j,p_eccwj)*rho(i,k,j)*dz8w(i,k,↩
                               j)*grid%DX*grid%DX/grid%msft(i,j)/grid%msft(i,j)
884                     else if(nv .EQ. p_eccwi) then
885                        temp_eccwi_1(i,k,j)=chem(i,k,j,p_eccwi)*rho(i,k,j)*dz8w(i,k,↩
                               j)*grid%DX*grid%DX/grid%msft(i,j)/grid%msft(i,j)
886                     end if
887                  enddo
888               enddo
889            enddo
890         enddo
891
892   !-- TW
```

and after running the routine dry_deposition_driver. The differences between both calculations were calculated and the variables dry_dep_ecj, dry_dep_eci, dry_dep_eccwj and dry_dep_eccwi were incremented by the differences.

```
950 !++ TW
951
952 !calculating total mass eci and ecj per gridbox after running dry-deposition
953 !and incrementing the dry-deposition for each time-step
954 !dry-deposition rates for the total domain are then given by subtracting
955 !the dry-deposition for two time-steps, summed over the entire domain
956       do nv=1,num_chem
957          do j=jts,jte
958             do k=kts,kte
959                do i=its,ite
960                   if(nv .EQ. p_ecj) then
961                      temp_ecj_2(i,k,j)=chem(i,k,j,p_ecj)*rho(i,k,j)*dz8w(i,k,j)*↩
                            grid%DX*grid%DX/grid%msft(i,j)/grid%msft(i,j)
962                      increment_ecj = temp_ecj_2(i,k,j) - temp_ecj_1(i,k,j)
963                      grid%dry_dep_ecj(i,k,j) = grid%dry_dep_ecj(i,k,j) + ↩
                            increment_ecj
964                   else if(nv .EQ. p_eci) then
965                      temp_eci_2(i,k,j)=chem(i,k,j,p_eci)*rho(i,k,j)*dz8w(i,k,j)*↩
                            grid%DX*grid%DX/grid%msft(i,j)/grid%msft(i,j)
966                      increment_eci = temp_eci_2(i,k,j) - temp_eci_1(i,k,j)
967                      grid%dry_dep_eci(i,k,j) = grid%dry_dep_eci(i,k,j) + ↩
                            increment_eci
968                   else if(nv .EQ. p_eccwj) then
969                      temp_eccwj_2(i,k,j)=chem(i,k,j,p_eccwj)*rho(i,k,j)*dz8w(i,k,↩
                            j)*grid%DX*grid%DX/grid%msft(i,j)/grid%msft(i,j)
970                      increment_eccwj = temp_eccwj_2(i,k,j) - temp_eccwj_1(i,k,j)
971                      grid%dry_dep_eccwj(i,k,j) = grid%dry_dep_eccwj(i,k,j) + ↩
                            increment_eccwj
972                   else if(nv .EQ. p_eccwi) then
973                      temp_eccwi_2(i,k,j)=chem(i,k,j,p_eccwi)*rho(i,k,j)*dz8w(i,k,↩
                            j)*grid%DX*grid%DX/grid%msft(i,j)/grid%msft(i,j)
974                      increment_eccwi = temp_eccwi_2(i,k,j) - temp_eccwi_1(i,k,j)
975                      grid%dry_dep_eccwi(i,k,j) = grid%dry_dep_eccwi(i,k,j) + ↩
                            increment_eccwi
976                   end if
977                enddo
978             enddo
979          enddo
980       enddo
981
982 !-- TW
```

The total BC mass loss due to dry-deposition is the domain averaged sum of dry_dep_ecj, dry_dep_eci, dry_dep_eccwj and dry_dep_eccwi, subtracted for two arbitrary time-steps.

C.3 Bug in the WPS routine

A bug was found in the UiO WPS setup. The standard meteorological input datasets for WRF-Chem are usually separated into atmospheric data and ground data. In the ECMWF input data, retrieved for UiO Master and PhD students, the datasets were combined. The variable table Vtable.ECMWF, that lists the contents of the input files, was therefore separated into two files Vtable.ECATM and Vtable.ECSURF. Those separated variable tables were included in the WPS routines.

After a change in the ECMWF input data, the tables were not updated and thus, the calculation of the soil moisture was neglected. A problem with the soil moisture was known for at least the last two years but the failure has not been found. A failure analysis was done and a bug-fix was produced in cooperation with Dr. Melissa Pfeffer and Bjørn-Egill Nygaard.
The updated variable table Vtable.ECSURF is given below.

```
GRIB | Level| Level| Level| metgrid  |  metgrid | metgrid
Code | Code |   1  |   2  | Name     |  Units   | Description
-----|------|------|------|----------|----------|-------------------------------------------
 165 |  1   |  0   |      | UU       | m s-1    | U
                                                  | At 10 m
 166 |  1   |  0   |      | VV       | m s-1    | V
                                                  | At 10 m
 167 |  1   |  0   |      | TT       | K        | Temperature
                                        | At 2 m
 168 |  1   |  0   |      | DEWPT    | K        |
                                                | At 2 m
     |  1   |  0   |      | RH       | %        | Relative Humidity
                                    | At 2 m
 172 |  1   |  0   |      | LANDSEA  | 0/1 Flag | Land/Sea flag
                                     |
 129 |  1   |  0   |      | SOILGEO  | m2 s-2   | blah blah blah
                                      |
     |  1   |  0   |      | SOILHGT  | m        | Terrain field of source
        analysis                     |
 134 |  1   |  0   |      | PSFC     | Pa       | Surface Pressure
                                       |
 151 |  1   |  0   |      | PMSL     | Pa       | Sea-level Pressure
                                        |
 235 |  1   |  0   |      | SKINTEMP | K        | Sea-Surface Temperature
                                          |
  31 |  1   |  0   |      | SEAICE   | 0/1 Flag | Sea-Ice-Flag
                                           |
  34 |  1   |  0   |      | SST      | K        | Sea-Surface Temperature
                                            |
 141 |  1   |  0   |      | SNOW     | kg m-2   |Water Equivalent of Accumulated
    Snow Depth|
 139 | 112  |  0   |  7   | ST000007 | K        | T of 0-7 cm ground layer
                                              |
 170 | 112  |  7   |  28  | ST007028 | K        | T of 7-28 cm ground layer
                                               |
 183 | 112  |  28  | 100  | ST028100 | K        | T of 28-100 cm ground layer
                                                |
 236 | 112  | 100  | 255  | ST100255 | K        | T of 100-255 cm ground layer
                                                 |
  39 | 112  |  0   |  7   | SM000007 | fraction | Soil moisture of 0-7 cm ground
     layer     |
  40 | 112  |  7   |  28  | SM007028 | fraction | Soil moisture of 7-28 cm ground
      layer    |
  41 | 112  |  28  | 100  | SM028100 | fraction | Soil moisture of 28-100 cm
     ground layer  |
  42 | 112  | 100  | 255  | SM100255 | fraction | Soil moisture of 100-255 cm
     ground layer |
-----|------|------|------|----------|----------|-------------------------------------------
```

C.4 Bug in the FINN tool

A mapping from the FINN species to the species within WRF-Chem is required in the input namelist of the FINN tool. A mapping that was written by Gabriele Pfister at NCAR, was provided by Øivind Hodnebrog. The aerosol species PM 2.5, PM 10, BC, OC and sulphate were simply mapped to the corresponding species within WRF-Chem. The PM species were hereby treated as additional non-specified aerosols. However, in the FINN tool, the PM 2.5 and PM 10 aerosol species include all aerosols with sizes smaller than 2.5 and 10 μm, including BC, OC and sulphate. This failure in the mapping led to an overestimation of the residual PM emissions in comparison to the other emissions, changing the plumes optical properties. The failure was found by the author and corrected in cooperation with Gabriele Pfister and Christine Wiedinmyer at NCAR.
The corrected mapping for the aerosol species is given below.

```
1 wrf2fire_map = 'pm10 -> 1.0*PM10 + -1.0*PM25;aerosol',
2                'pm25 -> 0.36*PM25;aerosol','oc -> 0.54*PM25;aerosol',
3                'bc -> 0.09*PM25;aerosol','sulf -> 0.01*PM25',
```

C.5 SORGAM aerosols

A bug was found in the subroutine sorgam_addemiss in module_aerosols_sorgam.F. The plumerise routine assigns the emissions to the correct vertical levels, according to the atmospheric stability. In the subroutine sorgam_addemiss, emissions are added to the chem-array (containing the information on all chemical species in WRF-Chem). The emissions are read from the variables ebu. Since the emissions were already treated by the plumerise routine, their vertical extend is the full number of vertical layers in WRF-Chem. Other emissions were not necessarily treated by the plumerise routine. Their number of vertical levels needs to be defined in the input namelist (kemit).
The ebu variable was assigned with kemit vertical levels. This led to a failure in the emissions treatment and to wrong concentrations of the aerosol species. The changes that were made in the code are given below.

```
8096 ! ++TW
8097 ! commented out 3 lines, added 3 modified lines
8098 !   REAL, DIMENSION( ims:ime, kms:kemit, jms:jme,num_ebu ),          &
8099 !         INTENT(IN     ) ::                                         &
8100 !         ebu
8101    REAL, DIMENSION( ims:ime, kms:kme, jms:jme,num_ebu ),           &
8102          INTENT(IN     ) ::                                          &
8103          ebu
8104 ! --TW
```

Appendix D

Illustration of the use of PDFs

The difference in PDF of the BC concentration between absorbing and non-absorbing simulations is an abstract construct that is explained in more detail here. The PDF of the BC concentration is an expression for how often concentrations occure in the computational domain. An example of the PDF of the BC concentration for the 100-fold emission scenario is given in Figure D.1, left-panel. The different curves show the model-time (day of April, 2010), for which the PDF was calculated. The peak at $10^{-13.5}\,\frac{\mu g}{m^3}$ is visible for all model-times. This is the background aerosol concentration in WRF-Chem. The number of cells containing the background aerosol concentration is decreasing with time, while aerosols are emitted.

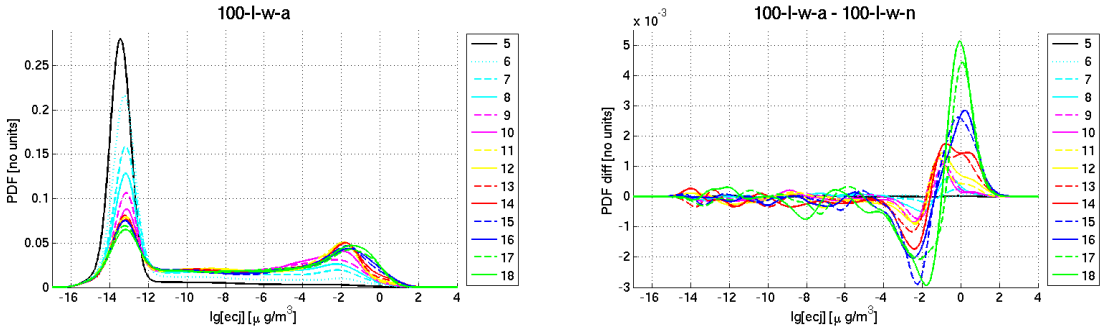

Figure D.1: Left panel: PDF of the BC concentration for the simulation 100-l-w-a. Right panel: Differences in PDF between the simulations 100-l-w-a - 100-l-w-n. The day of April, 2010 is given in the legends. The PDFs of both the absorbing and the non-absorbing simulations are normalized. Thus, differences in PDF are zero in average and show differences in the relative occurrence of the concentrations.

The second peak around $10^{-2}\,\frac{\mu g}{m^3}$ is the aerosol concentration for grid-boxes that are influenced by emissions from wildfires. The centre of the peak corresponds to the outer parts of the plumes, the concentrations lower than $10^{-3}\,\frac{\mu g}{m^3}$ correspond to highly diluted air that is probably detached from strong plumes. The concentrations larger than $10^{0}\,\frac{\mu g}{m^3}$ correspond to the plume centres. The number of cells containing plumes

is increasing with time over the first few days and stabilises later. The concentrations larger than $10^0 \frac{\mu g}{m^3}$, corresponding to the plume centres (the areas with the maximum aerosol concentrations), occur less often than the lower concentrations.
The differences in PDF between the absorbing and the non-absorbing simulations for the same emission scenario is shown in Figure D.1, right panel. The differences are close to 0 for all concentrations during the first few simulation days and increase later. The differences are maximum around $10^0 \frac{\mu g}{m^3}$ and minimum around $10^{-2.5} \frac{\mu g}{m^3}$. The maximum at the high concentrations suggests that strong plumes fill more grid-boxes in the absorbing than in the non-absorbing simulations. The minimum at the lower concentrations suggests that diluted plume parts fill less grid-boxes in the absorbing than in the non-absorbing simulation. From this, it can be concluded that the plumes in the absorbing simulation contain more regions of high aerosol concentrations then the plumes in the non-absorbing simulations. This can either mean that the plumes in the non-absorbing simulation are more dispersed or that aerosols in the strong plume parts have been lost to wet-scavenging.
Since the PDFs from both the absorbing and the non-absorbing simulations are normalised, the integral of the differences over the concentrations is always zero.